



# IRREVERSIBLE TRANSFER OF HEAT, WORK, AND MATTER ACROSS THIN BOUNDARIES

Elizabeth Duselis<sup>[a]</sup> and Jurgen Honig<sup>[a]\*</sup>

**Keywords:** Irreversible Processes, Transfer Across Boundaries, Entropy of Irreversible Transfers, Quasistatic Irreversible Processes

---

Here we extend a set of earlier articles that dealt with time-dependent irreversible processes across a thin boundary separating a system from its surroundings. The entropy change for irreversible transfers of heat, work, and matter in this compound system is examined for a one component condensed phase for which temperature, pressure, and mole numbers are the control variables. The required fundamental relations are collected and evaluated to generate an expression for the entropy change in terms of experimentally determinable variables. Contributions to the entropy change from heat exchange, work performance, and material transfer are evaluated for two distinct time-dependent paths. While contributions from each element differ for the two cases, the sum of all three elements remains identical for both time variations, as is consistent with entropy being a function of state. The net entropy change upon irreversibly cycling is also assessed.

---

Corresponding Author  
Tel: + 765 494 5279  
Fax: +765 494 0239  
E-Mail: [jmh@purdue.edu](mailto:jmh@purdue.edu)  
[a] Department of Chemistry  
Purdue University  
560 Oval Drive  
West Lafayette, IN  
47907-2084

## Introduction

The study of irreversible processes in terms of thermodynamic variables<sup>1-7</sup> generally involves identifying the relevant fluxes and forces, setting up the corresponding linear phenomenological equations, and imposing steady state conditions to identify the transport coefficient. This method has been broadened over the last 25 years via the so-called extended thermodynamics approach<sup>8-11</sup> that permit handling greater departures from equilibrium. One of the problems in this latter treatment is the definition under nonequilibrium conditions of intensive variables such as temperature, pressure, or chemical potential, and the specification of the ordinary functions of state, such as energy and entropy, well away from equilibrium.

We base the present paper on earlier work<sup>12-19</sup> in which we attempt to treat the contribution of heat exchange, work performance, and material transfers to entropy changes in irreversible processes relative to those executed reversibly. In setting up the requisite theory we note that in the extended thermodynamics method so far investigated<sup>20-24</sup> the temperature  $\theta$  appropriate for characterizing irreversible processes differed from the equilibrium temperature  $T$  by no more than 10%, and that the difference was frequently considerably smaller.

Accordingly, in the present approach we introduce the use of intensive variables appropriate to equilibrium configurations, while investigating significant departures

from equilibrium. Here that method is applied to a one-component system in the condensed state.

The system under study consists of a system at temperature  $T$ , pressure  $P$ , and chemical potential  $\mu$  which is connected via a thin, porous, moveable boundary layer to an enormous reservoir – also called surroundings – whose intensive variables are specified by  $T_0$ ,  $P_0$ , and  $\mu_0$ . The setup is shown in Fig. 1 with a superimposed temperature profile, which is uniform over virtually the entire extension of both the system and the reservoir, and which changes abruptly over the length of the junction. A similar profile obtains for pressure and chemical potential. For this situation to be applicable, our study is restricted to *quasistatic irreversible processes* (QSIPs): these are assumed to occur at a rate that permits the use of intensive variables which change *uniformly* with time  $t$ . In accord with standard convention, all processes within the reservoir are assumed to take place reversibly, while  $T_0$ ,  $P_0$ , and  $\mu_0$  remain constant. To approach such conditions experimentally, the reservoir must be huge in extension, and one must deal with systems that are very thin in extension and/or for which the relaxation time for establishing equilibrium is exceedingly short; alternatively, one must surround small, separated regions of the entire system by their own reservoirs acting in concert.

## Fundamentals

In the current study the control variables are temperature  $T$ , pressure  $P$ , and mole number  $n$ . Consider now an infinitesimal step in a process involving these variables. Let  $d\theta$  represent the path-dependent differential change in entropy  $S$  when this step is carried out irreversibly (designated as  $d_b S_0$ ) as compared to reversibly (designate as  $d_a S_0$ ). Then

$$d\theta = d_b S_0 - d_a S_0. \quad (1)$$

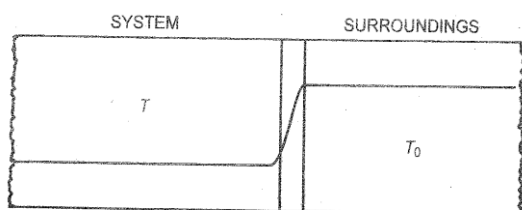


Fig. 1. Temperature Profile Across a Thin Junction Separating a System from its Surroundings in the QSIP Mode of Operation

For the reversible operation we may set  $d_a S_0 = -dS(T, P, n)$ , so that Eq. (1) reads

$$dS(T, P, n) + dS_0(T_0, P_0, n_0) = d\theta \quad (2)$$

We now set up the differential equations for the energy of the system and surroundings, as applicable to reversible processes:

$$dE(S, V, n) = TdS - PdV + \mu dn \quad (3a)$$

$$T_0 d\theta = (T - T_0) \left[ \frac{C_P}{T} dT - \alpha V dP + \tilde{S} dn \right] - (P_0 - P) [\alpha V dT - \beta P dP + \tilde{V} dn] + (\mu_0 - \mu) dn \quad (5)$$

where quantities with the tilde represent the partial molal entropy and volume. Eq. (5) is the fundamental relation derived earlier by a different approach<sup>16</sup>.

We now introduce the requisite equation of state for condensed matter, in which higher order terms are omitted:

$$\tilde{V} = \tilde{V}(T, P) = \tilde{V}_a \left[ 1 + \alpha(T - T_i) - \beta(P - P_i) \right] \quad (6)$$

where  $\tilde{V}_a \equiv \tilde{V}(T_i, P_i)$ . Here  $\tilde{V}_a$  is the molar volume at some specified initial pressure  $P_i$  and temperature  $T_i$  common to the system and the reservoir. However, to simplify the subsequent operations we adopt the truncated form

$$\tilde{V}(T_i, P_i) = \tilde{V}_a (1 + \alpha T - \beta P), \quad (7)$$

which is permissible since we will show that only the first order terms in  $\alpha \tilde{V}_a$  and  $\beta \tilde{V}_a$  are encountered in the final results. When Eq. (7) is used in Eq. (5) we may specify  $d\theta$  as a sum of three terms:

$$d\theta = d\theta_T + d\theta_P + d\theta_n, \quad (8)$$

where

$$d\theta_T = \left[ \left( 1 - \frac{T}{T_0} \right) \frac{n \tilde{C}_P}{T} - \frac{P_0}{T_0} \left( 1 - \frac{P}{P_0} \right) \alpha n \tilde{V}_a \right] dT \quad (9)$$

$$d\theta_P = \left[ \frac{P_0}{T_0} \left( 1 - \frac{P}{P_0} \right) \beta n \tilde{V}_a - \left( 1 - \frac{T}{T_0} \right) \alpha n \tilde{V}_a \right] dP \quad (10)$$

$$d\theta_n = \frac{1}{T_0} \left[ \tilde{T}_0 (\tilde{S} - \tilde{S}_0) + (\tilde{H}_0 - \tilde{H}) - (P_0 - P) \tilde{V} \right] dn \quad (11)$$

$$dE_0(S_0, V_0, n_0) = T_0 dS_0 - P_0 dV_0 + \mu_0 dn_0 \quad (3b)$$

However, since  $E$  and  $E_0$  are functions of state, we may reconstitute the above so as to apply to irreversible processes, by substituting for  $dS_0$  from Eq. (2).

We next invoke energy conservation for the compound system by setting  $dE + dE_0 = 0$ , impose volume conservation by setting  $dV + dV_0 = 0$ , and conservation of material by setting  $dn + dn_0 = 0$ . Then for a sequence of elementary steps we write

$$dS = (\partial S / \partial T) dT + (\partial S / \partial P) dP + (\partial S / \partial n) dn \quad (4a)$$

$$dV = (\partial V / \partial T) dT + (\partial V / \partial P) dP + (\partial V / \partial n) dn, \quad (4b)$$

and introduce the standard Maxwell relation, the heat capacity under constant pressure,  $C_P$ , the isobaric coefficient of expansion  $\alpha$ , and isothermal coefficient of compression  $\beta$  of the material to obtain by addition of the two energy differentials in Eq. (2) the result

The last equation requires elaboration. We need to determine the molar entropy and enthalpy for the system on the assumption that they are independent of mole number  $n$ . Integration of Eq. (4a) from the initial temperature and pressure to any intermediate temperature and pressure yields:

$$\tilde{S}(T, P) = \tilde{S}(T_i, P_i) + \int_{T_i, P_i}^{T, P} \frac{\tilde{C}_P}{T} dT - \int_{T_i, P_i}^{T, P} \alpha \tilde{V}_a dP \quad (12a)$$

$$\tilde{S}(T, P) = \tilde{S}(T_i, P_i) + \tilde{C}_P \ln \frac{T}{T_i} - \alpha \tilde{V}_a (P - P_i) \quad (12b)$$

The same relations obtain for the molar entropy of the reservoir, by replacing  $T$  and  $P$  with  $T_0$  and  $P_0$  respectively.

The molar enthalpy is found by utilizing Eq. (7) and the caloric equation of state:

$$\left( \frac{\partial \tilde{H}}{\partial P} \right)_T = \tilde{V} - T \left( \frac{\partial \tilde{V}}{\partial T} \right)_P = \tilde{V}_a (1 - \beta P) \quad (13)$$

which yields the integrated form:

$$\tilde{H}(T, P) = \tilde{H}(T_i, P_i) + \tilde{V}_a P - \frac{1}{2} \beta \tilde{V}_a P^2 + F(T) \quad (14)$$

where  $F(T)$  is an arbitrary function of temperature, which is found by setting  $\tilde{H}(0, T) = 3RT$  for a monatomic solid with no internal degrees of freedom, which is maintained at intermediate temperatures. When this approximation is inserted back into (14), we obtain:

$$\tilde{H}(T, P) = \tilde{H}(T_i, P_i) + \tilde{V}_a P - \frac{1}{2} \beta \tilde{V}_a P^2 + 3RT \quad (15)$$

The same relation can be used for  $\tilde{H}_0$  by replacing  $P$  and  $T$  with  $P_0$  and  $T_0$ , respectively. Clearly, for later use, the above approximation restricts us to a rather narrow temperature range. When we insert  $S(T, P)$ ,  $S_0(T_0, P_0)$ ,  $\tilde{H}(T, P)$ , and  $\tilde{H}_0(T_0, P_0)$  into (11), we obtain:

$$d\theta_n = \left[ 3R \left( 1 + \ln \frac{T}{T_0} - \frac{T}{T_0} \right) + \alpha \tilde{V}_a (P_0 - P) \left( 1 - \frac{T}{T_0} \right) - \frac{\beta \tilde{V}_a}{2T_0} (P_0 - P)^2 \right] dn \quad (16)$$

Eqs. (9), (10), and (16) form the basis of all subsequent operations.

### Special cases

To obtain the entropy associated with the above approach we must integrate Eq. (8). For this purpose, we specify two distinct irreversible processes that involve: heat exchange

while the temperature of the system evolves, execution of work during changes in pressure exerted on the system, and the transfer of matter across the boundary. To that end we introduce the time  $t$  as a parameter and set  $T = T(t)$ ,  $P = P(t)$ , and  $n = n(t)$ , while keeping the corresponding intensive variables of the reservoir fixed. We then integrate Eqs. (9), (10), and (16) for a time interval  $0 \leq t \leq \tau$  within which the system goes from initial temperature  $T_i$ , pressure  $P_i$ , and mole number  $n_i$  to final values  $T_f$ ,  $P_f$ , and  $n_f$ . For definiteness we assume that  $T < T_0$ ,  $P < P_0$ , and  $n < n_0$ , and we also set  $dT = (dT/dt)dt$ ,  $dP = (dP/dt)dt$ , and  $dn = (dn/dt)dt$ . The resulting integrations are straightforward but tedious.

### Case 1

Let  $T(t) = T_i e^{k_T t}$ ,  $P(t) = P_i e^{k_P t}$ , and  $n(t) = n_i e^{k_n t}$ ,

$T_f = T_i e^{k_T \tau}$ ,  $P_f = P_i e^{k_P \tau}$ ,  $n_f = n_i e^{k_n \tau}$ , where  $k_T$ ,  $k_P$ , and  $k_n$  are constants such that  $(k_P/k_n) = \ln(P_f/P_i)/\ln(n_f/n_i)$ , and  $(k_P/k_T) = \ln(P_f/P_i)/\ln(T_f/T_i)$ , and  $(k_T/k_n) = \ln(T_f/T_i)/\ln(n_f/n_i)$ . Integration of (9), (10), and (16) yields, respectively:

$$\theta_T = 3R \left[ \frac{k_T}{k_n} (n_f - n_i) - \frac{1}{T_0} \left( \frac{1}{1 + k_n/k_T} \right) (n_f T_f - n_i T_i) \right] - \alpha \tilde{V}_a \left[ \frac{P_0}{T_0} \left( \frac{1}{1 + k_n/k_T} \right) (n_f T_f - n_i T_i) - \frac{1}{T_0} \left( \frac{1}{1 + (k_n + k_P)/k_T} \right) (n_f T_f P_f - n_i T_i P_i) \right] \quad (17)$$

$$\theta_P = \beta \tilde{V}_a \left[ \frac{P_0}{T_0} \left( \frac{1}{1 + k_n/k_P} \right) (n_f P_f - n_i P_i) - \frac{1}{T_0} \left( \frac{1}{2 + k_n/k_P} \right) (n_f P_f^2 - n_i P_i^2) \right] + \alpha \tilde{V}_a \left[ \frac{1}{T_0} \left( \frac{1}{1 + (k_n + k_T)/k_P} \right) (n_f T_f P_f - n_i T_i P_i) - \left( \frac{1}{1 + k_n/k_P} \right) (n_f P_f - n_i P_i) \right] \quad (18)$$

### Case 2

Case 2 differs from case 1 by the pressure and mole number dependence on time. Let  $T(t) = T_i e^{k_T t}$ , as before,

$P(t) = P_i(1 + k_P t)$ , and  $n(t) = n_i(1 + k_n t)$ , so that  $(k_T/k_n) = \ln(T_f/T_i)/(n_f/n_i - 1)$ ,  $(k_T/k_P) = \ln(T_f/T_i)/(P_f/P_i - 1)$ ,  $(k_T/k_n) = (P_f/P_i - 1)/(n_f/n_i - 1)$ . Eqs. (20), (21), and (22) are found in the same manner as for case 1:

$$\begin{aligned} \theta_n = & 3R \left[ (n_f - n_i) \left( \ln \frac{T_i}{T_0} + 1 \right) + \frac{k_T}{k_n} \left( n_f \ln \frac{n_f}{n_i} - (n_f - n_i) \right) - \frac{1}{T_0} \left( \frac{1}{1 + k_T/k_n} \right) (n_f T_f - n_i T_i) \right] \\ & + \beta \tilde{V}_a \left[ \frac{P_0}{T_0} \left( \frac{1}{1 + k_P/k_n} \right) (n_f P_f - n_i P_i) - \frac{2}{T_0} \left( \frac{1}{2k_P/k_n + 1} \right) (n_f P_f^2 - n_i P_i^2) - \frac{P_0^2}{2T_0} (n_f - n_i) \right] \\ & - \alpha \tilde{V}_a \left[ \left( \frac{1}{1 + k_P/k_n} \right) (n_f P_f - n_i P_i) + \frac{P_0}{T_0} \left( \frac{1}{1 + k_T/k_n} \right) (n_f T_f - n_i T_i) - \frac{1}{T_0} \left( \frac{1}{1 + (k_n + k_P)/k_T} \right) (n_f T_f P_f - n_i T_i P_i) + P_0 (n_f - n_i) \right] \end{aligned} \quad (19)$$

$$\begin{aligned} \theta_T = & \frac{3R}{2} \left\{ \ln \frac{T_f}{T_i} (n_f + n_i) - \frac{2}{T_0} n_i \left[ (T_f - T_i) + \frac{k_n}{k_T} \left( T_f \ln \frac{T_f}{T_i} - (T_f - T_i) \right) \right] \right\} \\ & - \alpha \tilde{V}_a \left\{ \frac{P_0}{T_0} n_i \left[ (T_f - T_i) + \frac{k_n}{k_T} \left( T_f \ln \frac{T_f}{T_i} - (T_f - T_i) \right) \right] \right. \\ & \left. - \frac{1}{T_0} n_i P_i \left[ \left( T_f \ln \frac{T_f}{T_i} - (T_f - T_i) \right) \left( \frac{k_P + k_n}{k_T} \right) + (T_f - T_i) + \frac{2k_P k_n}{k_T^2} \left( \frac{1}{2} T_f \ln^2 \frac{T_f}{T_i} - T_f \ln \frac{T_f}{T_i} - (T_f - T_i) \right) \right] \right\} \end{aligned} \quad (20)$$

$$\begin{aligned} \theta_P = & -\beta \tilde{V}_a \frac{(P_f - P_i)}{T_0} \left\{ -\frac{P_0}{2} (n_f - n_i) + \frac{1}{3} \left[ n_i P_i + n_f P_f + \frac{1}{2} (n_i P_f + n_f P_i) \right] \right\} \\ & + \alpha \tilde{V}_a \left\{ \frac{1}{2} (P_f - P_i) (n_f - n_i) + \frac{1}{T_0} n_i P_i \frac{k_P}{k_T} \left[ (T_f - T_i) + \frac{k_n}{k_T} \left( T_f \ln \frac{T_f}{T_i} - (T_f - T_i) \right) \right] \right\} \end{aligned} \quad (21)$$

$$\begin{aligned} \theta_n = & 3R \left\{ (n_f - n_i) \left[ 1 + \ln \frac{T_i}{T_0} + \frac{1}{2} \ln \frac{T_f}{T_i} \right] - \frac{1}{T_0} \frac{k_n}{k_T} n_i (T_f - T_i) \right\} + \beta \tilde{V}_a \left\{ \frac{(n_f - n_i)}{2T_0} \left[ P_0 (P_f + P_i - P_0) - \frac{1}{3} (P_f^2 + P_f P_i + P_i^2) \right] \right\} \\ & - \alpha \tilde{V}_a \left\{ \frac{P_0}{T_0} \frac{k_n}{k_T} n_i (T_f - T_i) - \frac{1}{2} (P_f + P_i) (n_f - n_i) + \frac{1}{T_0} \frac{k_n}{k_T} n_i P_i \left[ (T_f - T_i) + \frac{k_P}{k_T} \left( T_f \ln \frac{T_f}{T_i} - (T_f - T_i) \right) \right] + P_0 (n_f - n_i) \right\} \end{aligned} \quad (22)$$

Despite the considerable differences encountered in the two cases, the total entropy change associated with (8),

upon eliminating  $k_n/k_P$ ,  $k_n/k_T$ , and  $k_P/k_T$  ratios, leads to exactly the same grand total result:

$$\begin{aligned} \theta = & 3R \left[ n_f \ln \frac{T_f}{T_0} - n_i \ln \frac{T_0}{T_i} + (n_f - n_i) + \frac{1}{T_0} (n_f T_f - n_i T_i) \right] \\ & - \beta \tilde{V}_a \left[ \frac{1}{2T_0} (n_f P_f^2 - n_i P_i^2) + \frac{P_0^2}{2T_0} (n_f - n_i) - \frac{P_0}{T_0} (n_f P_f - n_i P_i) \right] \\ & - \alpha \tilde{V}_a \left[ \frac{P_0}{T_0} (n_f T_f - n_i T_i) + (n_f P_f - n_i P_i) - \frac{1}{T_0} (n_f T_f P_f - n_i T_i P_i) - P_0 (n_f - n_i) \right] \end{aligned} \quad (23)$$

The pathway in which the system went from initial to final configuration across the boundary was not specified in the approximation. Thus, when we initially defined the two cases, we set up ratios for  $T_f/T_i$ ,  $P_f/P_i$ , and  $n_f/n_i$ , which required  $k_T$ ,  $k_P$ ,  $k_n$ , and  $\tau$  to change to fit the specified ratios. What (17), (18), and (19) and (20), (21), and (22) do is to show the differences in the contributions to the overall entropy from the heat evolution, execution of work due to pressure changes, and matter transfers across the boundary.

However, the individual contributions in the two cases sum to the same final result; this is consistent with entropy being a function of state.

## The Cyclic Process

So far we have considered variations of temperature, pressure, and chemical potential only in one direction.

Also of interest is a cyclic process in which the intensive variables of the system are changed in the order  $T_i \rightarrow T_f \rightarrow T_i$ ,  $P_i \rightarrow P_f \rightarrow P_i$ , and  $n_i \rightarrow n_f \rightarrow n_i$ .

## Discussion

$$\begin{aligned} \theta = 3R & \left[ n_f \left( \ln \frac{T_f}{T_0} + \ln \frac{T_f}{T_1} \right) + n_i \left( \ln \frac{T_i}{T_0} + \ln \frac{T_i}{T_1} \right) - (n_i T_i - n_f T_f) \left( \frac{1}{T_0} - \frac{1}{T_1} \right) \right] \\ & + \frac{\beta \tilde{V}_a}{2} \left[ (n_f P_f^2 - n_i P_i^2) \left( \frac{1}{T_0} - \frac{1}{T_1} \right) + 2(n_f P_f - n_i P_i) \left( \frac{P_0}{T_0} - \frac{P_1}{T_1} \right) + (n_f - n_i) \left( \frac{P_1^2}{T_1} - \frac{P_0^2}{T_0} \right) \right] \\ & + \alpha \tilde{V}_a \left[ (n_i T_i - n_f T_f) \left( \frac{P_0}{T_0} - \frac{P_1}{T_1} \right) + (n_f T_f P_f - n_i T_i P_i) \left( \frac{1}{T_0} - \frac{1}{T_1} \right) + (n_f - n_i) (P_0 - P_1) \right] \end{aligned} \quad (24)$$

Close examination of Eq. (23) shows the following: In accord with past experience<sup>14,19</sup> this end result is independent of the time protocol that had been selected. Mathematically this is related to the fact that the right hand side of Eq. (1) involves a difference in two functions of state. The present analysis shows, however, how the individual contributions  $\theta_T$ ,  $\theta_P$ , and  $\theta_n$  depend on the selected time dependence of the control variables.

One should note that the quantity  $\tilde{V}_a$  does not appear in the above relation; only the first order terms  $\alpha \tilde{V}_a$  and  $\beta \tilde{V}_a$  are encountered in Eqs. (23) and (24). Going back to Eq. (10), this implies that changes of pressure exert only a secondary effect on the properties of the system. Effectively, in zero order, the material is incompressible. It is for this reason that Eq. (7) rather than (6) could be used in the derivations.

The leading term in Eq. (23) is of the form

$$\theta = 3R \left\{ n_f \left[ \ln \frac{T_f}{T_0} - \frac{T_f}{T_0} \right] - n_i \left[ \ln \frac{T_i}{T_0} - \frac{T_i}{T_0} \right] + (n_f - n_i) \right\}$$

*Eur. Chem. Bull.* **2012**, 1(6), 175-180

DOI: 10.17628/ecb.2012.1.175-180

To accomplish this, we attach the system to another reservoir at temperature  $T_1$ , pressure  $P_1$ , and mole number  $n_1$ , in which  $T_1 < T_i$ ,  $P_1 < P_i$ , and  $n_1 < n_i$ .

While the system interacts with reservoir 0, reservoir 1 remains sealed off, and vice versa. The interaction with the reservoir for the return process is handled by reversing the indices  $i$  and  $f$  and replacing subscript 0 by subscript 1 in (23). When this newly generated expression is added to (23), one obtains for the cyclic process:

(25)

When there is no transfer of material,  $n_f = n_i \equiv n$ , the above reduces to

$$\theta = 3Rn \left( \ln \frac{T_f}{T_i} - \frac{T_f}{T_0} + \frac{T_i}{T_0} \right). \quad (26)$$

Numerical calculations reveal that for ratios  $T_f/T_i \leq 2$  (with  $T_i < T_f$ ) the above quantity is positive. If additionally there is no temperature difference between the reservoir and the system,  $\theta = 0$ .

This is reasonable, given the fact that when  $T$  and  $P$  are uniform throughout the compound system, the transfer of essentially incompressible material incurs no changes in entropy (in the approximation of Eq. (7)). In the range  $T_f/T_i > 2$  the calculations involving (25) and (26) become increasingly unreliable, which indicates that the

approximation  $\tilde{C}_p = 3R$ , adopted earlier, has failed, as was is to be expected. One may extend the present approach by adopting the Debye theory for the heat capacity of monatomic solids to replace the current approximation.

It is instructive to note how Eqs. (23) and (24) differ. The cyclic process refers only to what goes on in the system. In actuality, heat, work, and material are transferred from the reservoir at temperature  $T_0$  to the one at temperature  $T_1$ . This is reflected in the difference between the leading terms in the two equations.

The first order terms may all be grouped into contributions  $\alpha\tilde{V}_a$  and  $\beta\tilde{V}_a$  associated with the thermal expansion and compressibility of the condensed phase respectively. These terms are small relative to the leading expressions that involve the gas constant  $R$ .

If desired, one may determine  $d_b S_0 = -dS + d\theta$ , using Eqs. (4), (9), (10), and (16) to determine the entropy change of the reservoir in response to the irreversible processes occurring in the system.

## Conclusions

In conclusion, we have considered the transfer of heat, work, and mass across a thin junction separating a system from the reservoir under conditions where the intensive variables in the two portions of the combined unit are different. The principal restriction of the study of the irreversible processes is the adoption of QSIPs, so that the intensive variables still retain their meaning even under nonequilibrium conditions. The resulting changes in state were studied by using time  $t$  as a parameter to characterize the processes. As anticipated, in the two cases studied, the entropy change is independent of the time protocol involved; the same should hold true for any other chosen time protocol. However, the individual contribution to the total entropy, i.e., the contributions due to heat flow, work exchange, and mass transfer do depend on the chosen path.

## References

- <sup>1</sup>Bejan, A., *Advanced Engineering Thermodynamics*, 2nd edition, p.135, Wiley, New York, **1997**.
- <sup>2</sup>de Groot, S. R., Mazur, P., *Non-Equilibrium Thermodynamics*. North Holland, Amsterdam, **1962**.
- <sup>3</sup>Gyarmati, I., *Non-equilibrium Thermodynamics*, Field Theory, and Variational Principles, Springer Verlag, New York, **1970**.
- <sup>4</sup>Haase, R., *Thermodynamics of Irreversible Processes*, Dover, New York, **1990**.

- <sup>5</sup>Kondepudi, D., Prigogine, I., *Modern Thermodynamics, from Heat Engines to Dissipative Structures*, Chaps. 15-17, Wiley, Chichester, **1998**.
- <sup>6</sup>Meixner, J., *Thermodynamik der Irreversiblen Prozesse*, Meixner, Aachen, Germany, **1954**.
- <sup>7</sup>Prigogine, I., *Introduction to Thermodynamics of Irreversible Processes*, Wiley, New York, **1967**.
- <sup>8</sup>Jou, D., Casas-Vázquez, J., Lebon, G., *Extended Irreversible Thermodynamics*, 4<sup>th</sup> edition, Chap. 3, Springer Verlag, Berlin, **2010**.
- <sup>9</sup>Jou, D., Casas-Vázquez, J., Lebon, G. Extended thermodynamics revisited (1988-1998), *Rep. Progr. Phys.* **1999**, 62, 1052.
- <sup>10</sup>Lebon, G., Jou, D., Casas-Vázquez, J., in *Entropy and Entropy Generation*, Shiner J. S., Ed., 37-45, Kluwer Academic, Dordrecht **1996**.
- <sup>11</sup>Mueller, I., Ruggeri, T., *Extended Thermodynamics*, Springer Verlag, New York, **1993**.
- <sup>12</sup>Ben Amotz, D., Honig, J. M., *J. Phys. Chem. B*, **2006**, 110, 19966.
- <sup>13</sup>Ben Amotz, D., Honig J. M., *Phys. Rev. Lett.*, **2006**, 96, 020602/1-4.
- <sup>14</sup>Hoehn, R., Honig J. M. *Acta Phys. Polon. A*, **2011**, 119, 323.
- <sup>15</sup>Honig, J. M. *Thermodynamics, Principles Characterizing Chemical and Physical Processes*, 3rd edition, Chapter 6, Academic Press, Amsterdam, **2008**.
- <sup>16</sup>Honig, J. M., *Appl. Phys. Res.*, **2011**, 3, 3.
- <sup>17</sup>Honig, J. M., Ben Amotz, D., *J. Chem. Educ.*, **2005**, 83, 132.
- <sup>18</sup>Honig, J. M., Ben Amotz, D., *Chem. Educator*, **2008**, 13, 220.
- <sup>19</sup>Honig, J. M., Hoehn, R., *Open J. Chem. Eng.*, **2011**, 5, 1.
- <sup>20</sup>Evans, D. J., *J. Stat. Phys.* **1989**, 57, 745.
- <sup>21</sup>Fort, J., *Physica A*, 1997, 243, 275.
- <sup>22</sup>Jou, D., Casas-Vázquez, J., *Phys. Rev. A*, **1992**, 45, 8371.
- <sup>23</sup>Kaufmann, M., Muschik, W., Schirrmester, D., in *Entropy and Entropy Generation*, Shiner, J., S., Ed., Chap 1, Kluwer Academic, Dordrecht, **1996**.
- <sup>24</sup>Jou, D., Cimmelli, V. A., Sellitto, A., *J. Non-equil. Thermodyn.*, **2011**, 36, 373.

Received: 11.09.2012.

Accepted: 25.09.2012.



# REVIEW ON UTILIZATION OF OIL SHALE AND SHALE OIL PRODUCTION AT FUSHUN DEPOSIT

Zhang Xiaoli [a]\*

**Keywords:** Fushun; shale oil; oil shale; review; utilization

The utilization of Fushun oil shale as raw material has been reviewed and the properties of Fushun shale oil and the developing history and the practical applicability of Fushun oil shale have been discussed. The complete utilization of Fushun oil shale sources has been evaluated.

\* Corresponding Author

Fax: 86-24-56860869

E-Mail: fszxi69@163.com

[a] Liaoning Shihua University, Fushun, Liaoning, P.R. China.

Mineral oils, however, contains in general smaller amounts of unsaturated hydrocarbons, nitrogen or oxygen compounds than shale oil. <sup>6</sup>

## Introduction

Oil shale is a solid-state organic-rich sedimentary and combustible rock with high ash content.<sup>1</sup> Shale oil is derived via pyrolysis of oil shale which is widely distributed throughout the world and contains considerable amounts of heteroatomic compounds and unsaturated hydrocarbons.<sup>2</sup>

As the demand for energy is greatly increasing throughout the world, oil shale, regarded as a potential energy source to substitute for oil and natural gas, has attracted Chinese researchers' attention for many years.<sup>3</sup> There is a considerable amount of oil shale deposits in *Fushun*, which rank the second in *China*. The amount of oil shale in *Fushun* is estimated to be 35 billion tons, and that of shale oil is 7.5 billion tons.<sup>4</sup>

In this paper, the main properties, developing history, and practical applicability of *Fushun* shale oil are reviewed, including a detailed comparison between investment and profit of *Fushun* shale oil.

## Discussion

### Properties of *Fushun* shale oil

*Fushun* shale oil used as feedstock came from Shale Oil Refinery of *Fushun* Ming Group Co., Ltd. Table 1 shows the properties of *Fushun* shale oil samples.<sup>5</sup> The composition and properties include density, kinematic viscosity, wax content, elemental composition, asphaltene content, boiling range, etc., and the ratio of carbon to hydrogen generally varies between 7 and 8, which is very close to the relevant value of petroleum. Shale oil as fuel may become an important substitute of petroleum in the near future.

Shale oil contains a lot of unsaturated hydrocarbons and non-hydrocarbon compounds as well. *Fushun* shale oil has higher nitrogen content than that of *Maoming* or *Estonia*, while *Estonia* shale oil has higher oxygen content than shale oils from other sources.<sup>6</sup>

**Table 1.** Properties of *Fushun* shale oil

Properties	Value
Density (20 °C), g/cm <sup>3</sup>	0.9033
Kinematic viscosity (50 °C), mm <sup>2</sup> /s	11.3
Solidification point, °C	33
Open cup flash point, °C	137
Phenol, %	3.1
Asphaltene, %	0.85
Wax, %	20.0
Resin, % (sulphate process)	42
Carbon residue, %	1.63
Elemental composition, wt%	
C	86.05
H	11.51
O	0.69
S	0.56
N	1.19
C/H	7.49
Basic nitrogen, %	0.6509
Boiling range:	
< 200 °C	3 %
200 °C – 350 °C	35 %
> 350 °C	62 %

*Fushun* shale oil contains less amount of light fraction, e.g. its gasoline fraction content is varied between 2.5 and 2.7 % and the amount of fraction boils below 360 °C is varied between 40 and 50%. Its wax and residual oil content were between 25 and 30% or 20 and 30%, respectively. *Fushun* shale oil belongs to the group of high nitrogen compound containing paraffinic oils with high wax content and setting point, and low asphaltene content.

### The developing history of *Fushun* Shale Oil

Table 3 shows the developing history of *Fushun* shale oil.<sup>7</sup> There were low capacities (50 t/unit) and more numbers of retorting boiler (80 units) at Shale Oil Refinery of *Fushun* Ming Group Co., Ltd. in 1928.

**Table 2** The main processing of oil shale in the world<sup>6</sup>

Country	Place	Oil shale (t/d)	Shale (m/m)	Yield (%)	Production
China	Fushun	100	10-75	65	Fuel, low heat value gas shale ash
Estonia	Kivioli	100	10-100	68	Fuel, chemical production, low heat value gas shale ash
Brazil	Sao Mateus	1500 and 6000	6-50	85-90	Light oil, sulfur, high heat value gas shale semi-coke
Estonia	Narva	3000	0-25	85-90	Fuel, chemical production, high heat value gas shale ash
Australia	Stuart	6000	0-16	85-90	Light fuel, low sulfur light oil, high heat value gas shale ash

Capacities of retorting boiler increased as the years increased until 1956; however the numbers of retorting boiler decreased with the increase of year as shown between 1928 and 1956. On the other hand, capacities and numbers of retorting boiler between 1989 and 1995 kept at 100 t and 20 units, respectively. Numbers of retorting boiler only increased to 160 units in 2002.

**Table 3.** The developing history of Fushun shale oil

Year	Capacity of retorting boiler (t)	Numbers of retorting boiler
1928	50	80
1934	100	80
1939	180	60
1945	200	60
1954	200	60
1956	200	26
1989	100	20
1992	100	20
1995	100	20
2002	100	160

### Comparing between investment and profit of Fushun oil shale

The Tables 4, 5 and 6 show the yields of the products such as shale oil, coal gas and oil shale residue, the consumption of *Fushun* oil shale per ton of product, and the total cost of *Fushun* oil shale per ton, respectively. One ton of oil shale produces 40-42 kg of shale oil, 80-160 kg of coal gas and 800-880 kg of shale oil residue, respectively. Other costs in Table 6 represent the highest cost for *Fushun* oil shale and include maintenance, the replacement or change of new equipment, etc. On the other hand, water consumption is the lowest cost factor.

**Table 4.** The yields of the production (1 ton of oil shale as feedstock)

Name of production	Shale oil	Coal gas	Oil shale residue
Yields (kg)	40-42	80-160	800-880

Table 7 shows the yields of shale oil, oil shale residue and tail mining (small particles of oil shale;  $d \leq 12\text{mm}$ ) per year. *Fushun* oil shale provides different quality fuel materials, fuel gas and raw material for production of various chemicals. The residues of oil shale separation can be used for manufacturing bricks and cement. For example, heating 1 million tons of grounded oil shale at 500 °C produces 3.3 million tons of shale oil, 81.7 million tons of oil shale residual and 17.6 million tons of tail mining, respectively.

**Table 5.** The consumption of Fushun oil shale per ton

Oil shale (t)	Water (t)	Electricity (kWh)	Steam (t)	Gas (Nm <sup>3</sup> )	Energy consumption (MJ)
24-26	7-11	370-400	1.8-2.5	2800-4000	24000

### The practical applicability of *Fushun* oil shale

*Fushun* oil shale can be used directly as fuel in power plants to provide electricity. *Fushun* oil shale can also be separated into shale oil, fuel gas, and oil shale residue. Table 8 shows the chemical compositions of oil shale residue. The oil shale residue can be used to produce brick and cement, and for the recovery of different rare earth elements, such as Si, Al, Fe, Mg and Ca, and to produce different kinds of manure.<sup>8</sup>

### Conclusion

*Fushun* oil shale and shale oil can be used directly as feedstock and fuel to produce high valuable products in order to meet Chinese energy requirements. Utilization of *Fushun* shale oil and oil shale provides less damage to the natural environment and increases the income of a petrochemical plant. The main benefits are as follows: (1) take the place of the traditional energy (coal and petroleum) and protect the local fragile environment; (2) both the local economic development and the local income are improved, as well as more job opportunities are provided.

**Table 6.** Total cost of processing of 1 ton of Fushun oil shale

Name	Oil shale	Material	Management	Salary	Water	Steam	Electricity	Others	Total
Unit/Yuan	61.95	97.30	111.0	93.0	25.00	100.00	123.3	271.73	883.28
Percent (%)	7.01	11.02	12.6	10.5	2.81	11.32	13.96	30.78	100

**Table 7.** The yields of shale oil, oil shale residue and tail mining per year (million tons at 500 °C)

Shale oil	Oil shale residue	Tail mining
3.3	81.7	17.6

**Table 8.** The chemical compositions of oil shale residue

Name	SiO <sub>2</sub>	Al <sub>2</sub> O <sub>3</sub>	Fe <sub>2</sub> O <sub>3</sub>	MgO	CaO
Content (%)	62.23	23.45	9.7	1.41	1.78

## References

- <sup>1</sup> Sun, B. Z., Wang, Q., Shen, P. Y., Qin, H. and Li, S. H. *Oil Shale*, **2012**, 29(1), 63.
- <sup>2</sup> Yu, H., Li, S. Y. and Jin, G. Z. *Oil Shale*, **2010**, 27(2), 126.
- <sup>3</sup> Kang, Z. Q., Yang, D., Zhao, Y. S. and Hu, Y. Q. *Oil Shale*, **2006**, 28(2), 273.
- <sup>4</sup> Hou, X. L. *Petroleum Industry Press*, **1984**.
- <sup>5</sup> Li, G. X., Han, D. Y., Cao, Z. B., Yuan, M. M. and Zai, X. Y. *Oil Shale*, **2011**, 28(3), 372.
- <sup>6</sup> Zhang, Y. M. and You, H. Q. *Eur. Chem. Bull.*, **2012**, 1(5), 170.
- <sup>7</sup> He, H. M., Xu, D. P. and Zhang, X. L. *Clean Coal Technol.*, **2002**, 8(2), 44.
- <sup>8</sup> Chen, X. F., Gao, W. J., Zhao, J., Huang, J. N., Wu, Y. X., Zhang, J. Q., Dou, J. L., Tian, P. J. and Zhang, Z. M. *Clean Coal Technol.*, **2010**, 6, 29.

Received:19.09.2012.  
Accepted:26.09.2012.



# HALOGEN-FREE IONIC LIQUID FOR EXTRACTION AND SIMULTANEOUS DETERMINATION OF Cu(II), Pb(II), Cd(II), AND Hg(II)

Adel F. Shoukry<sup>[a]\*</sup>, Nadia M. Shuaib<sup>[a]</sup>, Rana M. Melhas<sup>[a]</sup>

**Keywords:** Halogen-free ionic liquid; Heavy metals, Solvent extraction, Inductively coupled plasma

A halogen-free ionic liquid, tetraoctylammonium dodecylbenzene sulfonate was used to extract Cu<sup>2+</sup>, Pb<sup>2+</sup>, Cd<sup>2+</sup>, and Hg<sup>2+</sup> from their aqueous solutions by using dithizone as chelating agent. Inductively coupled plasma-mass spectrometry (ICP-MS) was applied, at different pH-values, to simultaneously measure the metal content in the aqueous phase, both before and after extraction. At the optimum pH value, extraction of the four metal cations from pure solution and marine water samples was successfully accomplished and their concentrations were simultaneously determined.

## Corresponding Authors

Tel: +965-24987374; Fax: +965-24816482

E-Mail: [a.shoukry@ku.edu.kw](mailto:a.shoukry@ku.edu.kw); [adelshoukry@gmail.com](mailto:adelshoukry@gmail.com)

[a] Chemistry Department, Faculty of Science, Kuwait University, B.O. Box 5969-Safat, 13060

## Introduction

Liquid-liquid extraction has been extensively employed for recovery and separation of metal ions. The extraction is normally achieved by contacting the aqueous phase with a lipophilic organic liquid containing a metal-selective chelating agent. The organic liquids used in this extraction are generally volatile organic compounds (VOCs). The use of VOCs always faces environmental and safety problems such as emission loss and fire hazard. Therefore, finding alternative materials to replace these solvents has always been of particular interest in providing potential solutions to reduce these problems. Room-temperature ionic liquids (ILs) are a novel class of salts that have engaged exponential attention in recent years due to their negligible vapour pressure. So they have been proposed as environmentally friendly alternatives for the ordinary VOCs. Ionic liquids of imidazolium [C<sub>4</sub>MIM]<sup>+</sup> cation with tetrafluoroborate [BF<sub>4</sub>]<sup>-</sup> and hexafluorophosphate [PF<sub>6</sub>]<sup>-</sup> anions have, so far, been the focus of numerous publications dealing with extraction of metal ions from aqueous samples.<sup>1-10</sup> Nevertheless, classification of such ILs as green solvents has not taken into account the entire life cycle of these solvents, especially those containing [BF<sub>4</sub>]<sup>-</sup> and [PF<sub>6</sub>]<sup>-</sup> anions. These fluorine-based anions have been the subject of extensive debates about the possible eventual decomposition, under certain circumstances, into toxic hydrofluoric acid.<sup>11-16</sup> Further, single-crystal X-ray diffraction studies<sup>17</sup> proved the formation of 1-butyl-3-methylimidazolium fluoride monohydrate complex, [C<sub>4</sub>MIM]F.H<sub>2</sub>O, during preparation and drying of [C<sub>4</sub>MIM][PF<sub>6</sub>]. It has also been reported<sup>18</sup> that in drastic acid medium, [PF<sub>6</sub>]<sup>-</sup> may be converted to [PO<sub>4</sub>]<sup>3-</sup>. This has raised the need for investigating metal-solvent extraction with halogen-free ionic liquids. In the present application, Cu<sup>2+</sup>, Pb<sup>2+</sup>, Cd<sup>2+</sup>, and Hg<sup>2+</sup> cations are extracted as their lipophilic neutral chelates with dithizone into the halogen-

free room temperature ionic liquid, tetraoctylammonium-dodecylbenzene sulfonate ([TOA][DBS]).<sup>19</sup> This ionic liquid is very easy to prepare and, besides being non-expensive; it is also highly lipophilic in nature because of its chemical structure which contains long chains of carbons. The proposed method involves use of a broad spectrum chelating agent and inductively coupled plasma spectroscopy which allow for simultaneous determination of several metals without interference. The method has been applied to determination of Cu<sup>2+</sup>, Pb<sup>2+</sup>, Cd<sup>2+</sup>, and Hg<sup>2+</sup> in pure solution and in marine water samples taken from Kuwait coastal area that is exposed to high anthropogenic activity.

## Experimental

### Reagents

Chloroform, acetonitril (ACN, Merck); dithizone (DT) (Fluka); nitrate salts of Cu(II), Pb(II), Cd(II) and Hg(II) (Merck); tetraoctylammonium bromide (TOABr) (Aldrich); and sodium dodecylbenzenesulfonate (NaDBS) (Aldrich) were used. The chemical composition of the ionic liquid was checked by using proton NMR. [<sup>1</sup>H-NMR (CDCl<sub>3</sub>, C<sub>42</sub>H<sub>97</sub>NO<sub>3</sub>S), 7.76(d, 2H, J 8.0 Hz), 7.09(d, 2H, H 8.0), 2.91(m, 8H), 1.63 - 0.79 (m, 85 H)].

Borate, phosphate and ammoniacal buffers were used to adjust the PH-value of the solutions.

### Preparation of the ionic liquid

The synthesis of the ionic liquid, tetraoctylammonium-dodecylbenzene-sulfonate [TOA][DBS] was similar to that described elsewhere.<sup>19</sup> Briefly, equimolar (0.1 M) TOABr and NaDBS were mixed in 1:1 (water + acetone) solvent. The mixture was stirred on hot until acetone evaporated completely. The mixture was transferred to a separating funnel and the aqueous phase was removed. The resultant crude [TOA][DBS] oil was purified by shaking with water several times. The ionic liquid was then dried with anhydrous sodium sulfate.

### 2.3. Sampling and sample preparation of seawater

A mechanized boat with a towing speed maintained at  $0.3 \text{ m s}^{-1}$  was employed to collect samples from Doha coastal area (Fig. 1). The samples were collected in sterile (5 L) plastic bottle from 5-m depth using Vandorn water sampler. The water was filtered in a  $0.45 \mu\text{m}$  membrane filter and eluted. To about one liter of the filtrate, 25 mL ammonium pyrrolidinedithiocarbamate, 10 mL 3M HCl, and 25-mL methyl isobutyl ketone, were added in a separating funnel. The mixture was shaken for 2 minutes, and then left undisturbed for 20 minutes. Two separate phases, namely, upper and lower solutions (A, and B, respectively) were built. Solution (A) was added with one liter seawater and the above chemicals, and then the process was repeated. Likewise, the lower solution (B) was treated in another separating funnel and eluted. The resultant upper solutions from both (A) and (B) were collected in a 50-mL volumetric flask and the lower solutions were discarded. The resultant upper solution was analyzed by inductively coupled plasma-mass spectrometry (ICP-MS) to obtain the extract content of the concerned metals, both before and after extraction with the halogen-free ionic liquid.



**Figure 1.** Map of Kuwait with sampling station (Doha village) indicated.

### Apparatus

Inductively coupled plasma-mass spectrometric measurements were performed with a Varian 820-MS spectrophotometer. UV-visible spectra were measured with a Cary-5 spectrophotometer. The pH value of the extraction systems was measured with an Orion, Model 420A pH/mV meter.

### Liquid-liquid extraction of metal-dithizone complex

Accurately weighed amount of dithizone (DT) was dissolved in a 100 mL of ACN : water mixture (10:90, v/v) to form a  $3.4 \times 10^{-4} \text{ M}$  dithizone solution. In two separating funnels, 10 mL each, the following mixtures were prepared:

1) 0.50 mL of the DT solution  $8.4 \times 10^{-4} \text{ M}$  + 2.25 mL bidistilled water + 4.5 mL of the buffer solution + 1.0 mL of [TOA][DBS].

2) 0.50 mL of the DT solution  $8.4 \times 10^{-4} \text{ M}$  + 2.25 mL metal ion solution (25 ppm) or metal ion solution mixture + 4.5 mL of the buffer solution + 1.0 mL of [TOA][DBS].

Each of the two mixtures was shaken for 15 minutes and then left to stand for 10 minutes. Visible spectra were run for each of the two ionic liquid layers. Different volumes of acid solution were then added to the ionic liquid to strip the metal ion(s) from it. The acid solution was then removed, diluted (if necessary), and measured with ICP-MS to determine the metal ion(s) content. The recovery factor was calculated after correcting for dilution.

### 2.6. Effect of pH- value on the Extraction efficiencies of metal ions with [TOA][DBS]

The efficiency rates of the extraction of each of Cu(II)-, Pb(II)-, Cd(II)- and Hg(II)-dithizone chelates using the halogen-free ionic liquid were determined at different pH-values of the aqueous layer. This was done by mixing 0.50 mL of  $8.4 \times 10^{-4} \text{ M}$  DT solution + 2.25 mL metal ion solution (25 ppm) or metal ion solution mixture + 4.5 mL of the buffer solution + 1.0 mL of [TOA][DBS]. The biphasic system was shaken to ensure complete mixing and then centrifuged to separate the two phases after extraction. The upper aqueous phase was taken out and measured with inductively coupled plasma spectrometry to determine the concentration of metal ions that were left in the aqueous phase. Extraction coefficients (E) were calculated by:

$$E(\%) = \frac{(C_i)_{aq} - (C_f)_{aq}}{(C_i)_{aq}} 100 \quad (1)$$

where  $(C_i)_{aq}$  and  $(C_f)_{aq}$  are the concentration of metal ions in aqueous phase before and after extraction, respectively.

For each of the metal cations, a parallel experiment was performed by using the traditional solvent, chloroform.

## Results and discussion

### Spectrophotometric investigation of the extraction process

Dithizone was chosen as organic extractant because of its known efficiency in the field of quantitative chemical analysis.<sup>20-23</sup> Moreover it has been used previously for solvent extraction with imidazolium-based ionic liquid.<sup>24</sup> Spectra of dithizone and the complexes of dithizone with Hg(II), Pb(II), Cd(II), and Cu(II) in the ionic liquid [TOA][DBS] are shown in Fig. 2. The results indicate that the characteristic absorption peak of dithizone in [TOA][DBS] (Fig.2a) suffers hyperchromicity associated with a shift of bands to shorter wavelengths (hypsochromic shift) (Fig. 2 b-e). This clearly reveals the efficiency of the employed halogen-free ionic liquid as extracting agent for the concerned metals.

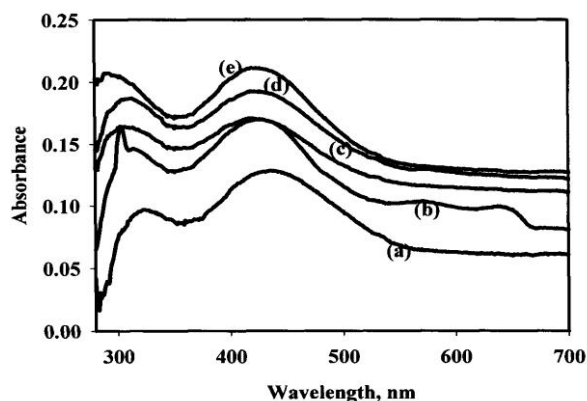


**Figure 2.** Absorption spectra of dithizone (a) and its chelates with divalent Cu (b), Cd (c), Pb (d), and Hg (e) in [TOA][DBS] ionic liquid after extraction from aqueous solutions buffered at pH 7.0.

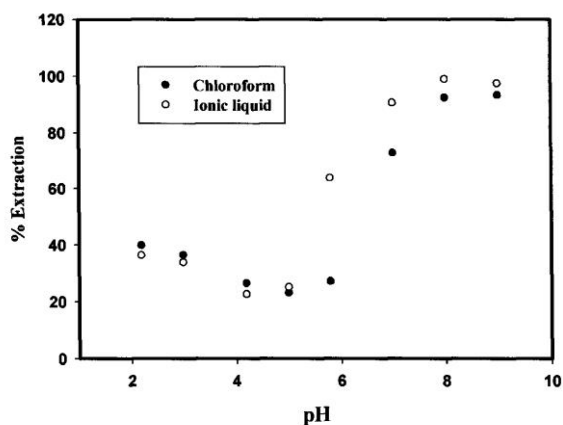


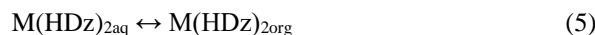
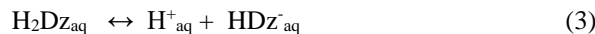
**Figure 3.** Effect of pH value of the aqueous layer on the extraction percentage of Pb(II).

#### Extraction of metal ion with [TOA][DBS] in comparison to chloroform

The extraction percentage of Pb(II), at different pH values was calculated by inductively coupled plasma spectrometric analysis of the aqueous phase before and after extraction. Fig. 3 shows the variations of this percentage for Pb(II) as a function of pH on using the ionic liquid (Fig. 3a) and on using the traditional solvent, chloroform (Fig. 3b). The results indicate that the extraction of lead was better using ionic liquid than chloroform. Similar trend was shown in case of Cu(II), Cd(II) and Hg(II).

From Fig. 3, it is evident that the extraction is most efficient at pH 7-9 on using either chloroform or the ionic liquid. Moreover the extraction of Pb(II) with the ionic liquid [TOA][DBS] is distinctly more efficient than with the traditional solvent, chloroform. Figures with similar trends were obtained for extraction of Hg(II), Cu(II) and Cd(II) with extraction exceeding 95% within the pH range 7 to 9. This is due to formation of dithizonate at these pH values which are fairly above the  $pK_a$  of dithizone ( $5.77 \pm 0.25$ ).<sup>25</sup>

The various equilibrium reactions that govern the extraction of M(II)-dithizonates are shown in the following:



The overall extraction equilibrium is the sum of the above four reactions:



The equilibrium constant for this reaction is:

$$K = \frac{[M(HDz)_2]_{org} [H^+]_{aq}^2}{[H_2Dz]_{org} [M^{2+}]_{aq}} \quad (7)$$

$$\frac{[M(HDz)_2]_{org}}{[M^{2+}]_{aq}} = K \frac{[H_2Dz]_{org}}{[H^+]_{aq}} \quad (8)$$

It is evident from equation (8) that the ratio of concentration of the metal species in the two layers is directly proportional to K and  $[H_2Dz]_{org}^2$  and inversely proportional to  $[H^+]_{aq}^2$ . The equilibrium constant K varies widely from one metal ion to another; these differences often make it possible to selectively extract one cation from another by buffering the aqueous phase at a level where one of them is extracted nearly completely and the second remains largely in the aqueous phase. In the present work sufficiently high pH value buffering was applied so that all metals can be determined simultaneously by using the ICP-MS technique (Table 1). This offers a rapid and highly precise method for analysis of metal ions matrix.

#### Extraction of the metals from their mixtures and from marine water sample

The feasibility for the simultaneous determination of cations in binary, ternary, and quaternary mixtures by ICP-MS spectrometry following liquid/liquid extraction with halogen-free IL was examined. For this purpose binary, tertiary, and quaternary mixtures of  $Cu^{2+}$ ,  $Pb^{2+}$ ,  $Cd^{2+}$ , and  $Hg^{2+}$  have been prepared in which concentration of each of the cations in the mixture was 20 ppm. The results shown in Table 1 reveal high recovery rates for individual metal cations; this efficiency of the method does not decrease for the analysis of the metals in their binary, ternary or quaternary mixture. The method was then applied to marine water sampled from El-Doha coastal area (Fig. 1) which is an industrial area where desalination and power plants are located. The results revealed extraction percentages of 99.3, 97.8, 97.5, and 99.6 % of Cu(II), Pb(II), Cd(II), and Hg(II), respectively, from the sample.

**Table 1.** ICP determination of Cu(II), Pb(II), Cd(II), and Hg(II) single and in mixtures after extraction with the halogen-free ionic liquid.

Single Cation		Binary Mixture			Ternary Mixture			Quaternary Mixture		
Cation	(%)*	Mixture	Cation	(%)*	Mixture	Cation	(%)*	Mixture	Cation	(%)*
Cu	93.1	Cu,Pb	Cu	98.3	Cu, Pb, Cd	Cu	98.7	Cu, Pb, Cd, Hg	Cu	98.1
			Pb	98.0		Pb	99.8			
		Cu,Cd	Cu	97.8	Cd	99.6				
			Cd	99.8	Cu, Pb, Hg	Cu	97.9			
Pb	98.8	Cu,Hg	Cu	99.4	Cu, Pb, Hg	Pb	99.4		Pb	99.8
			Hg	97.5		Hg	97.6			
		Pb,Cd	Pb	99.1		Cu, Cd, Hg	Cu			
Cd	99.6		Cd	99.9						
Cd	99.4	Pb,Hg	Pb	99.6	Pb, Cd, Hg	Hg	99.3	Cd	99.8	
			Hg	98.5		Pb	99.9			
		Cd,Hg	Cd	99.6		Cd	99.9			
Hg	97.8		Hg	97.1						

\*Percent extraction

## Conclusion

The use of inductively coupled plasma-mass spectrometry technique enables simultaneous determination of Cu(II), Pb(II), Cd(II), and Hg(II) cations both in their aqueous solution and in marine water. The application requires extraction of the concerned metals with the halogen-free room temperature ionic liquid [TOA][DBS] in presence of dithizone as chelating agent.

## Acknowledgment

The support of Kuwait University received through the Research Administration (project no. 02/10) is gratefully acknowledged. We also thank the Science Analytical Facilities (SAF), Kuwait University, Faculty of Science, for the analyses of our samples using ICP-Ms (GS01/05) and NMR (GS01/01)

## References

- Dai, S., Ju, Y. H., Barnes, C. E., *J. Chem. Soc. Dalton Trans.*, **1999**, 1201.
- Visser, A. E., Swatloski, R. P., Griffin, S. T., Hartman, D. H., Rogers, R. D., *Sep. Sci. Technol.* **2001**, *36*, 785.
- Visser, A. E., Swatloski, R. P., Reichert, W. M., Griffin, S. T., Hartman, D. H., Rogers, R. D., *Ind. Eng. Chem. Res.*, **2001**, *39*, 4596.
- Wei, G. T., Yang, Z., Chen, C. J., *Anal. Chim. Acta*, **2003**, *488*, 183.
- Dietz, M. L., *Sep. Sci. Technol.*, **2006**, *41*, 2047.
- Luo, H., Dai, S., *Separation of metal ions based on ionic liquids. In: Ionic Liquids in Chemical Analysis*. Taylor & Francis, USA, **2008**.
- Domanska, U., Rekawek, A., *J. Solution Chem.*, **2009**, *38*, 739.
- Germani, R., Mancini, M. V., Savelli, G., Spreti, N., *Tetrahedron Lett.* **2007**, *48*, 1767.
- Zhao H., Xia, S., Ma, P., *J. Chem. Technol. Biotechnol.* **2005**, *80*, 1089.
- Liu, J., Jonsson, J. A., Jiang, G., *Trends in Anal. Chem.*, **2005**, *24*, 20.
- Huddleston, J. G., Visser, A. E., Reichert, W. M., Willauer, H. D., Broker, G. A., Rogers, R. D., *Green Chem.*, **2001**, *3*, 156.
- Gubicza, L., Nemestoyhy, N., Frater, T., Belafi-Bako, K., *Green Chem.*, **2003**, *5*, 236.
- Tseng, M., Liang, Y., Chu, Y., *Tetrahedron Lett.*, **2005**, *46*, 6131.
- Nikitenko, S. I., Berthon, C., Moisy, P.C. R., *Chimie*, **2007**, *10*, 1122.
- Archer, D. G., Widegreen, J. A., Kirklin, D. R., Magee, J. W., *J Chem. Eng. Data*, **2005**, *50*, 1484.
- Najdanovic-Visak, V., Esperanca, J. M. S. S., Rebelo, L. P. N., Nunes da Ponte, M., Guedes, H. J. R., Seddon, K. R., Szydowski, J., *J. Phys. Chem. Chem. Phys.*, **2002**, *4*, 1701.
- Swatloski, R. P., Holbery, J. D., Rogers, R. D., *Green Chem.*, **2003**, *5*, 361.
- Visser, A. E., Swatloski, R. P., Reichert, W. M., Griffin, S. T., Rogers, R. D., *Ind. Eng. Chem. Res.*, **2000**, *39*, 3596.
- Tsukatani, T., Katano, H., Tatsumi, H., Deguchi, M., Hirayama, N., *Anal. Sci.*, **2006**, *22*, 199.
- Kolthoff, J. M., Sandell, E. B., Mechan, E. J., Bruckenstein, S., *Quantitative Chemical Analysis*, 4<sup>th</sup> edition, The Macmillan Company, NY. **1969**.
- Marczenko, Z., *Spectrophotometric Determination of Elements*, John Wiley and Sons Inc., USA. **1976**.
- Onishi, H., *Photometric Determination of Traces of Metals – Part IIB: Individual Metals, Magnesium to Zirconium*, 4<sup>th</sup> edition, John Wiley & Sons, Inc., USA. **1989**.
- Harris, D., *Quantitative Chemical Analysis*, 5<sup>th</sup> Edn., p.644, Freeman, NY. **1998**.
- Domanska, U., Rekawek, A., *J. Solution Chem.*, **2009**, *38*, 739-751.
- Irving, H., Cooke, S. J. H., Woodger, S. C., William, R. J. P., *J. Chem. Soc.*, **1949**, 1847.

Received: 15.09.2012.

Accepted: 27.09.2012.





# NEW COMPLEXES OF UREA WITH Hg(II) AND Ni(II) METAL IONS

Omar B. Ibrahim<sup>[a]</sup>, Moamen S. Refat<sup>[a,b]\*</sup>, Mahmoud Salman<sup>[c]</sup> and M. M. Al-Majthoub<sup>[a,c]</sup>

**Keywords:** Urea, Hg(II), Ni(II), Biological activity, Spectroscopic studies, Thermal analysis.

The complexation of urea (U) with mercury(II) and nickel(II) ions at room temperatures and 60 °C has been studied by many methods namely elemental analysis, magnetic susceptibility, conductivity measurements, infrared and thermal analysis (TG/DTG), scanning electron microscopy (SEM), Energy-dispersive X-ray spectroscopy (EDX), and x-ray powder diffraction (XRD) method. The physical and spectral data were well explained in terms of the formation of HgCl<sub>2</sub>·4U·2H<sub>2</sub>O (**1**) and Ni(NO<sub>3</sub>)<sub>2</sub>·2U·2H<sub>2</sub>O (**2**) at room temperature, on one hand, and HgCl<sub>2</sub>·2U·2H<sub>2</sub>O (**3**) and on the other hand Ni(NO<sub>3</sub>)<sub>2</sub>·2U·H<sub>2</sub>O (**4**) at 60 °C. On the basis of the infrared spectral data and the values of stretching vibrational bands of both –C=O and –NH<sub>2</sub> groups, the complexation of metal ions toward urea was distinguished. The enhancement of the microbial treatments against bacteria (*Escherichia Coli*, *Staphylococcus Aureus*, *Bacillus subtilis* and *Pseudomonas aeruginosa*) and fungi (*Aspergillus Flavus* and *Candida Albicans*) was assessed and a remarkable efficiency was recorded for complexes (**1**) and (**2**).

\* Corresponding Authors

E-Mail: msrefat@yahoo.com

- [a] Department of Chemistry, Faculty of Science, Taif University, Al-Hawiah, Taif, P.O. Box 888 Zip Code 21974, Saudi Arabia  
 [b] Department of Chemistry, Faculty of Science, Port Said University, Port Said, Egypt  
 [c] Department of Chemistry, Faculty of Science, Al-Hussein Bin Talal University, P.O. Box 20 Ma'an, Jordan

ligand through the oxygen atom, forming a C=O · · · M bond. The rare N,O-bidentate coordination mode has been observed in a very limited number of cases.<sup>19-22</sup>

Raman and infrared spectra of urea have been studied by several scientists.<sup>23-33</sup>

Urea possesses two types of potential donor atoms, the carbonyl oxygen and amide nitrogens. Penland et al.<sup>34</sup> studied the infrared spectra of urea complexes to determine whether coordination occurs through oxygen or nitrogen atoms. If coordination occurs through nitrogen CO stretching frequency is expected to increase with a decrease of CN stretching frequency, the NH stretching frequency in this case may fall to the same range as those of the amido complexes.

On the other hand if coordination occurs through oxygen CO stretching frequency decreases but with no appreciable change in NH stretching frequency. Since the vibrational spectrum of urea itself has been analysed,<sup>32</sup> band shifts caused by coordination can easily be checked, for example, the effect of the coordination on the spectra of the complexes of urea with Pt(II) and Cr(III) in which the coordination occurs through nitrogen and oxygen atoms, respectively.<sup>34</sup> The mode of coordination of urea with metal ions seems to be dependent upon the type and nature of metal ions. Pd(II) coordinates to the nitrogen, whereas Fe(III), Zn(II), and Cu(II) coordinate to the oxygen of urea.<sup>34</sup>

In urea-metal complexes, if a nitrogen-to-metal bond is present, the vibrational spectrum of this complex differs significantly from that of the free urea molecule. The N-H stretching frequencies would be shifted to lower values, and the C=O bond stretching vibration, ( $\nu(\text{C}=\text{O})$ ) would be shifted to higher frequency at about 1700cm<sup>-1</sup>.<sup>35</sup>

Recently, urea represents not only an important molecule in biology<sup>36</sup> but also an important raw material in chemical industry.<sup>37</sup>

## Introduction

Urea, CH<sub>4</sub>N<sub>2</sub>O, a white solid which melts at 132°C, soluble in water and ethanol, but insoluble in ether was first prepared by Wöhler<sup>1</sup> by evaporating a solution containing a mixture of potassium isocyanate and ammonium sulphate. Ammonium isocyanate, which is formed first, undergoes molecular rearrangement to give urea, as shown by the following reaction;



Urea can be prepared in the laboratory by the reaction of ammonia with carbonyl chloride, alkyl carbonates, chloroformates or urethans. Industrially urea is used<sup>2-4</sup> for preparing various formaldehyde-urea resins (plastics),<sup>5</sup> barbiturates<sup>6</sup>, and fertilizers.<sup>7-10</sup> Urea is also extensively used in the paper industry to soften cellulose and has been used to promote healing in infected wounds and also in many other applications in the field of medicine.<sup>11-13</sup> Recently, urea is used for the manufacture of hydrazine in which it is treated with alkaline sodium hypochlorite<sup>6</sup> and with reactive dyeing.<sup>14</sup>

Complexes of urea with some metal ions such as [Zn(urea)<sub>6</sub>]SO<sub>4</sub>·H<sub>2</sub>O and [Zn((urea)<sub>4</sub>](NO<sub>3</sub>)<sub>2</sub>·2H<sub>2</sub>O are used as fertilizers<sup>15-18</sup>. Crystal structure studies of urea showed that in solid urea, both of the nitrogen atoms are identical.<sup>6</sup> Urea usually coordinates as a monodentate

## Experimental

### Materials

HgCl<sub>2</sub>, Ni(NO<sub>3</sub>)<sub>2</sub>·6H<sub>2</sub>O and methanol were obtained from Aldrich Company. Urea was received from Fluka chemical company. All chemicals used in this study were of analytical grade and they were used as such without further purification.

### Synthesis of Hg(II) and Ni(II) urea complexes

#### *Synthesis of urea complexes at room temperature*

The complexes with composition of HgCl<sub>2</sub>·4U·2H<sub>2</sub>O (**1**) and Ni(NO<sub>3</sub>)<sub>2</sub>·2U·2H<sub>2</sub>O (**2**), were prepared by mixing equal aqueous solutions of HgCl<sub>2</sub> (2.72 g, 0.01 mole) and Ni(NO<sub>3</sub>)<sub>2</sub>·6H<sub>2</sub>O (2.90 g, 0.01 mole) in 25 mL distilled water with a 50 mL volume of urea solution (6.0 g, 0.1 mole) in methanol. The mixtures were stirred for about 12 hours under refluxed system at room temperature *ca.* 25 °C. The amount of the precipitate so formed was increased with increasing with the time. The precipitated complex so formed was filtered off, dried under *vacuo* over anhydrous calcium chloride.

#### *Synthesis of urea complexes at 60 °C temperature*

The urea complexes, HgCl<sub>2</sub>·2U·2H<sub>2</sub>O (**3**) and Ni(NO<sub>3</sub>)<sub>2</sub>·2U·H<sub>2</sub>O (**4**), were prepared by a method similar to that of described for the preparation of urea complexes at room temperature. A 25 mL volume of urea solution (6.0g, 0.1 mole) in methanol was mixed with an equal volume of HgCl<sub>2</sub> (2.72 g, 0.01 mole) and Ni(NO<sub>3</sub>)<sub>2</sub>·6H<sub>2</sub>O (2.90 g, 0.01 mole) and with 25 mL of distilled water. The mixtures were stirred for about 2 hours and then heated to 60 °C for 6 hours on a water bath under refluxed system. The precipitated products were filtered, dried at 60 °C in an oven for 3 hours.

### Measurements

The elemental analysis of carbon and hydrogen contents were performed by the microanalysis unit at Cairo University, Egypt, using a Perkin Elmer CHN 2400 instrument. The conductivities of freshly prepared 1.0×10<sup>-2</sup> g/5 cm<sup>3</sup> dimethylformamide (DMF) solutions were measured for the soluble urea complexes using Jenway 4010 conductivity meter. Magnetic measurements were performed on the Magnetic Susceptibility Balance, Sherwood Scientific, and Cambridge Science Park-Cambridge-England. The infrared spectra with KBr discs were recorded on a Bruker FT-IR Spectrophotometer (4000–400 cm<sup>-1</sup>). The thermal studies TG/DTG–50H were carried out on a Shimadzu thermogravimetric analyzer under static air till 800 °C. Scanning electron microscopy (SEM) images and Energy Dispersive X-ray Detection (EDX) were taken in Joel JSM-6390 equipment, with an accelerating voltage of 20 KV. The X-ray diffraction patterns for the urea complexes were recorded on X'Pert PRO PANalytical X-ray powder diffraction, target copper with secondary monochromate.

### Antibacterial and antifungal activities

Antimicrobial activity of the tested samples was determined using a modified Kirby-Bauer disc diffusion method.<sup>38</sup> Briefly, 100 µl of the best bacteria/fungi were grown in 10 mL of fresh media until they reached a count of approximately 10<sup>8</sup> cells/mL for bacteria and 10<sup>5</sup> cells/mL for fungi.<sup>39</sup> 100 µl of microbial suspension was spread onto agar plates corresponding to the broth in which they were maintained. Isolated colonies of each organism that might be playing a pathogenic role should be selected from primary agar plates and tested for susceptibility by disc diffusion method.<sup>40,41</sup>

Of the many media so available, National Committee for Clinical Laboratory Standards (NCCLS) recommends Mueller-Hinton agar due to main reasons that: it results in good batch-to-batch reproducibility. Disc diffusion method for filamentous fungi tested by using approved standard method (M38-A) developed by the NCCLS<sup>42</sup> for evaluating the susceptibility of filamentous fungi to antifungal agents.

Disc diffusion method for yeast developed standard method (M44-P) by the NCCLS.<sup>43</sup> Plates inoculated with filamentous fungi as *Aspergillus Flavus* at 25 °C for 48 hours; Gram (+) bacteria as *Staphylococcus Aureus*, *Bacillus subtilis*; Gram (-) bacteria as *Escherichia Coli*, *Pseudomonas aeruginosa* they were incubated at 35-37 °C for 24-48 hours and yeast as *Candida Albicans* incubated at 30 °C for 24-48 hours and, then the diameters of the inhabitation zones were measured in millimetres.<sup>38</sup> Standard discs of Tetracycline (Antibacterial agent), Amphotericin B (Antifungal agent) served as positive controls for antimicrobial activity but filter disc impregnated with 10 µl of solvent (distilled water, chloroform, DMSO) were used as a negative control.

The agar so used is Mueller-Hinton agar that is rigorously tested for composition and pH. Further the depth of the agar in the plate is a factor to be considered in the disc diffusion method. This method is well documented and standard zones of inhabitation have been determined for susceptible values. Blank paper disks (Schleicher & Schuell, Spain) with a diameter of 8.0 mm were impregnated 10 µl of tested concentration of the stock solutions. When a filter paper disc impregnated with a tested chemical is placed on agar the chemical will diffuse from the disc into the agar. This diffusion will place the chemical in the agar only around the disc. The solubility of the chemical and its molecular size will determine the size of the area of chemical infiltration around the disc. If an organism is placed on the agar it will not grow in the area around the disc if it is susceptible to the chemical. The area of no growth around the disc is known as a "Zone of inhibition" or "Clear zone". For the disc diffusion, the zone diameters were measured with slipping calipers of the National for Clinical Laboratory Standards.<sup>400</sup>

Agar-based methods such as Etest disk diffusion can be good alternatives because they are simpler and faster than broth the methods.<sup>44,45</sup>

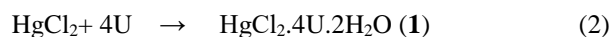
**Table 1:** Physical characterization, micro-analytical and molar conductance data of urea complexes

Empirical formula (MW.)	Color	Molar ratio	Elemental analysis (%)		Λ <sub>m</sub> (Ω <sup>-1</sup> cm <sup>2</sup> mol <sup>-1</sup> )
			Found (Calcd.)	C	
HgCl <sub>2</sub> .4U.2H <sub>2</sub> O (1) 547.5 g/mol	White	1:4	08.89 (08.78)	03.22 (03.91)	13
Ni(NO <sub>3</sub> ) <sub>2</sub> .2U.2H <sub>2</sub> O (2) 338.85 g/mol	Light green	1:4	07.16 (07.08)	04.50 (03.54)	215
HgCl <sub>2</sub> .2U.2H <sub>2</sub> O (3) 427.5 g/mol	White	1:4	05.68 (05.61)	02.80 (02.80)	-
Ni(NO <sub>3</sub> ) <sub>2</sub> .2U.H <sub>2</sub> O (4) 320.85 g/mol	Light green	1:4	07.39 (07.48)	04.30 (03.11)	-

## Results and Discussion

The color, physical characteristics, micro-analytical data, molar conductance measurements of Hg(II) and Ni(II) urea complexes are given in Table 1. The elemental analysis data of some prepared complexes revealed 1:4 molar ratio (M:U) (where M= Hg(II), Ni(II) and U= urea) are in a good agreement with the general formulas HgCl<sub>2</sub>.4U.2H<sub>2</sub>O (1), Ni(NO<sub>3</sub>)<sub>2</sub>. 2U.2H<sub>2</sub>O (2), HgCl<sub>2</sub>.2U.2H<sub>2</sub>O (3) and Ni(NO<sub>3</sub>)<sub>2</sub>. 2U. H<sub>2</sub>O (4). It is important to mention that complexes 1, and 2 were prepared at room temperature but complexes 3 and 4 were resulted from the chelation of urea with Hg(II) and Ni(II) ions at 60 °C with molar ratio of urea:metal=4:1. The reactions can be represented by the stoichiometric equations:

Reactions at 25 °C:



Reactions at 60 °C



The complexes are air-stable, hygroscopic, with low melting points, soluble in H<sub>2</sub>O and dimethylformamide. The conductivities of 10<sup>-2</sup> g/5 ml solutions of the prepared complexes in DMF (Table 1) indicate that the complexes have an electrolytic nature.

### Conductivity measurements

The conductivity values for the urea complexes in DMF solvent (10<sup>-2</sup> g/5 ml solution) are 13 and 215 Ω<sup>-1</sup> cm<sup>2</sup> mol<sup>-1</sup> for complexes (1) and (2) respectively suggesting them to be electrolytes (Table 1). Conductivity measurements have frequently been used in structures of metal complexes (mode of coordination) within the limits of their solubility. They provide a method of testing the degree of ionization of the complexes, the molar ions that a complex liberates in solution (in case of presence anions outside the coordination sphere), the higher will be

its molar conductivity and vice versa. It is clear from the conductivity data that the complex (1) seems to be more electrolyte in nature than complex (2).

Also the molar conductance values indicate that the anions present outside the coordination sphere. This result was confirmed from the elemental analysis data where Cl<sup>-</sup> or NO<sub>3</sub><sup>-</sup> ions are precipitated or colored by adding of AgNO<sub>3</sub> or FeSO<sub>4</sub> solutions, respectively, this experimental test is a good matched with CHN data. Both these complexes have electrolytic properties. This fact elucidated that the Cl<sup>-</sup> or NO<sub>3</sub><sup>-</sup> are present. These results establish the stoichiometry of these complexes, which are in agreement with the general formulas were suggested.

### Magnetic measurements

Magnetic measurements were carried out on a Sherwood Scientific magnetic balance according to the Gauy method. The calculations were evaluated by applying the following equations:

$$\chi_g = \frac{c(R - R_o)}{10^9 M} \quad (6)$$

$$\chi_m = \chi_g MWt \quad (7)$$

$$\mu_{\text{eff}} = 2.828 \sqrt{\chi_m T} \quad (8)$$

where

$\chi$  is mass susceptibility per gm sample,

$c$  is the calibration constant of the instrument and equal to 0.0816

$R$  is the balance reading for the sample and tube

$R_o$  is the balance reading for the empty tube

$M$  is the weight of the sample in gm

$T$  is the absolute temperature

The magnetic moments of Ni(NO<sub>3</sub>)<sub>2</sub>.2U.2H<sub>2</sub>O (2) and Ni(NO<sub>3</sub>)<sub>2</sub>.2U.H<sub>2</sub>O (4) complexes at T= 300 K and were calculated. The observed values of the effective magnetic moments  $\mu_{\text{eff}}$  measured were found to be 3.73 B. M. and 2.96 BM. for complexes (2) and (4), respectively, this is convenient with experimental values of 3.32 B.M. obtained<sup>46</sup> for octahedral Ni(II) complexes with sp<sup>3</sup>d<sup>2</sup> hybridization for both Ni(II)/U complexes.

### Infrared spectra

The infrared spectra of the Hg(II) and Ni(II) urea complexes at room temperature and at 60 °C are shown in Fig. 1. The band locations were measured for the mentioned urea complexes, together with the proposed assignments for the most characteristic vibrations are presented in Tables 2 and 3. In order to facilitate the spectroscopic analysis and to put our hand on the proper structure of the prepared complexes, the spectra of the urea complexes were accurately compared with those of the urea and similar complexes in literature. The discussion of the spectra will be addressed on the basis of the most characteristic vibrations.

**Table 2:** Characteristic infrared frequencies ( $\text{cm}^{-1}$ ) and tentative assignments of urea (U),  $[\text{Pt}(\text{urea})_2\text{Cl}_2]$  (A),  $[\text{Cr}(\text{urea})_6]\text{Cl}_3$  (B),  $\text{HgCl}_2 \cdot 4\text{U} \cdot 2\text{H}_2\text{O}$  (1) and  $\text{Ni}(\text{NO}_3)_2 \cdot 2\text{U} \cdot 2\text{H}_2\text{O}$  (2) complexes

Urea	A	B	1	2	Assignments <sup>(b)</sup>
3450	3390	3440	3462	3460	$\nu(\text{OH}); \text{H}_2\text{O}$
	3290	3330	3357	3333	$\nu_{\text{as}}(\text{NH}_2)$
3350	3130	3190	-	3361	$\nu_{\text{s}}(\text{NH}_2)$
	3030				
			1613	1628	$\delta(\text{H}_2\text{O})$
1683	1725	1505	1667	1660	$\delta(\text{C}=\text{O})$
1471	1395	1505	1447	1462	$\nu(\text{C}-\text{N})$

The assignments of full vibrational analysis of crystalline urea have been published.<sup>34</sup> Tables 2 and 3 give diagnostic infrared peaks of the free urea ligand, published work Hg(II) and Ni(II) complexes. Assignments have been given in comparison with the data obtained for the free urea, that is, uncoordinated, U and its  $[\text{Pt}(\text{urea})_2\text{Cl}_2]$  and  $[\text{Cr}(\text{urea})_6]\text{Cl}_3$  complexes.<sup>34</sup> The effect of the coordination on the spectra of the complexes of urea with  $[\text{Pt}(\text{urea})_2\text{Cl}_2]$  and  $[\text{Cr}(\text{urea})_6]\text{Cl}_3$  complexes in which the coordination occurs through nitrogen and oxygen atoms, respectively.<sup>34</sup> The mode of coordination of urea with metal ions seems to be dependent upon the type and nature of metal. Pt(II) ions in  $[\text{Pt}(\text{urea})_2\text{Cl}_2]$  coordinate to the nitrogen, whereas Fe(III), Zn(II), and Cu(II) coordinate to the oxygen of urea.<sup>34</sup>

**Table 3:** Characteristic infrared frequencies ( $\text{cm}^{-1}$ ) and tentative assignments of urea (U),  $[\text{Pt}(\text{urea})_2\text{Cl}_2]$  (A),  $[\text{Cr}(\text{urea})_6]\text{Cl}_3$  (B),  $\text{HgCl}_2 \cdot 2\text{U} \cdot 2\text{H}_2\text{O}$  (3) and  $\text{Ni}(\text{NO}_3)_2 \cdot 2\text{U} \cdot \text{H}_2\text{O}$  (4) complexes

Urea	A	B	3	4	Assignments <sup>(b)</sup>
3450	3390	3440	3462	3454	$\nu(\text{OH}); \text{H}_2\text{O}$
	3290	3330	3358	3347	$\nu_{\text{as}}(\text{NH}_2)$
3350	3130	3190	2361	3233	$\nu_{\text{s}}(\text{NH}_2)$
	3030				
			1617		$\delta(\text{H}_2\text{O})$
1683	1725	1505	1668	1655	$\delta(\text{C}=\text{O})$
1471	1395	1505	1448	1473	$\nu(\text{C}-\text{N})$

For all the prepared complexes, the coordination mode take place *via* oxygen of amide group, the positively charged metal ion stabilizes the negative charge on the oxygen atom; the NCO group now occurs in its polar resonance form and the double bond character of the CN bond increases or still not affected, while the double bond character of the CO bond decreases, resulting in an

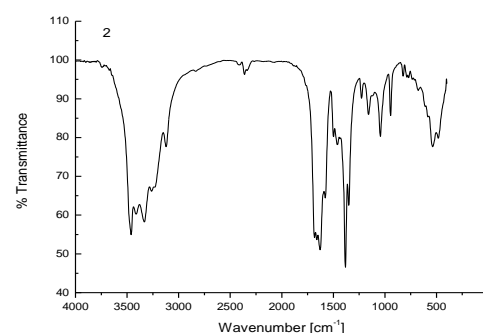
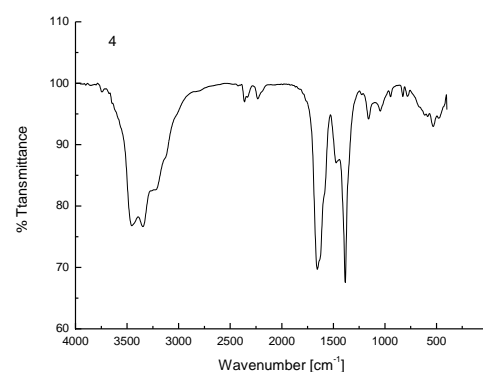
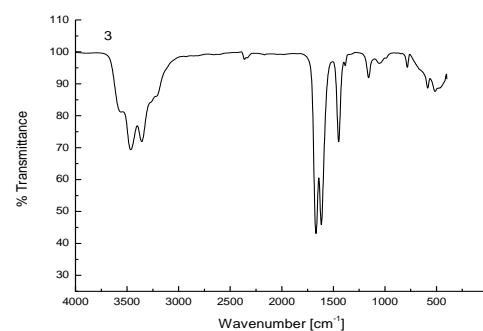
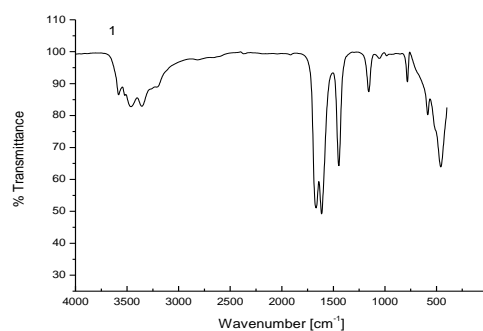


Figure 1a: Infrared spectra of urea complexes  $\text{HgCl}_2 \cdot 4\text{U} \cdot 2\text{H}_2\text{O}$  (1),  $\text{Ni}(\text{NO}_3)_2 \cdot 2\text{U} \cdot 2\text{H}_2\text{O}$  (2),  $\text{HgCl}_2 \cdot 2\text{U} \cdot 2\text{H}_2\text{O}$  (3) and  $\text{Ni}(\text{NO}_3)_2 \cdot 2\text{U} \cdot \text{H}_2\text{O}$  (4).

increase of the CN stretching frequency with a simultaneous decrease in the CO stretching frequency.<sup>47,48</sup> The IR-active  $\nu(\text{M}-\text{O})$  vibration of all prepared urea complexes is observed at the range (637- 479)  $\text{cm}^{-1}$ .<sup>47,48</sup> The band related to the stretching vibration  $\nu(\text{O}-\text{H})$  of non-coordinated  $\text{H}_2\text{O}$  is observed as expected in the range of (3454-3460)  $\text{cm}^{-1}$ , while the corresponding bending motion of the non-coordinated water,  $\delta(\text{H}_2\text{O})$ , is observed in the range of (1613-1628)  $\text{cm}^{-1}$ .

**Table 4:** The maximum temperature,  $T_{\max}/^{\circ}\text{C}$ , and weight loss values of the decomposition stages for the  $\text{HgCl}_2 \cdot 4\text{U} \cdot 2\text{H}_2\text{O}$  (1),  $\text{Ni}(\text{NO}_3)_2 \cdot 2\text{U} \cdot 2\text{H}_2\text{O}$  (2),  $\text{HgCl}_2 \cdot 2\text{U} \cdot 2\text{H}_2\text{O}$  (3) and  $\text{Ni}(\text{NO}_3)_2 \cdot 2\text{U} \cdot \text{H}_2\text{O}$  (4) complexes.

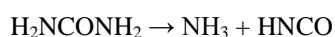
Complexes	Decomposition	$T_{\max}/^{\circ}\text{C}$	Lost		% Weight loss	
			Species	Found	Calc.	
2	Second step	537	Hg + Cl <sub>2</sub>	51.190	49.605	
	First step	204	2H <sub>2</sub> O	10.905	10.624	
	Second step	332	NH <sub>3</sub> +Urea+N <sub>2</sub> O <sub>6</sub>	59.134	41.656	
	Third step	501	NHCO	11.866	12.699	
	Residue		Ni	18.095	17.320	
3	First step	248	2Urea + 2H <sub>2</sub> O + Cl <sub>2</sub>	54.917	53.099	
	Second step	537	Hg	43.750	46.922	
4	First step	108	H <sub>2</sub> O	7.995	5.610	
	Second step	253	2 Urea+2NO <sub>2</sub> + $\frac{1}{2}$ O <sub>2</sub>	72.072	71.061	
	Third step	440	0.5O <sub>2</sub>	3.276	4.986	
	Residue		Ni	16.657	18.292	

In both the nickel complexes, the characteristic stretching vibrations of the nitrate group,  $\text{NO}_3^-$ , is observed at around (1385 and 1156  $\text{cm}^{-1}$  attributed to  $\nu_{\text{as}}(\text{NO}_3)$  and  $\nu_{\text{s}}(\text{NO}_3)$ , respectively.<sup>49</sup> The stretching motion of ( $\nu(\text{N}=\text{O})$ ) is observed at 1477  $\text{cm}^{-1}$  as a strong band, while the bending motion of the type  $\delta(\text{NO}_3)$  are well resolved and observed at around 784  $\text{cm}^{-1}$  as a medium band.

### Thermal analysis

Urea complexes;  $\text{HgCl}_2 \cdot 4\text{U} \cdot 2\text{H}_2\text{O}$  (1),  $\text{Ni}(\text{NO}_3)_2 \cdot 2\text{U} \cdot 2\text{H}_2\text{O}$  (2),  $\text{HgCl}_2 \cdot 2\text{U} \cdot 2\text{H}_2\text{O}$  (3) and  $\text{Ni}(\text{NO}_3)_2 \cdot 2\text{U} \cdot \text{H}_2\text{O}$  (4) were studied by thermogravimetric analysis from ambient temperature to 800 °C in oxygen atmosphere. The TG curves and decomposition stages obtained for these complexes with a temperature rate of 30 °C/min are given in the Supplementary material.

Thermal analysis of  $\text{HgCl}_2 \cdot 4\text{U} \cdot 2\text{H}_2\text{O}$  (1) complex (Supplementary material) shows that the mercury(II) complex prepared at room temperature is thermally stable up to 140°C. Its thermal decomposition occurs in two stages of maximum temperatures  $\text{DTG}_{\max}=273$ , and 537 °C, respectively. From the TG-DTG curves (Supplementary material) it is clear that the first decomposition stage corresponds to the loss of 2 mol of water and 4 mol of urea. The continued loss decomposition in the second step corresponds release of Cl<sub>2</sub> and sublimation of mercury or  $\text{HgCl}_2$  in itself. The probable thermal decomposition of urea released from the complex may be represented as:



The mechanism of the thermal decomposition of the complex is proposed as:

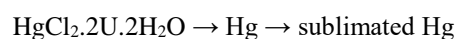


The TG curve of  $\text{Ni}(\text{NO}_3)_2 \cdot 2\text{U} \cdot 2\text{H}_2\text{O}$  (2) complex can be shown in the Supplementary material. Three stages of the dissociation of the complex are indicated in TG and

DTG curve. The first decomposition starts at 178 °C and ends at 261 °C, with an experimental mass loss of 10.905% against a theoretical loss of 10.624%, this corresponds to the release of 2 molecules of water. The second stage takes place between 261 and 405 °C, with an experimental mass loss of 59.134 % against a theoretical loss of 59.138 %, which corresponds to the release of 1 mol of ammonia, 1mol of urea and N<sub>2</sub>O<sub>4</sub>. The last third stage is from 405 to 561 °C with maximum peak at 501 °C, with an experimental mass loss of 11.866 % against a theoretical mass loss of 12.699 %, corresponds to the dissociation of coordinated NHCO leaving Ni as a residue. The mechanism of the thermal decomposition of the complex is proposed as:



The TG curve of  $\text{HgCl}_2 \cdot 2\text{U} \cdot 2\text{H}_2\text{O}$  (3) complex can be seen in the Supplementary material. The TG-DTG curve indicates that the dissociation of complex is in two stages. The first transition takes place between 137 and 287 °C, with  $\text{DTG}_{\max}=248$  °C, corresponds to the release of 2 mol of urea, 2 mol of H<sub>2</sub>O and Cl<sub>2</sub>. The second transformation is from 287 to 453 °C, is due to the sublimation of mercury. The mechanism of the thermal decomposition of the complex is proposed as:



The TG-DTG curve of  $\text{Ni}(\text{NO}_3)_2 \cdot 2\text{U} \cdot \text{H}_2\text{O}$  (4) complex is also shown in the Supplementary material. Three transition stages of are observed in the TG-DTG curve. The first transition stage is from 46 °C to 205 °C with  $\text{DTG}_{\max}=108$  °C, with an experimental mass loss of 7.996% against a theoretical loss of 5.610%, corresponding to the release of 1 mol of water. The second transition stage starts at 205 °C and ends at 329 °C, with  $\text{DTG}_{\max}$  at 253 °C with an experimental mass loss of 72.072% against a theoretical mass loss of 71.061%, due to the release of 2 mol of urea, 2NO<sub>2</sub> and 0.5 O<sub>2</sub>. The last and final transition stage which takes place between 358 °C and 509 °C is due to the loss of 0.5O<sub>2</sub> leaving Ni as a residue, the experimental and theoretical mass losses of this stage were 3.276% and 4.986% respectively. The

sequential thermal dissociation process of the complex can be shown as follows:



To clarify the final decomposition products of urea complexes, the solid residues after thermal degradation under oxygen atmosphere were collected at 800 °C and were analyzed by infrared spectroscopy, X-ray diffractometry, EDX and SEM.

### X- ray powder diffraction studies

The x-ray powder diffraction patterns for the Hg(II) and Ni(II) urea at different temperatures with formulas;  $\text{HgCl}_2 \cdot 4\text{U} \cdot 2\text{H}_2\text{O}$  (1),  $\text{Ni}(\text{NO}_3)_2 \cdot 2\text{U} \cdot 2\text{H}_2\text{O}$  (2),  $\text{HgCl}_2 \cdot 2\text{U} \cdot 2\text{H}_2\text{O}$  (3) and  $\text{Ni}(\text{NO}_3)_2 \cdot 2\text{U} \cdot \text{H}_2\text{O}$  (4) are depicted in Fig. 3. Inspecting these patterns, we notice that all the systems are well crystalline in nature. The crystal size of these complexes could be estimated from XRD patterns by applying FWHM of the characteristic peaks using Deby-Scherrer equation  $1^{50}$ . Where D is the particle size of the crystal gain, K is a constant (0.94 for Cu grid),  $\lambda$  is the x-ray wavelength (1.5406 Å),  $\theta$  is the Bragg diffraction angle and  $\beta$  is the integral peak width. The particle size was estimated according to the highest value of intensity compared with the other peaks. These data gave an impression that the particle size located within nano scale range.

$$D = K \frac{\lambda}{\beta \cos \theta} \quad (1)$$

### SEM and EDX studies

Scanning electron microscopy is a simplest tool used to give an impression about the microscopic aspects of the physical behavior of urea as a chelating agent (Fig. 3). Although this tool is not a qualified method to confirm complex formation but it can be a reference to the presence of a single component in the synthetic complexes.

The pictures of the Hg(II) and Ni(II) complexes show a small particle size with a nano feature products. The chemical analysis results by EDX for the formed complexes show a homogenous distribution between metal ions and chelating agent. SEM examinations were checked the morphology of the surfaces of these complexes that show small particles which have a tendency to agglomerates formation with different shapes comparison with the start materials. The peaks of EDX profile of these complexes (Fig. 5) refer to all elements which constitute the molecules of urea complexes (1-4) that clearly identified confirming the proposed structures.

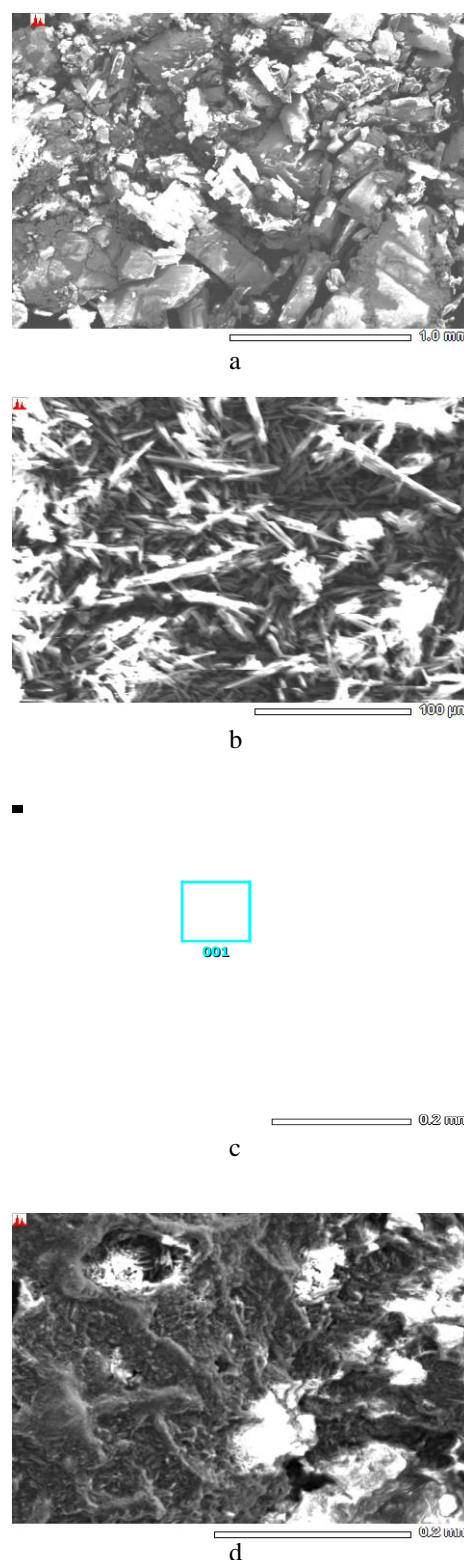


Figure 4: SEM image of:  $\text{HgCl}_2 \cdot 4\text{U} \cdot 2\text{H}_2\text{O}$  (1),  $\text{Ni}(\text{NO}_3)_2 \cdot 2\text{U} \cdot 2\text{H}_2\text{O}$  (2),  $\text{HgCl}_2 \cdot 2\text{U} \cdot 2\text{H}_2\text{O}$  (3) and  $\text{Ni}(\text{NO}_3)_2 \cdot 2\text{U} \cdot \text{H}_2\text{O}$  (4) complexes

**Table 5:** Inhibition zone diameter (mm) of the target compounds against tested microorganisms for HgCl<sub>2</sub>.4U.2H<sub>2</sub>O (1) and Ni(NO<sub>3</sub>)<sub>2</sub>.2U.2H<sub>2</sub>O (2) complexes

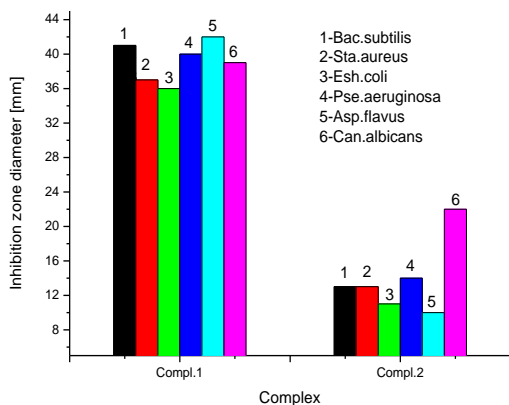
Sample	Inhibition zone diameter (mm / mg sample)						
	<i>Bacillus subtilis</i> (G <sup>+</sup> )	<i>Escherichia coli</i> (G <sup>-</sup> )	<i>Pseudomonas aeruginosa</i> (G <sup>-</sup> )	<i>Staphylococcus aureus</i> (G <sup>+</sup> )	<i>Aspergillus flavus</i> (Fungus)	<i>Candida albicans</i> (Fungus)	
Control: DMSO	0.0	0.0	0.0	0.0	0.0	0.0	
Standard	Antibacterial agent (Tetracycline)	36	31	35	30	--	--
	Antifungal agent Amphotericin B	--	--	--	--	18	19
<b>1</b>	41	36	40	37	42	39	
<b>2</b>	13	11	14	13	10	22	

G: Gram reaction.

Solvent: DMSO.

### 3-8- Biological evaluation

Biological evaluations were checked in terms of antimicrobial activities of target compounds against gram-positive (*Bacillus subtilis* and *Staphylococcus aureus*) and gram-negative (*Escherichia coli* and *Pseudomonas aeruginosa*) and two strains of fungi (*Aspergillus flavus* and *Candida albicans*). Result from the agar disc diffusion tests for antimicrobial activities of target compounds are presented in Table 5, and illustrated in Fig. 4.

Figure 4 : Biological evaluation of HgCl<sub>2</sub>.4U.2H<sub>2</sub>O (1) and Ni(NO<sub>3</sub>)<sub>2</sub>.2U.2H<sub>2</sub>O(2) complexes

The diameters of zone of inhibition (in mm) of the standard drug tetracycline against gram positive bacteria *B. subtilis* and *S. aureus* and gram negative bacteria *E. coli* and *P. aeruginosa* were found to be 36, 30, 31 and 35 mm, respectively, while the standard drug amphotericin B against *Aspergillus flavus* and *Candida albicans* gave 18 and 19, respectively. Under identical conditions, Table 5 shows that, complex 1 has (41, 36, 40, 37, 42 and 39 mm) while complex 2 has (13, 11, 14, 13, 10 and 22 mm)

respectively, for *Bacillus subtilis*, *Escherichia coli*, *Pseudomonas aeruginosa*, *Staphylococcus aureus*, *Aspergillus flavus* and *Candida albicans*. Both the complexes were found to be an efficient microbial agents.

### References

- Wöhler, F., *Ann. Phys.*, **1828**, 12, 253.
- Tonn, W. H. Jr., *Chem. Eng.*, **1955**, 62, 186.
- Moore, P., *Chem. & Eng. News*, **1959**, 37, 84.
- Franz, A., *J. Org. Chem.*, **1961**, 26, 3304.
- Feldman, D. Barbalata, A., "Synthetic Polymers", Chapman & Hall, London, **1996**.
- Finar, I. L., *Organic Chemistry*, Longman Group Ltd., London, **1973**, p. 460.
- Rahman, M. J. and P. Bozadjiev, Y. Polovski, *Fert. Res.*, **1994**, 38(2), 89.
- George, S. Chellapandian, M. Sivasankar, B. Jayaraman, K., *Bioprocess Eng.*, **1997**, 16(2), 83.
- Wang, X. J. Douglas, L.A., *Agrochimica*, **1996**, 40(5-6), 209.
- Yerokun, O. A., *S. Afr. J. Plant Soil*, **1997**, 14(2), 63.
- Heinig, R., *SOFW J.*, **1996**, 122(14), 998.
- Gnewuch, C. T. Sosnovsky, G., *Chem. Rev.*, **1997**, 97(3), 829.
- Miyagawa, C. I., *Drug Intell. & Clin. Pharma.*, **1986**, 20, 527.
- Kissa, E., *Text. Res. J.*, **1969**, 39(8), 734.
- Srinivasa, I. Vishivanathapuram, K. Mishra, M. B. Ghosh, S. K., *Technology*, **1970**, 7(12), 27.
- Kaganskii, I. M. Babenko, A. M., *Zh. Prikl. Khim.*, **1970**, 43(11), 2390.
- Zhang, Y. Bai, J. Wei, T. Lu, A., *Huaxue Shijie*, **1996**, 37(4), 178.
- Kim, Y. K., Williard, J. W., Frazier, A. W., *J. Chem. Eng. Data*, **1988**, 33(3), 306.
- Gentile, P. S. Carfagno, P. Haddad, S. Campisi, L., *Inorg. Chim. Acta*, **1972**, 6C, 296.
- Sagatys, D. S. Bott, R. C. Smith, G. Byriel, K. A. Kennard, C. H. L., *Polyhedron*, **1992**, 11(1), 49.
- Lewinski, K. Sliwinski, J. Lebioda, L., *Inorg. Chem.*, **1983**, 22(16), 2339.
- Kryatov, V. Nazarenko, A. Y. Robinson, P. D. Rybak-Akimova, E. V. *Chem. Comm.*, **2000**, 11, 921.

- <sup>23</sup> Bhoopathy, T. J. Baskaran, M. Mohan, S. *Indian J. Phys.*, **1988**, 62B(1), 47.
- <sup>24</sup> Yamaguchi, A. Penland, R. B. Mizushima, S. Lane, T. J., Curran, C., Quagliano, J. V., *J. Am. Chem. Soc.*, **1958**, 80, 527.
- <sup>25</sup> Duncan, J. L., *Spectrochim. Acta*, **1970**, 27A, 1197.
- <sup>26</sup> Aitken, G. B. Duncan, J. L. Mc Quillan, G. P. *J. Chem. Soc. A*, **1971**, 2695.
- <sup>27</sup> Hadzi, D. Kidric, J. Knezevic, Z. V. Barlic, B. *Spectrochim. Acta*, **1976**, 32A, 693.
- <sup>28</sup> Bala, S. S., Ghosh, P. N., *J. Mol. Struct.*, **1983**, 101, 69.
- <sup>29</sup> Kellner, L. *Proc. Roy. Soc.*, **1941**, 177A, 456.
- <sup>30</sup> Waldron, R. D. Badger, R. M., *J. Chem. Phys.*, **1950**, 18, 566.
- <sup>31</sup> Andrew, E. R. Hyndman, D., *Proc. Phys. Soc.*, **1953**, 66A, 1187.
- <sup>32</sup> Yamaguchi, A. Miyazawa, T. Shimanouchi, T. Mizushima, S., *Spectrochim. Acta*, **1957**, 10, 170.
- <sup>33</sup> Stewart, J. E., *J. Chem. Phys.*, **1957**, 26, 248.
- <sup>34</sup> Penland, R. B. Mizushima, S. Curran, C. Quagliano, J. V., *J. Am. Chem. Soc.*, **1957**, 79, 1575.
- <sup>35</sup> G. F. Svatos, C. Curran, J. V. Quagliano, *J. Am. Chem. Soc.*, **1955**, 77, 6159.
- <sup>36</sup> Boron W. F. and Boulpaep, E. L. *Medical Physiology*, Updated Edition, Saunders, Philadelphia, Pa, USA, **2004**.
- <sup>37</sup> Meessen J. H. and Petersen, H., „Urea,“ in *Ullmann's Encyclopedia of Industrial Chemistry*, Electronic Release, Wiley-VCH, Weinheim, Germany, 6th edition, **2002**.
- <sup>38</sup> Bauer, A.W. Kirby, W. M. Sherris, C. Turck, M., *Am. J. Clin. Pathol.*, **1966**, 45, 493.
- <sup>39</sup> Pfaller, M. A. Burmeister, L. Bartlett, M. A. Rinaldi, M. G., *J. Clin. Microbiol.*, **1988**, 26, 1437.
- <sup>40</sup> National Committee for Clinical Laboratory Standards, Performance vol. antimicrobial susceptibility of Flavobacteria, **1997**.
- <sup>41</sup> *Methods for dilution antimicrobial susceptibility tests for bacteria that grow aerobically*. National Committee for Clinical Laboratory Standards. *Approved standard M7-A3*, **1993**.
- <sup>42</sup> *Reference Method for Broth Dilution Antifungal Susceptibility Testing of Conidium-Forming Filamentous Fungi: Proposed Standard M38-A*. NCCLS, Wayne, PA, USA., National Committee for Clinical Laboratory Standards. **2002**.
- <sup>43</sup> *Methods for Antifungal Disk Diffusion Susceptibility Testing of Yeast: Proposed Guideline M44-P*. NCCLS, Wayne, PA, USA. National Committee for Clinical Laboratory Standards. **2003**.
- <sup>44</sup> Liebowitz, L.D. Ashbee, H.R. Evans, E.G.V. Chong, Y. Mallatova, N. Zaidi, M. Gibbs, D. and Global Antifungal Surveillance Group, *Diagn. Microbiol. Infect. Dis.*, **2001**, 4, 27.
- <sup>45</sup> Matar, M. J. Ostrosky-Zeichner, L. Paetznick, V. L. Rodriguez, J. R. Chen, E. Rex, J. H. *Antimicrob. Agents Chemother.*, **2003**, 47, 1647.
- <sup>46</sup> Earnshaw, A. *Introduction to Magnetochemistry*, Academic press, London and New York, **1968**, p. 35.
- <sup>47</sup> Diamantopoulou, E. Papaefstatiou, G.S. Terzis, A. Raptopoulou, C.P. Dessey, H.O. Perlepes, S. P. *Polyhedron*, **2003**, 22, 825.
- <sup>48</sup> Keuleers, R., Papaefstathiou, G. S., Raptopoulou, C. P., Perlepes, S. P., Dessey, H. O., *J. Mol. Struct.*, **2000**, 525(1-3), 173.
- <sup>49</sup> Nakamoto, K., *Infrared and Raman Spectra of Inorganic and Coordination Compounds*, Wiley, New York, **1978**.
- <sup>50</sup> Quan, C. X. Bin, L. H. Bang, G. G., *Mater. Chem. Phys.* **2005**, 91, 317.

Received: 18.09.2012.

Accepted: 30.09.2012.



# SYNTHESIS, SPECTRAL, THERMAL, MAGNETIC, AND STRUCTURAL STUDY OF DIAQUABIS-(*m*-HYDROXYBENZOATO-κO)BIS(N,N-DIETHYLNICOTINAMIDE-κN)COBALT(II)

Dursun Ali Köse<sup>[a]</sup>, Onur Sahin<sup>[b]</sup> and Orhan Büyükgüngör<sup>[b]</sup>

**Keywords:** mixed ligand complexes, Co(II) complex, N,N-diethylnicotinamide, *m*-hydroxybenzoate, thermal decomposition, X-ray structure, mass pattern

The complex of [Co(*m*-hba)<sub>2</sub>(Dena)<sub>2</sub>(H<sub>2</sub>O)<sub>2</sub>], diaquabis(*m*-hydroxybenzoato-κO)bis(N,N-diethylnicotinamide-κN)Cobalt(II), C<sub>34</sub>H<sub>42</sub>CoN<sub>4</sub>O<sub>10</sub>, referred to in the title, has been synthesized and explained as structural by using elemental analysis, FT-IR spectra, UV-Vis reflectance, magnetic measurements, thermal analysis, mass spectra and X-ray diffraction methods. The analysis results showed that the unit cell of the complex includes one molecule of Co<sup>II</sup>-cation, two molecules of *m*-hydroxybenzoate, two molecules of N,N-diethylnicotinamide ligands and two molecules of aqua ligands. The compound crystallizes in the triclinic space group P-1 with the following unit-cell parameters: **a**=8.7288(3)Å, **b**=14.2213(4)Å, **c**=15.4307(5), α=108.270(2)°, β=92.473(3)°, γ=102.549(5)° and Z=2. The compound crystallizes in the space group P-1 with Z'=1. The asymmetric unit of the complex C<sub>34</sub>H<sub>42</sub>CoN<sub>4</sub>O<sub>10</sub> contains two crystallographically independent molecules. Each Co<sup>II</sup> ion located at a centre of symmetry and is coordinated by two O atoms from two equivalent carboxylate groups, two O atoms from aqua ligands, and two pyridyl N atoms. It has strong paramagnetic properties.

\* Corresponding Authors

Tel: +90 3642700000/1635; Fax: +903642700005

E-Mail: dalikose@hitit.edu.tr

[a] Department of Chemistry, Hitit University, 19030 Çorum, Turkey

[b] Department of Physics, Ondokuz Mayıs University, 55139 Samsun, Kurupelit, Turkey

The scope of this study, Co<sup>II</sup> with *m*-hydroxybenzoato-diethylnicotinamide complex has been synthesized and the

structural properties of compound were explained by using X-ray diffraction studies, FT-IR spectra, UV-VIS spectra, elemental analysis, magnetic measurements, mass spectra and TGA/DTA curves. The decomposition pathways of the investigated complex are discussed in connection with the available spectroscopic data.

## Introduction

Studies on mixed-ligand complexes have importance with special interest on complexes between transition metal ions, benzoate ion and a nitrogen base. Various studies on mixed-ligand metal complexes of the benzoate and N,N-diethylnicotinamide have been reported.<sup>1-11</sup>

In the recent times, research in bioinorganic chemistry has revealed the important role of metal ions in most biological processes. Carboxylates play an important role in inorganic chemistry, and lots of metal cations in a great number of various biological processes, especially six-membered ring systems, are still components of several vitamins and drugs.<sup>12</sup> Also, some carboxylate compounds (e.g. benzoates) are known to have antibacterial activity. Benzoic acid is used in combination with salicylic acid in dermatology as a fungicidal treatment for fungal skin diseases.<sup>13, 14</sup> Metal complexes of biologically important ligands are sometimes more effective than free ligands.<sup>15</sup> It is well documented that heterocyclic compounds play a significant role in many biological systems. Therefore, it is not surprising that many authors have investigated heterocyclic compounds and also examined them as ligands in coordination compounds of several central atoms.<sup>16-22</sup>

## Experimental

### Materials and Instrumentation

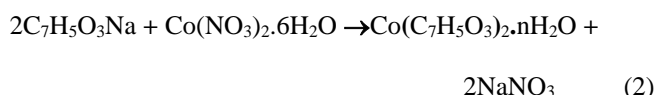
All chemicals used were analytic reagent products. Co(NO<sub>3</sub>)<sub>2</sub>·6H<sub>2</sub>O, *m*-hydroxybenzoic acid (*m*-hba), and N,N-diethylnicotinamide (dena) (Scheme 1) were obtained from Sigma Aldrich. Elemental analyses (C, H, N) were carried out by standard methods (Tubitak Marmara Research Center). Magnetic susceptibility measurements were performed at room temperature by using a Sherwood Scientific MXI model Gouy magnetic balance and Quantum Designed Physical Property Measurement System (PPMS). Infrared spectra were recorded in the 4000–400 cm<sup>-1</sup> region with a Perkin Elmer Spectrum One FT-IR spectrophotometer by using KBr pellets. Thermal analyses (TGA, DTA) were performed by the Shimadzu DTG-60H system, in dynamic nitrogen atmosphere (100mL/min) at a heating rate of 10°C/min, in platinum crucibles as sample vessel, by using α-Al<sub>2</sub>O<sub>3</sub> as reference. Electronic spectra were recorded by a Shimadzu 3600/UV-VIS-NIR Spectrophotometer. Mass spectrum data were recorded by an Agilent Technologies 5973 spectrophotometer by using DIP-MS method.

### Preparation of the Co(II)-*m*-hydroxybenzoato-*N,N*-diethylnicotinamide (1) complex

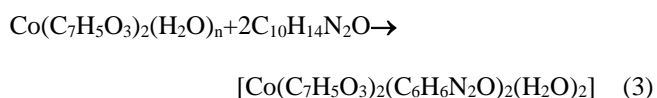
In the first step, *m*-hydroxybenzoic acid sodium salt was prepared at room temperature according to the equation (1) below. All of the reactions were carried out in water/ethanol (50%/50%) media. When removal of CO<sub>2</sub> gas is finished, the reaction is completed.



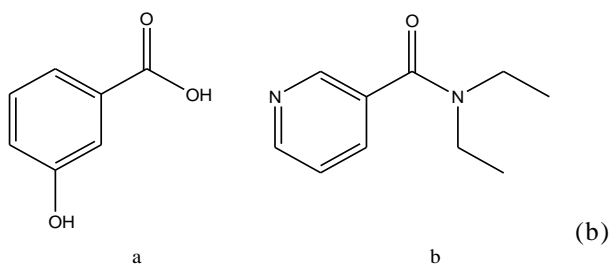
In the second step, the cobalt(II) *m*-hydroxybenzoate was synthesized from Na(*m*-hba) salt by the following substitution reaction:



Finally, the solution of *N,N*-diethylnicotinamide (2 mmol) in distilled water (30 mL) was added dropwise to a stirred solution of Co(*m*-hba)<sub>2</sub>(H<sub>2</sub>O)<sub>*n*</sub> (1 mmol) in hot distilled water/ethanol (50/50 mL). The resulting solution was left for 15–17 days for crystallization at room temperature. The crystals formed were filtered off and washed with cold water and acetone, then dried in vacuum. The mixed ligand complexes were prepared according to the following equations:



The yield of the compound (1) is about 76%. Calculated for C<sub>34</sub>H<sub>42</sub>CoN<sub>4</sub>O<sub>10</sub>: C 52.63; H 4.10; N 8.19. Found: C 52.12; H 4.38, N 8.27.



**Scheme 1.** Molecular structure of the ligands, (a) *m*-hydroxybenzoic acid (*m*-hba), (b) *N,N*-diethylnicotinamide(Dena).

### Results and Discussion

The effective magnetic moment of Co<sup>II</sup> ion is 4.21 BM and is compatible with literature values for similar complexes.<sup>9,10,21</sup> According to analytical results, the per mole formula unit of complex contain 2 moles of *m*-hydroxybenzoato/diethylnicotinamide ligands and two moles of water. The octahedral coordination of the metal ion has been completed by two carboxylic oxygen atoms from two *m*-hydroxybenzoates, two nitrogen atoms from

two diethylnicotinamides, and two aqua oxygen atoms. According to the magnetic susceptibility results, the complex (1) is paramagnetic.

The electronic spectrum of the complex was taken in the solid state because of the low solubility of the complex. The electronic spectra showed two d–d transitions at 7045 cm<sup>-1</sup> (<sup>4</sup>T<sub>1g</sub>→<sup>4</sup>T<sub>2g</sub>) and 20105 cm<sup>-1</sup> (<sup>4</sup>T<sub>1g</sub>→<sup>4</sup>T<sub>1g</sub>) (<sup>4</sup>P) for the compound. The UV–visible peaks corresponding to the π→π\* transitions in the ligands were observed at 272 and 327 nm.<sup>23</sup> The coordination geometry of Co<sup>II</sup> ion is that of an octahedral with the N atoms from diethylnicotinamide ligands, the bonded carboxylate O atoms from *m*-hydroxybenzoato ligands, and two O atoms from aqua ligands.

### FT-IR spectra

Absorption bands in the range of 3450–2900 cm<sup>-1</sup> correspond to the asymmetric and symmetric stretching vibrations of water molecules. The *m*-hba/Dena mixed ligand complexes give rise to strong bands responsible from the C=O stretching. Conjugation between the carbonyl group and the amide nitrogen causes small frequency shifts. The strong bands observed at around 1677 cm<sup>-1</sup> are assigned to this mode. This band remained almost in the same range as the amide group of the free Dena ligand, indicating that the Dena ligand does not coordinate through amide group. Pyridine ring vibration of free diethylnicotinamide at 1565 cm<sup>-1</sup> shifts to 1455 cm<sup>-1</sup> in the complexes indicating that the pyridine ring is coordinated. The main difference in the spectrum of *m*-hydroxybenzoic acid is that the C=O stretching vibration of the carboxyl group at 1718 cm<sup>-1</sup> shifts to lower frequencies in the cobalt complex (1). The carboxylate peak in the complex (1) appears in the range of 1677 cm<sup>-1</sup>. This shows that the coordination takes place through the carboxyl group.<sup>24</sup> The –OH bending peak for the *m*-hydroxybenzoic acid remained almost in the same position at around 1259 cm<sup>-1</sup> in the complex (1). The low intensity bands in the region of 600–400 cm<sup>-1</sup> are attributed to M–N and M–O vibrations.<sup>9,20–22</sup>

### Thermal Analysis



Fig. 1 shows the TG–DTG/DTA curves for the Co(II) complex (1). According to these curves, two molecules of the coordinated aqua ligands have released an accompanying endothermic effect with the DTA curve at 127 °C (exp. 5.08 %; calc. 4.96 %). The anhydrous complex begins to decompose with melting at 153 °C. Two moles of neutral diethylnicotinamide ligands are decomposed with removal of four moles of ethyl groups. (exp. 15.98 %; calc. 16.39 %). Then two moles of amide groups of diethylnicotinamide ligands are released from the structure with endothermic effect (exp. 12.24 %; calc. 11.97 %). Afterwards, two moles pyridine groups are decomposed and removed at 348 °C DTA peak as an endothermic (exp. 21.56 %; calc. 21.50 %) peak. After decomposing of neutral ligands at 349 °C, the *m*-hydroxybenzoato ligands begin to degrade in two steps by giving endothermic peaks. Finally, cobalt oxide (CoO) remains in the crucible (exp. 10.89 %; calc. 10.33 %).

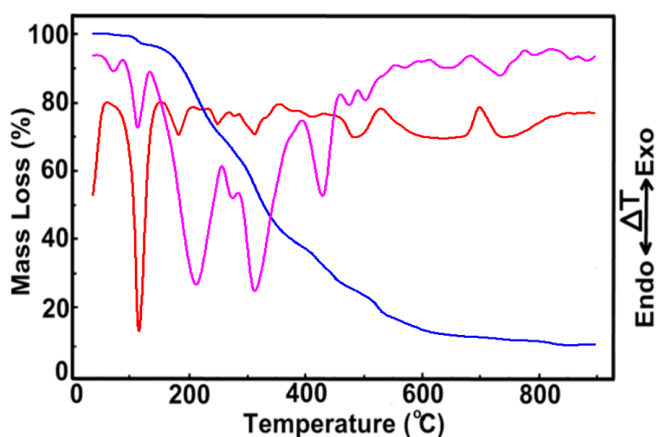


Figure 1. The TG-DrTGA/DTA curves of the Co(II) complex.

### Mass Spectra

The thermal decomposition pathway of the [Co(*m*-hba)<sub>2</sub>(Dena)<sub>2</sub>(H<sub>2</sub>O)<sub>2</sub>] complex mass spectrum was recorded (Fig. 2) by using direct insertion probe pyrolysis mass spectrometry method. The molecular ion peak is detected at 723 *m/z* in the mass spectrum recorded. The mass spectrum obtained is relatively complex. Beside the most abundant peaks, much fewer abundant peaks were observed on the spectrum depending probably on the nature of ligands. Scheme 2 summarizes the fragmentation pattern of the complex (1). The mass spectra data support to thermal decomposition.

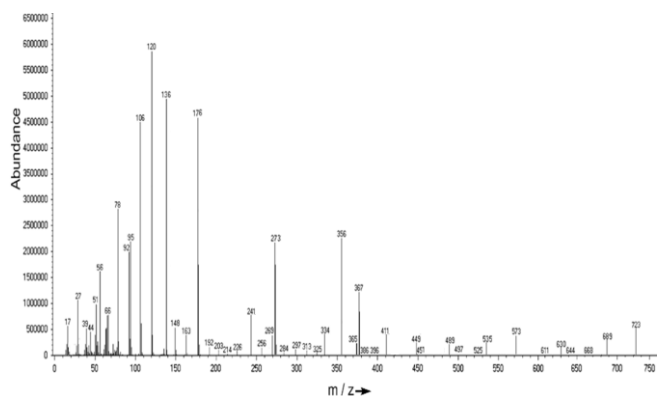


Figure 2. Mass spectrum of the [Co(*m*-hba)<sub>2</sub>(dena)<sub>2</sub>(H<sub>2</sub>O)<sub>2</sub>] complex

### Data collection, structure solution, and refinement

Suitable crystals of C<sub>34</sub>H<sub>42</sub>CoN<sub>4</sub>O<sub>10</sub> were selected for data collection which was performed on a STOE IPDS II diffractometer equipped with a graphite-monochromatic Mo-K $\alpha$  radiation ( $\lambda = 0.71073 \text{ \AA}$ ) at 296 K. Other details of cell data, data collection, and refinement are summarized in Table 1. The structures were solved by direct methods using SHELXS-97 and refined by full-matrix least-squares methods on F<sup>2</sup> using SHELXL-97<sup>25</sup> from within the WINGX<sup>26</sup> suite of software. All non-hydrogen atoms were refined with anisotropic parameters.

The molecular structure of C<sub>34</sub>H<sub>42</sub>CoN<sub>4</sub>O<sub>10</sub> (1) and the atom-labelling scheme are shown in Fig. 3. The compound C<sub>34</sub>H<sub>42</sub>CoN<sub>4</sub>O<sub>10</sub> crystallizes in the space group P-1 with Z'=1.

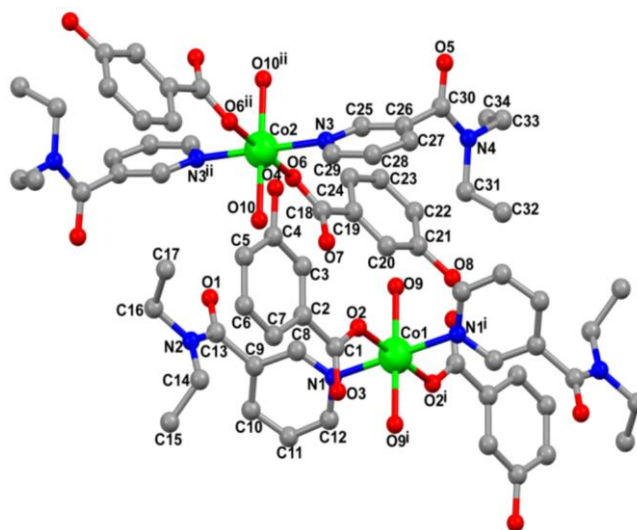


Figure 3. A view of a [Co(*m*-hba)<sub>2</sub>(Dena)<sub>2</sub>H<sub>2</sub>O)<sub>2</sub>] molecule showing the atom-numbering scheme. Displacement ellipsoids are drawn at 30% probability level. [Symmetry codes: (i) 1-*x*, 1-*y*, 1-*z*; (ii) 1-*x*, 2-*y*, 1-*z*.]

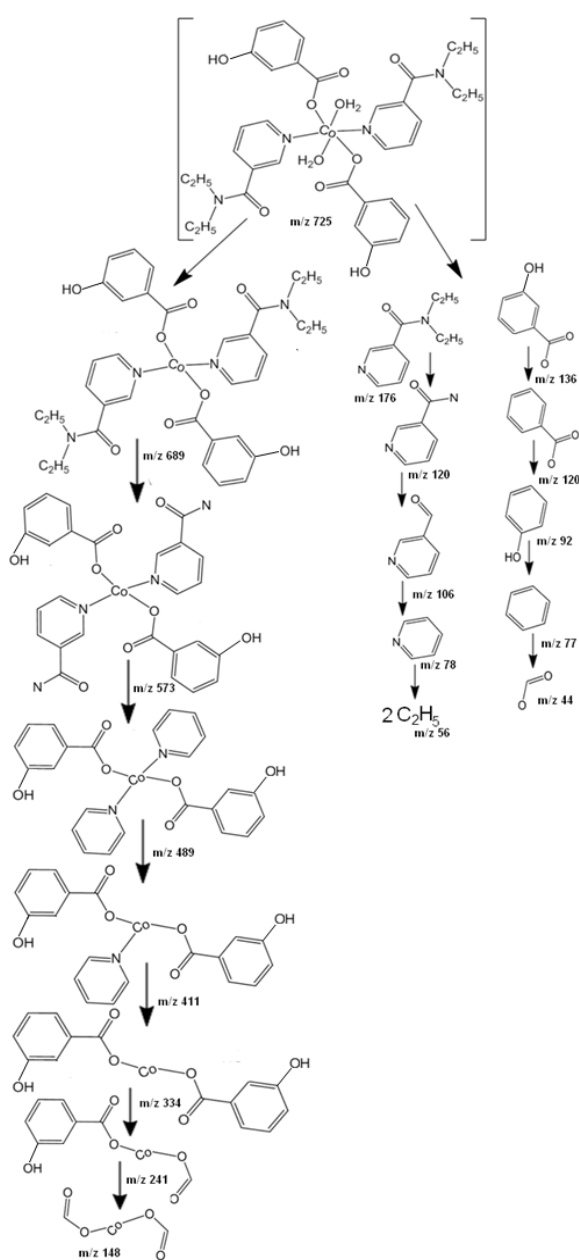
Table 1 Experimental details of the compound [Co(*m*-hba)<sub>2</sub>(Dena)<sub>2</sub>H<sub>2</sub>O)<sub>2</sub>].

Crystal data	[Co( <i>m</i> -hba) <sub>2</sub> (Dena) <sub>2</sub> H <sub>2</sub> O) <sub>2</sub> ]
Chemical formula	C <sub>34</sub> H <sub>42</sub> CoN <sub>4</sub> O <sub>10</sub>
M <sub>r</sub>	725.65
Cell setting, space group	Triclinic, P -1
Temperature (K)	296
a, b, c (Å)	8.7288 (3), 14.2213 (4), 15.4307 (5)
$\alpha$ , $\beta$ , $\gamma$ (°)	108.270 (2), 92.473 (3), 102.549 (3)
V (Å <sup>3</sup> )	1762.64 (10)
Z	2
D <sub>x</sub> (Mg m <sup>-3</sup> )	1.367
$\mu$ (mm <sup>-1</sup> )	0.55
Crystal form, colour	Needle, pink
Crstal size (mm)	0.50 x 0.40 x 0.13
Absorption correction	Integration
T <sub>min</sub>	0.719
T <sub>max</sub>	0.938
No. of measured, independent and observed reflections	43297, 7292, 5526
Criterion for observed reflection	I > 2 $\sigma$ (I)
R <sub>int</sub>	0.051
$\theta_{max}$ (°)	26.5
R[F <sup>2</sup> > 2 $\sigma$ (F <sup>2</sup> )], wR(F <sup>2</sup> ), S	0.044, 0.122, 1.05
No. of reflections	7292
No. of parameters	457
( $\Delta$ / $\sigma$ ) <sub>max</sub>	0.001
$\Delta\rho_{max}$ , $\Delta\rho_{min}$ (e Å <sup>-3</sup> )	0.35, -0.33

**Table 2.** Hydrogen-bond parameters (Å, °) of C<sub>34</sub>H<sub>42</sub>CoN<sub>4</sub>O<sub>10</sub>.

D-H...A	D-H	H...A	D...A	D-H...A	Chain	Motif	Direction
O4-H4...O5 <sup>v</sup>	0.82	1.93	2.685 (3)	152	C (11)	-	[110]
O8-H8A...O3 <sup>vi</sup>	0.82	2.02	2.803 (3)	161	-	R <sub>2</sub> <sup>1</sup> (6)	-
O9-H9A...O3 <sup>vi</sup>	0.79 (4)	1.93(4)	2.707 (3)	166 (4)	-	R <sub>1</sub> <sup>1</sup> (6)	-
O9-H9B...O7	0.82 (4)	1.93(4)	2.744 (3)	177 (4)	-	R <sub>2</sub> <sup>2</sup> (14)	-
O10-H10A...O7	0.76 (4)	1.89(4)	2.641 (3)	169 (4)	-	S(6)	-
O10-H10A...O6	0.76 (4)	2.57(4)	2.938 (3)	111 (4)	-	S(4)	-
O10-H10B...O1	0.82 (4)	1.99(4)	2.775 (4)	159 (4)	C <sub>2</sub> <sup>2</sup> (16)	R <sub>2</sub> <sup>2</sup> (14)	[010]
C20-H20...O3 <sup>vi</sup>	0.93	2.54	3.226 (3)	131	C <sub>2</sub> <sup>2</sup> (18)	R <sub>2</sub> <sup>1</sup> (6)	[010]
C29-H29...O4	0.93	2.47	3.302 (3)	149	C <sub>2</sub> <sup>2</sup> (18)	R <sub>2</sub> <sup>2</sup> (16)	[010]

Cg2 = C1-C6. Symmetry codes: (i) *x*, *y*-1, *z*; (ii) -*x*+2, -*y*+1, -*z*+1; (iii) *x*, -*y*+3/2, *z*+1/2; (iv) 1-*x*, *y*-1/2, 3/2-*z*; (v) -*x*+2, -*y*+2, -*z*+1; (vi) -*x*+1, -*y*+1, -*z*+1.

**Scheme 2.** Mass spectral fragmentation pattern of the [Co(*m*-hba)<sub>2</sub>(Dena)<sub>2</sub>H<sub>2</sub>O]<sub>2</sub>.

Water H atoms were located in difference maps and refined subject to a DFIX restraint of O-H = 0.83(2)Å, and with U<sub>iso</sub>(H) = 1.5U<sub>eq</sub>(O). All other H atoms were located from difference maps and then treated as riding atoms with C-H distances of 0.93-0.97Å and O-H distances of 0.82Å, and with U<sub>iso</sub>(H) = 1.2U<sub>eq</sub>(C, O). Molecular diagrams were created by using ORTEP-III.<sup>27</sup> Geometric calculations were performed with PLATON.<sup>28</sup> The molecules are linked by intramolecular hydrogen bonding, and graph-set notation<sup>29</sup> was employed to describe the patterns of hydrogen bonding. Details of hydrogen-bond dimensions are given in Table 2.

The asymmetric unit of the complex C<sub>34</sub>H<sub>42</sub>CoN<sub>4</sub>O<sub>10</sub> contains two crystallographically independent molecules. Each Co<sup>II</sup> ion is located at a centre of symmetry and is coordinated by two O atoms from two equivalent carboxylate groups, two O atoms from aqua ligands, and two pyridyl N atoms (Table 3).

**Table 3** Selected bond lengths (Å) and angles (°) for the C<sub>34</sub>H<sub>42</sub>CoN<sub>4</sub>O<sub>10</sub>

Co2-O10	2.116(2)	N1-Co1	2.154(2)
O6-Co2	2.0571(19)	O2-Co1	2.0882(16)
N3-Co2	2.176(2)	Co1-O9	2.1037(19)
O2-Co1-O9 <sup>i</sup>	90.08(7)	O2 <sup>i</sup> -Co1-N1	92.75(8)
O2 <sup>i</sup> -Co1-O9 <sup>i</sup>	89.92(7)	O9 <sup>i</sup> -Co1-N1	85.61(8)
O10-Co2-N3	87.32(9)	O9-Co1-N1	94.39(8)
O10-Co2-N3 <sup>ii</sup>	92.68(9)	O6 <sup>ii</sup> -Co2-N3 <sup>ii</sup>	88.59(8)
O2-Co1-N1	87.25(8)	O6 <sup>ii</sup> -Co2-O10	90.51(8)
O6 <sup>ii</sup> -Co2-N3	91.41(8)	O6-Co2-O10	89.49(8)

Symmetry codes: (i) -*x*+1, -*y*+1, -*z*+1; (ii) -*x*+1, -*y*+2, -*z*+1.

The C<sub>34</sub>H<sub>42</sub>CoN<sub>4</sub>O<sub>10</sub> (**1**) molecules are linked into sheets by a combination of seven O-H...O hydrogen bonds and two C-H...O hydrogen bonds (Table 2). Within the selected asymmetric unit, intramolecular O10-H10A...O6 and O10-H10A...O7 hydrogen bonds produce S(4) and S(6) motifs. Atom O4 in the molecule at (*x*, *y*, *z*) acts as hydrogen-bond donor, via atom H4, to atom O5 in the molecule at (-*x*+2, -*y*+2, -*z*+1), so forming a C(11) chain running parallel to the [110] direction (Fig. 4). Atoms C20 and O8 in the molecule at (*x*, *y*, *z*) act as hydrogen-bond donors, via atoms H20 and H8A, to atom O3 in the molecule at (-*x*+1, -*y*+1, -*z*+1), so forming an R<sub>2</sub><sup>1</sup>(6) ring. The combination of O-H...O and C-H...O hydrogen bonds produces R<sub>2</sub><sup>2</sup>(14)R<sub>2</sub><sup>2</sup>(16) rings (Fig. 5).

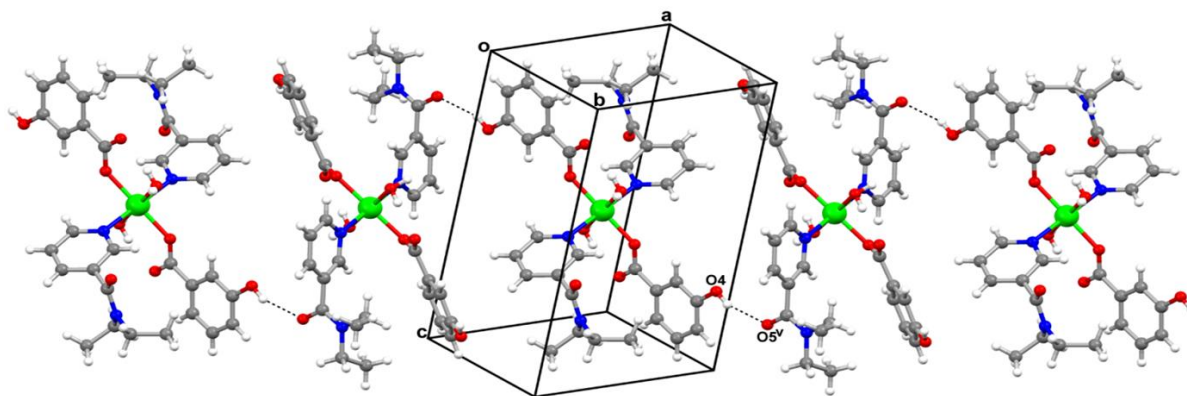


**Figure 4.** Part of the crystal structure of C<sub>34</sub>H<sub>42</sub>CoN<sub>4</sub>O<sub>10</sub>, showing the formation of a chain along [110] generated by O-H...O hydrogen bonds. [Symmetry code: (v)  $-x+2, -y+2, -z+1$ .]

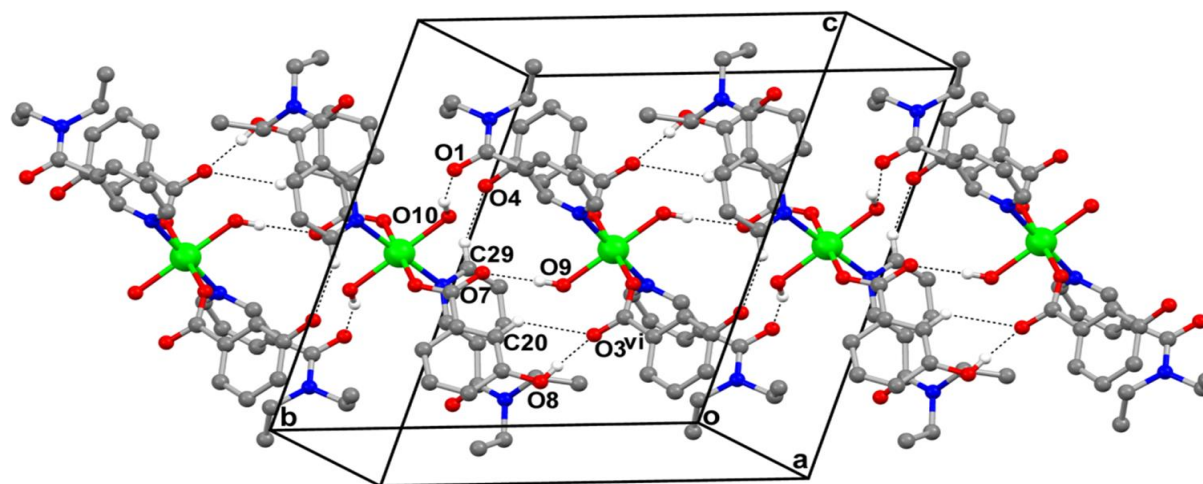


**Figure 5.** Part of the crystal structure of C<sub>34</sub>H<sub>42</sub>CoN<sub>4</sub>O<sub>10</sub>, showing the formation of R<sub>2</sub><sup>2</sup>(14)R<sub>2</sub><sup>2</sup>(16) rings. H atoms not involved in these interactions have been omitted for clarity. [Symmetry code: (vi)  $-x+1, -y+1, -z+1$ .]

### Magnetic Studies

Magnetic properties have been recorded at 300 K on crushed crystalline samples of the complex. The magnetic behavior of the complex is shown in Figure 7. The variable-field magnetization data were collected in the magnetic field (Oe) range -30000 to 30000 G. The  $\chi_M T$  value at 300 K is 3 cm<sup>3</sup>Kmol<sup>-1</sup>. The saturation magnetization, remanent magnetization and coercivity values were calculated 0.2579 emu, 0.00191 emu and -95.149 Oe, respectively from the hysteresis loop of the complex. The magnetization curve of the complex recorded at room temperature is given in Figure 6.

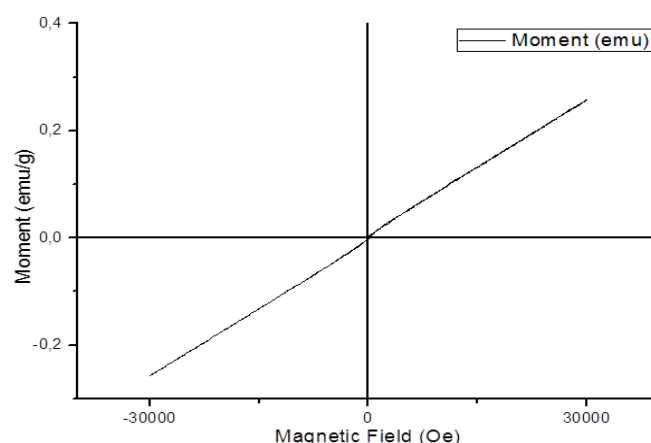


**Figure 6.** The magnetization curve of C<sub>34</sub>H<sub>42</sub>CoN<sub>4</sub>O<sub>10</sub>. (1)

### Conclusion

Thermal decomposition takes place in three steps: dehydration of two moles of aqua ligands, elimination of the two moles of neutral *N,N*-diethylnicotinamide ligands, and decomposition of the two moles of anionic *m*-hydroxybenzoato ligands. In the reaction crucible, the CoO metal oxide remains as a decomposition product. According to thermal analysis data, releasing of the diethylnicotin-

amide and *m*-hydroxybenzoato ligands is an endothermal process and resembles to thermal decomposition of diethylnicotinamide complexes reported by previous investigators.<sup>6,8,9,22,30</sup> An earlier releasing of the diethylnicotinamide than that of *m*-hydroxybenzoato ligand by volatilisation may be due to the non-ionic bonding to metal ion.

In the complex (1), all the ligands are coordinated to the metal ion in monodentate mode. The IR spectra of the intermediate products showed similar results. The (COO)<sup>-</sup><sub>sym</sub> peak is located at 1677 cm<sup>-1</sup> for the complex (1). The (COO)<sup>-</sup><sub>asym</sub> peak is observed at 1444 cm<sup>-1</sup>. The shift ( $\Delta$ ) between  $\mu_{asym}$  and  $\mu_{sym}$  bands of COO<sup>-</sup> group is 233 cm<sup>-1</sup> for the complex which is higher than for the sodium salt of m-hydroxybenzoic acid (163 cm<sup>-1</sup>) in which the monodentate carboxylate group exists.<sup>22,24</sup>Hiba! A könyvjelző nem létezik.

The mass spectra gave the expected fragmentation peaks of the complex.

The asymmetric unit of the complex C<sub>34</sub>H<sub>42</sub>CoN<sub>4</sub>O<sub>10</sub> contains two crystallographically independent molecules. Each Co<sup>II</sup> ion is located at a centre of symmetry and is coordinated by two O atoms from two equivalent carboxylate groups, two O atoms from aqua ligands, and two pyridyl N atoms (Table 3). The geometry around the Co<sup>II</sup> ion is that of a distorted octahedron, the equatorial plane of which (O2, O2<sup>i</sup>, O6, O6<sup>ii</sup>, O9, O9<sup>i</sup>, O10 and O10<sup>ii</sup>) is formed by two carboxylate O atoms and two aqua O atoms [symmetry codes: (i) 1-x, 1-y, 1-z; (ii) 1-x, 2-y, 1-z]. The axial positions are occupied by two pyridyl N atoms (N1, N1<sup>i</sup>, N3 and N3<sup>ii</sup>). The significant difference between the Co-O bond distances in the equatorial plane and Co-N bond distances in the axial positions has also been observed in another cobalt complex<sup>11,30</sup> [11,31]. The benzene and pyridine rings are almost planar, maximum deviations from the least-squares planes being 0.0052(20) Å for atom C4, 0.0174(17) Å for atom C20, 0.0124(19) Å for atom C8 and 0.0141(17) Å for atom N3.

## Supplementary material

Crystallographic data for the structures reported in this paper have been deposited with the Cambridge Crystallographic Data Center: CCDC-837593 contains the supplementary crystallographic data for this paper. These data can be obtained free of charge from The Cambridge Crystallographic Data Centre, www.ccdc.cam.ac.uk/data request/cif.

## Acknowledgements

The authors wish to acknowledge Hitit University Rectorate and the Faculty of Arts and Sciences, Ondokuz Mayıs University, Turkey, for the use of the Stoe IPDS-II diffractometer (purchased from Grant No. F279 of the University Research Fund).

## References

- Casasas, E., Izquierdo-Ridora, A., Tauler, R., *J. Chem. Soc., Dalton Trans.*, **1990**, 2341.
- Leban, I., Kozlevcar, B., Sieler, J., Segedin, P., *Acta Cryst.*, **1997**, C53, 1420.
- Motz, C., Roth, H. P., Kirchgessner, M., *Trace Elem. Electroly.*, **1995**, 12, 1.
- Petrovic, N., Kozlevcar, B., Golic, L., Leban, I., Segedin, P., *Acta Cryst.*, **1999**, C55, 176.
- Devereux, M., Curran, M., McCann, M., Casey, R. M. T., McKee, V., *Polyhedron*, **1996**, 15, 2029.
- Icbudak, H., Heren, Z., Kose, D. A., Necefoğlu, H., *J. Therm. Anal. Cal.*, **2004**, 76(3), 837.
- Sahin, O., Buyukgungor, O., Kose, D. A., Necefoğlu, H., *Acta Cryst.*, **2007**, C63, m510.
- Öztürkkan, E. F., Köse, D. A., Necefoğlu, H., Uzun, I., *Asian J. Chem.*, **2007**, 19(6), 4880.
- Köse, D. A., Kaya, A., Necefoğlu, H., *Russian J. Coord. Chem.*, **2007**, 33(6), 422.
- Köse, D. A., Necefoğlu, H., *J. Therm. Anal. Cal.*, **2008**, 93(2), 509.
- Sahin, O., Buyukgungor, O., Kose, D.A., Necefoğlu, H., *Acta Cryst.*, **2008**, C64, m317.
- Yeşilel, O. Z., Olmez, H., Uçar, I., Bulut, A., Kazak, C., *Z. Anorg. Allg. Chem.*, **2005**, 631, 3100.
- Chenoweth, M. B., *Pharmacol. Rev.*, **1956**, 8, 57.
- Sorenson, J. R. J., In: Siegel, H., (ed.) *Metal Ions in Biologicals, vol.14*, Marcel-Dekker, New York, **1982**.
- Reid, J., Watson, R. D., Cochran, J. B., Sproull, D. H., *British Med. J.*, **1951**, 1, 321.
- Olmez, H., Arslan, F., Icbudak, H., *J. Therm. Anal. Calor.*, **2004**, 76, 793.
- Geraghty, M., Sheridan, V., McCann, M., Devereux, M., McKee, V., *Polyhedron.*, **1999**, 18, 2931.
- Kose, D.A., Zumreoglu-Karan, B., Unaleroglu, C., Şahin, O., Buyukgungor, O., *J. Coord. Chem.*, **2006**, 17, 2125.
- Kose, D.A., Icbudak, H., Necefoğlu, H., *Hacettepe J. Biol. Chem.*, **2007**, 35(2), 123.
- Wolodkiewicz, W., Brzyska, W., *Polish J. Chem.*, **1997**, 71, 16.
- Erdelyiová, A., Györyová, K., Gyepes, R., Halás, L., Kovárová, J., *Polyhedron*, **2009**, 28, 131.
- Kose, D. A., Necefoğlu, H., Icbudak, H., *J. Coord. Chem.*, **2008**, 61(21), 3508.
- Sutton, D., *Electronic spectra of transition metal complexes. McGraw-Hill, London*, **1968**.
- Zelenák, V., Vargová, Z., Györyová, K., *Spectrochim. Acta A*, **2007**, 66, 262.
- Sheldrick, G. M., *Acta Cryst.*, **2008**, A64, 112.
- Farrugia, L. J., *J. Appl. Cryst.*, **1999**, 32, 837.
- Farrugia, L. J., *J. Appl. Cryst.*, **1997**, 30, 565.
- Spek, A. L., *PLATON—A Multipurpose Crystallographic Tool*, Utrecht University, Netherlands, **2005**.
- Bernstein, J., Davis, R. E., Shimon, L., Chang, N. L., *Angew. Chem. Int. Ed. Engl.*, **1995**, 34, 1555.
- Şahin, O., Büyükgüngör, O., Köse, D. A., Öztürkkan E. F., Necefoğlu, H., *Acta Cryst.*, **2007**, C63, m243.

Received: 20.09.2012.  
Accepted: 01.10.2012.



# EMISSION ESTIMATION TECHNIQUES FOR AMMONIUM NITRATE PRODUCTION

Ahmet Ozan Gezerman<sup>[a]\*</sup>

**Keywords:** Emission factor, emission estimation technique, emission factor code.

In the present study, an estimation calculation system is described according to the literature reviews available in Asian and European countries on the minimization of industrial emissions. On the basis of the calculations done, an approach is described for the calculation of emissions, and the procedure mentioned in the article, and referred to the National Pollutant Inventory (NPI) is also described.

\* Corresponding Authors

Fax: + 90 532 653 85 05

E-Mail: ahmet\_ozan@yahoo.com

[a] Department of Chemical Engineering,  
Yildiz Technical University, Istanbul, Turkey

## INTRODUCTION

A commonly used method for industrial fertilizer production and its emission calculation are described herein. Chemical fertilizer production is a process in which physical and chemical reactions take place<sup>1</sup>. The main purpose of this work is to investigate the changes in chemical structure that occur during fertilizer production. Different fertilizers are used in a variety of sectors depending on their chemical and thermal properties<sup>2</sup>. Table 1 outlines the most common fertilizers together with their compositions. One of the most commonly used fertilizers in the mining industry uses a mixture of ammonium nitrate and fuel oil<sup>3</sup>. The main products of the combustion of this mixture are CO, CO<sub>2</sub>, NOX, and H<sub>2</sub>O. For example, in Australia, it is estimated that the mining industry uses at least 600 000 tonnes of this mixture per annum<sup>4</sup>.

## EMISSION SOURCES AND CONTROL TECHNOLOGIES

### Emissions to Air

Emissions to air can be categorized as follows<sup>5</sup>:

#### Fugitive Emissions

There are many different emission forms from fertilizer production plants. Fugitive Emission is the waste form in the outline of a planned process. The chemical compositions of waste materials are different depending on the particular fertilizer. The emission factor is used for determining the mass loss.

#### Point Source Emissions

In terms of fertilizer production, this emission form concerns the waste gas emitted from a planned point. There are several reviews available in the literature regarding this form of emission.

### Emissions to Land

This describes the discharge of emission sources that are collected as waste water in production plants. There are several appropriate control technologies for emission reduction, each of which has a certain control efficiency. In this study, uncontrolled emissions are measured using some form of control technology and are classified according to their "emission factor", as given in Table 2.

## MATERIALS AND METHODS

An engineering calculation is an estimation method based on physical/chemical properties (e.g., vapor pressure of the substance) and mathematical relationships (e.g., ideal gas law). Example 1 shows how emissions of dinitrogen monoxide can be calculated. Some information is available on the chemical decomposition of fertilizers, so that the amounts of some substances listed in the National Pollutant Inventory (NPI), produced from the combustion process (e.g., carbon monoxide), can be calculated theoretically.

**Table 1.** Compositions of Fertilizers

Fertilizer	Composition
NPK	75/10/15 Nitrogen/Phosphorous/Potassium
Nitrate compounds	20–60% ammonium nitrate and sodium nitrate
Ammonium nitrate	Ammonium nitrate with 5.8–8% fuel oil
Amine complexes	Cyclotrimethylenetrinitroamine

### Example 1. Estimation of dinitrogen monoxide Emissions from the Production of Ammonium Nitrate

The result of the production of ammonium nitrate is represented by the following general reaction series, which forms the basis of the worked out example.

The final products of the production of ammonium nitrate are:



- a)  $2\text{N} \rightarrow \text{N}_2$
- b)  $4\text{H} + 3\text{O} \rightarrow 2\text{H}_2\text{O}$  (1 O remaining)
- c)  $2\text{N} + \text{O} \rightarrow \text{N}_2\text{O}$

The loss during the production



Total molecular weight of  $\text{NH}_4\text{NO}_3$ :  $(2 \times \text{N}) + (4 \times \text{H}) + (3 \times \text{O}) = (2 \times 14) + (4 \times 1) + (3 \times 16) = 28 + 4 + 48 = 80$ . Total Molecular weight of  $\text{N}_2\text{O} = 14 \times 2 + 16 = 44 \text{ kg mol}^{-1}$ . Total weight of  $\text{N}_2\text{O}$  from reaction =  $1 \text{ mol} \times 44 \text{ kg mol}^{-1} = 44 \text{ kg}$ . Total  $\text{N}_2\text{O}$  emission =  $(44/80) \times 1000 \text{ kg t}^{-1} = 550 \text{ kg}$  of  $\text{N}_2\text{O}$  produced per tonne of ammonium nitrate

### Emission Factors

The emission factor is a tool used to estimate emissions to the environment. In this paper, it relates the quantity of a substance emitted from a source to some common activity associated with those emissions. Emission factors are obtained from US, European, and Asian sources, and are usually expressed as the weight of a substance emitted divided by the unit weight, volume, distance, or duration of the activity through which the substance is emitted<sup>6</sup>.

Emission factors are used to estimate a facility's emissions by the general equation:

$$E_{kpy_i} = A * OpHrs * EF_i \left[ 1 - \frac{CE_i}{100} \right] \quad (3)$$

where:

- $E_{kpy_i}$  - emission rate of pollutant  $i$ ,  $\text{kg yr}^{-1}$
- $A$  - activity rate,  $\text{t h}^{-1}$
- $OpHrs$  - operating hours,  $\text{h yr}^{-1}$
- $EF_i$  - uncontrolled emission factor of pollutant  $i$ ,  $\text{kg t}^{-1}$
- $CE_i$  - overall control efficiency for pollutant  $i$ , %

Emission factors determined from measurements for a specific process can sometimes be used to estimate emissions. If a company has several processes of similar operation and size and emissions are measured from one process source, an emission factor can be determined and applied to similar sources. Examples of uncontrolled emission factors for fertilizers are given in Table 2.

Available theoretical, complex equalities and models in the literature are used to calculate the emission amounts during the production of fertilizers such as ammonium nitrate.

The use of equalities for the estimation of fertilizer production is more complex than the use of emission factors. Emission equalities require more data, but they ensure more accurate estimation depending on the specific conditions.

### Discussion

The main aim of this study is to ensure the realization of industrial production processes with sensitivity to the environment, and the development of new methods in order to obtain the best possible results. With this aim, new methods and models have recently been recommended to allow the description and better understanding of frequently mentioned emission problems.

With regard to the emission factors calculated by the NPI method (Table 2), it is clear that the emission levels need to decrease. For this, there are four methods for emission estimation provided in the NPI guidelines. In general, there are four emission estimation methods in the NPI Guidelines for production processes<sup>7</sup>:

- sampling or direct measurement;
- mass balance;
- fuel analysis or other engineering calculations;
- emission factors.

Any of these methods can be selected. For example, the mass balance method can be used for fugitive emissions. For the calculation at a detected point, the use of emission factors is a more suitable approach. Emission data estimated by using any of these methods will be displayed on the NPI database as measurements of "acceptable reliability."

Emission sources in fertilizer production are common. These may be different according to the type of fertilizer produced. Emission problems during production can be mitigated if we know what action the manufacture should take to decrease emissions. For this purpose, the preferred method of the known emission calculation methods is that of emission factors. Each emission factor is described by an emission factor rating (EFR) code<sup>8</sup>. This rating system is common for all similar industries. When using the emission factor approach, the emission factor code and its meaning should be understood. Ratings A and B describe bigger and more certain ratings than D and E. The given emission factor is not representative for a specific source or category.

The EFR system is as follows:

- A - Excellent
- B - Above Average
- C - Average
- D - Below Average
- E - Poor
- U - Unrated

**Table 2.** Uncontrolled Emission Factors for Fertilizers

Fertilizer	Emission factor (kg ton <sup>-1</sup> ) <sup>a</sup>					
	Carbon monoxide (CO)	Nitrogen Oxides (NO <sub>x</sub> )	Ammonia	Hydrogen cyanide (HCN)	Hydrogen Sulfide (H <sub>2</sub> S)	Sulfur dioxide (SO <sub>2</sub> )
Nitrate compounds	32	ND	NA	NA	16	NA
Ammonium nitrate	34	8	NA	NA	NA	1
Amine complexes	98	ND	22	NA	NA	NA
NPK	85	ND	NA	NA	12	NA

Source: Adapted from USEPA Document AP-42 (1995); <sup>a</sup> Units are kilograms (kg) of substance emitted per tonne (tonne) of fertilizer used; ND - No data available; NA - Not applicable.

## Conclusion

The most effective emission estimation techniques have been investigated according to the NPI values for emission estimation. As expected, direct measurement is the most reliable method for emission characterization. However, results from other calculation methods can be considered. For typical emission problems, there are four methods found in the literature for measuring emissions from a particular source. It should be mentioned that the emission of material mass to air, water, and land should be calculated using every method.

## References

- <sup>1</sup>ADI Smokeless Powders Handloader's Guide, 2nd ed., NSW, Australia. **1996**.
- <sup>2</sup>Coffey Geosciences Pty Ltd, *Personal Communication* with Coffey Geosciences Pty Ltd. Cooper, **1999**.

<sup>3</sup>Paul.W., *Fertilizers Engineering*, New York, N.Y.: VCH, USA. **1996**.

<sup>4</sup>Dyno Nobel, *Personal Communication* with Dyno Nobel, **1999**.

<sup>5</sup>Orica Australia, *Personal Communication* with Orica Australia, **1999**.

<sup>6</sup>Queensland Department of Mines and Energy, *Personal Communication* with the Queensland Department of Mines and Energy, **1999**.

<sup>7</sup>Ullmann, F., *Ullmann's Encyclopedia of Industrial Chemistry*, 5th ed., VCH, Weinheim, Germany. **1987**.

<sup>8</sup>USEPA, *Compilation of Air Pollutant Emission Factors, Volume 1: Stationary Point and Area Sources, fifth edition, AP-42, Section 13, Fertilizers Detonation*, United States Environmental Protection Agency, Office of Air Quality Planning and Standards. Research Triangle Park, NC, USA. **1995**.

Received: 27.09.2012.  
Accepted: 02.10.2012.



# Synthesis and Structural Study of the Ion-Associates of Sildenafil Citrate with Chromotropic Acid Azo Dyes

Y.M. Issa<sup>[a]</sup>, W.F. El-Hawary<sup>[a,b]\*</sup>, A.F.A. Youssef<sup>[a]</sup>, A.R. Senosy<sup>[a]</sup>

**Keywords:** sildenafil citrate, chromotropic acid azo dyes, Vis spectrophotometry, IR spectra.

Five ion-associates of the drug sildenafil citrate (SC) with mono-chromotropic acid azo dyes, chromotrope 2B (I) and chromotrope 2R (II), and chromotropic acid bi-azo dyes, bis-3,6-(*o*-hydroxyphenylazo)-chromotropic acid (III), bis-3,6-(*p*-N,N-dimethylphenylazo)-chromotropic acid (IV) and 3-phenylazo-6-*o*-hydroxyphenylazo-chromotropic acid (V) have been synthesized. Structural characterization of these novel sildenafil citrate ion-associates was carried out using elemental analysis and spectral techniques (VIS and IR). IR absorption spectra of the investigated ion-associates are studied and compared with those of the pure azo dyes and the drug. The spectral characteristics, oscillator strengths, transition dipole moments and resonance energy of the ion-associates in the ground state have also been calculated.

Corresponding Author

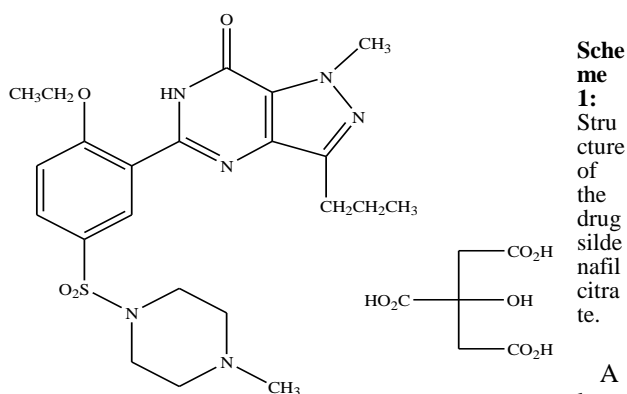
E-Mail: waheedfathi@yahoo.com

[a] Chemistry Department, Faculty of Science, Cairo University, Gamaa Street, Giza, Egypt

[b] Chemistry Department, Faculty of Science, Taif University, Taif, KSA

## Introduction

Sildenafil citrate is designated chemically as 1-[[3-(6,7-dihydro-1-methyl-7-oxo-3-propyl-1H-pyrazolo[4,3-d]pyrimidin-5-yl)-4-ethoxyphenyl]sulfonyl]-4-methylpiperazine citrate [CAS 139755-83-2] and has the structure shown as Scheme 1. Sildenafil citrate is a compound of the pyrazolo-pyrimidinylmethylpiperazine class. It is a selective inhibitor of cyclic guanosine monophosphate (cGMP)-specific phosphodiesterase inhibitors type 5 (PDE5).<sup>1</sup> Singh et al.<sup>2</sup> reviewed and generalized strategies for characterizing adulteration of PDE-5 inhibitors drugs (sildenafil, vardenafil and tadalafil) by using modern, sensitive and selective analytical techniques such as, liquid chromatography with tandem mass spectrometry, Fourier transform (FT) with near infrared spectrometry, and FT with Raman spectrometry. Structure elucidation of a novel synthetic thiono analogue of sildenafil<sup>3</sup> detected in an alleged herbal aphrodisiac was established using LC-MS, UV and IR spectroscopy, MS, and NMR. Kim et al.<sup>4</sup> synthesized new sildenafil analogues containing an ether ring fused into the phenyl ring.



others analogues of sildenafil, including homosildenafil,<sup>5-8</sup> hydroxyhomosildenafil,<sup>7,8</sup> acetildenafil,<sup>7-10</sup> hydroxyacetildenafil<sup>11</sup> and methisosildenafil,<sup>12</sup> have been detected in dietary supplements. Sildenafil citrate (Viagra)

and sildenafil base in pure form are easily and unequivocally characterized by multinuclear nuclear magnetic resonance (NMR) spectroscopy.<sup>13</sup> Two molecularly imprinted polymers (MIPs) as selective sorbents for the solid-phase extraction of sildenafil and its principal metabolite, desmethylsildenafil, were synthesised<sup>14</sup>, using structural analogues of sildenafil as templates.

Chromotropic acid (4,5-dihydroxynaphthalene-2,7-disulphonic acid) is used for preparation of azo dyes which are well known indicators for spectrophotometric determination of metal ions.<sup>15,16</sup> The synthesis and structural study of azo dyes and their complexes was the subject of many new researches.<sup>17-20</sup> The IR spectra of azo dyes were investigated,<sup>21,22</sup> these studies were mainly concerned with the N=N band assignment. Abdel-Ghani et al.<sup>23</sup> presented potentiometric, IR and thermal conductimetric studies on chelates of chromotropic acid with some transition metals. Some azo dyes and their metal complexes were characterized by multinuclear NMR.<sup>24</sup>

In the present study, elemental analysis, electronic and vibrational analyses were applied to investigate the structure of the prepared sildenafil citrate ion-associates with some chromotropic acid azo dyes.

## Experimental

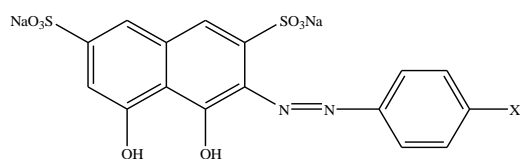
### Instrumentation

Shimadzu FTIR spectrophotometer was used to record IR spectra (on KBr) in the range of 400–4000 cm<sup>-1</sup>. The UV-VIS spectrophotometer model 22 Labomed was used for all spectrophotometric measurements. Elemental analyses were carried out using automatic CHN analyzer (Perkin-Elmer model 2400) at the Microanalytical Center, Faculty of Science, Cairo University.

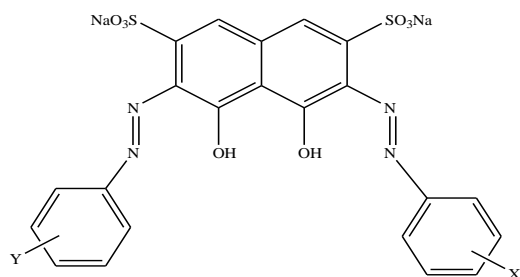
### Reagents

All chemicals used were of the analytical reagent grade. sildenafil citrate was a product of Alkan Pharmaceutical Industries, Cairo, Egypt. Chromotrope 2B (I) and

chromotrope 2R (II) were obtained from Sigma (USA); their structure is shown in Scheme 2. Bi-chromotropic acid azo dyes (III-V) were prepared by diazotization of the corresponding amines with chromotropic acid.<sup>25</sup> The resulting precipitate was re-crystallized<sup>26</sup> (Scheme 3).



**Scheme 2:** Structure of mono-chromotropic acid azo dyes.



**Scheme 3:** Structure of bi-chromotropic acid azo dyes.

## Synthesis

The new solid ion-associates of SC with mono- and bi-azo dyes of chromotropic acid were prepared; 0.1 mmol (0.0513 g) of (I), 0.0468 g of (II), 0.0604 g of (III), 0.0658 g of (IV) and 0.0588 g of (V) were dissolved in about 30 mL methanol and added to 0.2 mmol (0.1332 g) and 0.1 mmol (0.0666 g) of the drug SC for preparation of solid ion-associates of SC with mono-azo (I and II) and bi-azo (III-V) dyes of chromotropic acid, respectively, the drug SC was dissolved in 30 mL of the same solvent. The dye solutions were added slowly to the individual SC solutions with constant stirring. The resulting mixtures were subjected to vigorous stirring, and then the mixture was left until the complete solvent vaporization. The resulting precipitates were filtered, washed thoroughly with petroleum ether and then dried at the room temperature to have fine powder. The structures of the precipitates were determined by elemental analysis, IR and Vis measurements.

## Results and discussion

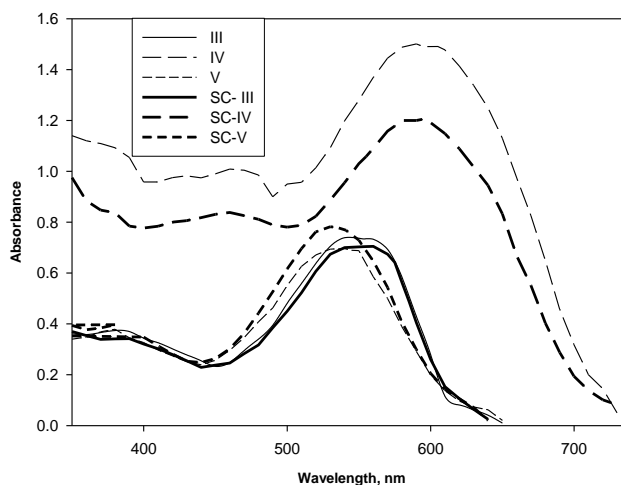
### Microanalysis of SC Solid ion-associates

Table 1 contains the elemental analysis results of the chromotropic acid azo dyes (I-V) ion-associates with the investigated drug (SC). It is noteworthy to mention that the found values of the different elements are in good agreement with the calculated values according to the proposed molecular formulae of the ion-associate. The obtained data reveal that the SC-I and SC-II ion-associates are formed in a

ratio of 2:1 (drug:dye) with a molecular formula of 2SC-(I-II).  $n\text{H}_2\text{O}$ , while SC-(III-V) ion-associates are formed in a ratio of 1:1 (drug:dye) with a molecular formula SC-(III-V).  $n\text{H}_2\text{O}$ , where n is the number of water molecules.

### Visible Spectra of SC Solid ion-associates

The absorption spectra of the azo dyes (I-V) under investigation and also their resulting solid ion-associates with the drug SC were studied against dimethylformamide (DMF) blank. The present spectral measurements were confined to the visible region within the wavelength range 300-600 nm (Figs. 1, 2) using DMF as solvent. The absorption maxima and the molar absorptivities of the azo dyes and their corresponding solid ion-associates are recorded in table 2. The small shift in the absorption maxima and variation in the molar absorptivities values for the reaction products relative to those of pure azo dyes is an indication for the formation of the new ion-associate



compounds.

**Figure 1.** Absorption spectra of the reagents I and II III- V and their corresponding ion- in DMF solvent

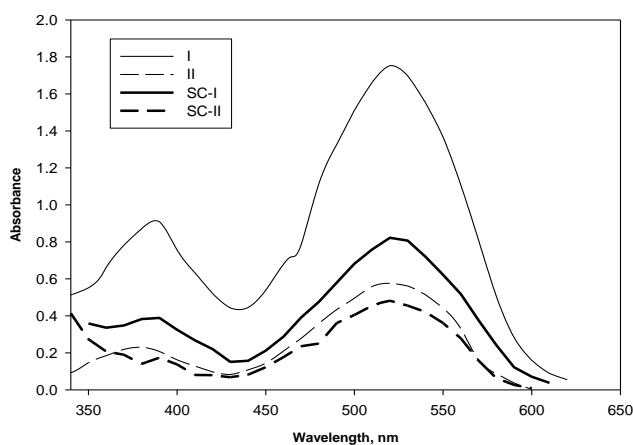


**Figure 2.** Absorption spectra of the reagents corresponding ion- and their associates with SC pairs with SC in DMF solvent.

**Table 1:** Data of elemental analysis of the investigated SC ion-associates.

Ion-associate	Chemical formulae	Colour of precipitate	Found (Calc.)			
			C%	H%	S%	N%
SC-I	C <sub>38</sub> H <sub>39</sub> N <sub>9</sub> O <sub>14</sub> S <sub>3</sub> . 10H <sub>2</sub> O	Red	45.72 (45.56)	5.27 (4.26)	7.36 (7.91)	9.97 (11.44)
SC-II	C <sub>38</sub> H <sub>40</sub> N <sub>9</sub> O <sub>14</sub> S <sub>3</sub> . 10H <sub>2</sub> O	Pink	42.69 (45.77)	5.46 (4.49)	7.64 (8.14)	9.98 (11.40)
SC-III	C <sub>44</sub> H <sub>45</sub> N <sub>10</sub> O <sub>14</sub> S <sub>3</sub> Na. 8H <sub>2</sub> O	Black	44.96 (43.99)	4.50 (5.07)	7.50 (8.00)	9.91 (11.05)
SC-IV	C <sub>48</sub> H <sub>54</sub> N <sub>12</sub> O <sub>12</sub> S <sub>3</sub> Na. 12H <sub>2</sub> O	Dark violet	41.90 (43.47)	5.10 (5.80)	6.47 (7.25)	10.04 (12.06)
SC-V	C <sub>44</sub> H <sub>44</sub> N <sub>10</sub> O <sub>13</sub> S <sub>3</sub> Na. 6H <sub>2</sub> O	Black	43.55 (46.00)	4.50 (4.87)	7.36 (8.37)	9.18 (11.10)

### Infrared Spectra

The infrared spectra (IR) of sildenafil citrate (SC) and some of the studied reagents (I-V) and their ion-associates were recorded in the range 4000-400 cm<sup>-1</sup> using KBr discs. Table 3 shows the IR band assignment of the investigated SC ion-associates. The main diagnostic bands in SC ion-associates are assigned in the following discussion. The IR spectra are represented in Figs. 3 and 4.

**Table 2:** Absorption spectral data of the investigated chromotropic acid azo dyes and their ion-associates with SC

	$\lambda_{\max}$ (nm)	$\epsilon_{\max} \times 10^3, \text{L mol}^{-1} \text{cm}^{-1}$
I	515	12.27
I-SC	520	10.93
II	520	2.99
II-SC	520	4.88
III	540	12.40
III-SC	560	11.37
IV	580	21.10
IV-SC	595	10.80
V	540	11.37
V-SC	530	18.04

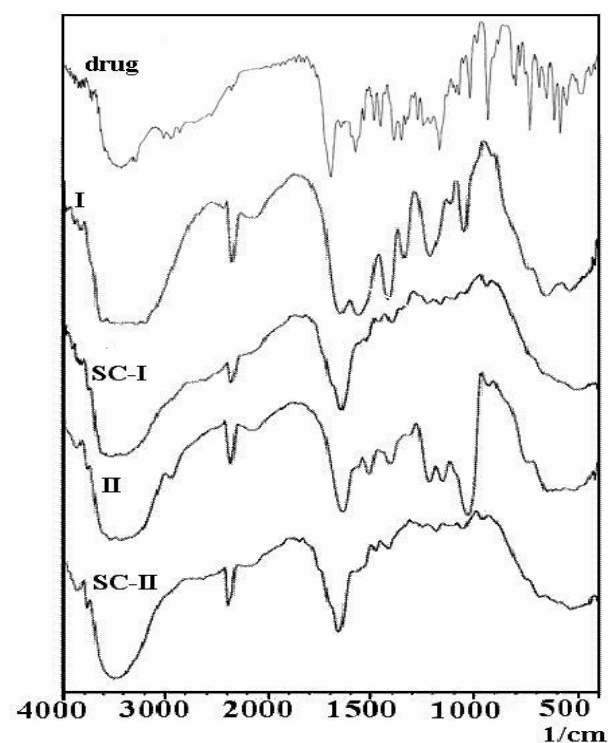
#### Hydroxyl bands

The infrared spectra of the chromotropic acid azo dyes and their ion-associates with SC show a broad hydroxyl group band. The intensity of this band is considerably greater than that of the free OH-vibration frequency. The broad shape can be attributed to the fact that the OH group is involved in hydrogen bonding. One of the two OH groups of chromotropic acid can form an intramolecular hydrogen bond with the azo group while the other one forms an intermolecular hydrogen bond with the oxygen of the  $\alpha$ -OH- group.<sup>27</sup> The band is slightly affected by the nature and position of the substituent (Table 3). There is another absorption band also in the lower frequency region which attributed to OH- deformation occurs around 1100 cm<sup>-1</sup>.

#### Absorption in the 1700–1400 cm<sup>-1</sup> region

This is the region of interest, since it involves bands due to C=O, C=N, C=C, and N=N. The IR-spectra of the drug SC shows two bands at 1701 and 1615 cm<sup>-1</sup>, these bands are assigned to the carbonyl group C=O<sup>28</sup> and vibration of C=N. These bands are shifted to lower or higher frequencies in the IR-spectra of the SC-(I-V) ion-associates, which indicate the formation of new ion-associate between the drug and the investigated azo dyes.

The IR-spectra of the compounds show bands near 1690, 1600 and 1500 cm<sup>-1</sup>. These bands are due to skeletal stretching vibrations C=C. The position of the bands is influenced to a small extent by the nature of substituent groups. However, they depend on a rather greater degree, on the way in which the latter are arranged around the ring. The vibration due to the azo link (N=N) of chromotropic acid azo dyes<sup>27</sup> differ than that of their ion-associates indicating that it has been affected by the reaction with SC.

**Figure 3.** IR spectra of the drug sildenafil citrate and reagents I and II and their ion-associates with the drug (SC-I and SC-II)

#### Absorption in the 1400–600 cm<sup>-1</sup> Region

This region involves other bands such as C–N stretching vibration, C–O stretching vibration and the aromatic C–H out of plane deformation.<sup>29</sup> C–N and C–O stretching vibration bands are found around 1300 and 1200 cm<sup>-1</sup>, respectively. Their positions vary considerably with structural effects. The vibration bands assigned to the aromatic C–H out of plane deformation are observed near 990 cm<sup>-1</sup>. The IR-spectra of chromotropic acid azo dyes indicate that the sulphonic acid group absorbs within the range 1190-1212 cm<sup>-1</sup> (broad) and 1037-1045 cm<sup>-1</sup> (strong or medium) with a third band around 640 cm<sup>-1</sup>.<sup>27</sup>

**Table 3.** Assignment of IR bands of SC and its ion-associates with the investigated chromotropic acid azo dyes.

SC	I	SC-I	II	SC-II	III	SC-III	IV	SC-IV	V	SC-V	Vibrational assignment
3398 <sup>b</sup>	3190 <sup>b</sup>	3244 <sup>b</sup>	3325 <sup>b</sup>	3414 <sup>b</sup>	3445 <sup>b</sup>	3425 <sup>b</sup>	3372 <sup>b</sup>	3440 <sup>b</sup>	3425 <sup>b</sup>	3425 <sup>b</sup>	νOH
1701 <sup>s</sup>	-	1639 <sup>b</sup>	-	1639 <sup>b</sup>	-	1693 <sup>w</sup>	-	1635 <sup>b</sup>	-	1693 <sup>w</sup>	νC=O
-	1643 <sup>w</sup>	1639 <sup>b</sup>	1639 <sup>m</sup>	1639 <sup>s</sup>	1628 <sup>w</sup>	1693 <sup>w</sup>	1601 <sup>b</sup>	1636 <sup>b</sup>	1620 <sup>w</sup>	1616 <sup>w</sup>	νC=C skeletal vib.
1539 <sup>w</sup>	1558 <sup>w</sup>	-	1566 <sup>w</sup>	1558 <sup>w</sup>	1566 <sup>w</sup>	1643 <sup>w</sup>	-	-	1570 <sup>w</sup>	-	νC=C skeletal vib.
1581 <sup>m</sup>	-	1523 <sup>w</sup>	1504 <sup>w</sup>	-	1500 <sup>w</sup>	1500 <sup>w</sup>	-	-	1508 <sup>m</sup>	1497 <sup>w</sup>	νC=C skeletal vib.
1651 <sup>w</sup>	-	1639 <sup>b</sup>	-	1639 <sup>b</sup>	-	1616 <sup>w</sup>	-	1636 <sup>b</sup>	-	1643 <sup>w</sup>	νC=N
-	1416 <sup>m</sup>	1404 <sup>w</sup>	1404 <sup>w</sup>	1462 <sup>w</sup>	1474 <sup>w</sup>	1462 <sup>w</sup>	1435 <sup>w</sup>	1393 <sup>w</sup>	1400 <sup>m</sup>	1462 <sup>w</sup>	νN=N
1338 <sup>w</sup>	1338 <sup>m</sup>	1354 <sup>w</sup>	1312 <sup>w</sup>	1400 <sup>w</sup>	1396 <sup>m</sup>	1357 <sup>w</sup>	1377 <sup>m</sup>	1392 <sup>m</sup>	1296 <sup>w</sup>	1396 <sup>w</sup>	νC-N
-	1211 <sup>s</sup>	-	1219 <sup>b</sup>	-	1215 <sup>b</sup>	-	1284 <sup>m</sup>	-	1219 <sup>b</sup>	-	νSO <sub>3</sub> <sup>-</sup>
1219 <sup>w</sup>	1211 <sup>s</sup>	1164 <sup>w</sup>	1218 <sup>w</sup>	1165 <sup>w</sup>	1215 <sup>b</sup>	1165 <sup>w</sup>	-	1158 <sup>w</sup>	1219 <sup>w</sup>	1165 <sup>w</sup>	νC-O
-	1041 <sup>s</sup>	1045 <sup>w</sup>	1038 <sup>s</sup>	1038 <sup>w</sup>	1045 <sup>s</sup>	1042 <sup>s</sup>	1042 <sup>s</sup>	1041 <sup>w</sup>	1045 <sup>s</sup>	1042 <sup>s</sup>	νSO <sub>3</sub> <sup>-</sup>
-	665 <sup>m</sup>	-	-	-	640 <sup>w</sup>	-	-	-	640 <sup>w</sup>	-	vibrations due to SO <sub>3</sub> <sup>-</sup>
941 <sup>s</sup>	-	937 <sup>w</sup>	-	-	-	995 <sup>w</sup>	-	933 <sup>m</sup>	-	991 <sup>w</sup>	δC-H out-of-plan def.

b: broad, s: strong, m: medium and w: weak.

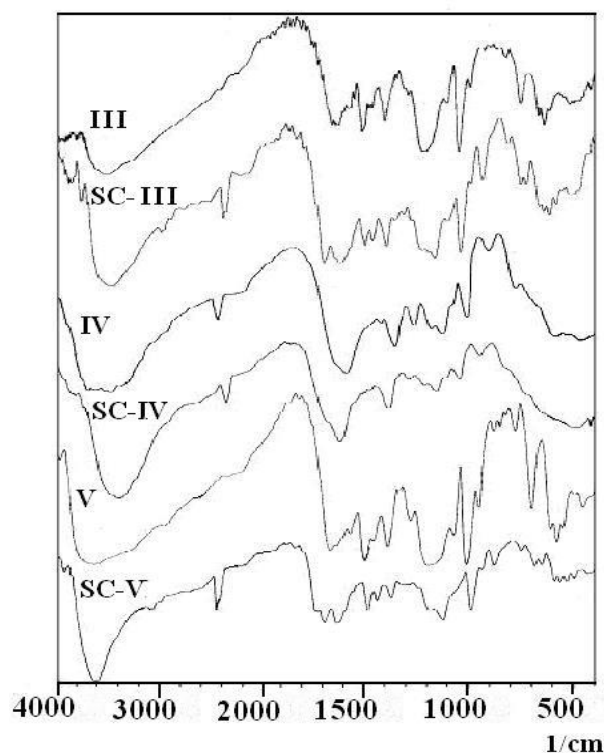


**Figure 4.** IR spectra of reagent III-V and their ion-pairs with sildenafil citrate.

#### Spectral Characteristics of the Solid ion-associates

The oscillator strength ( $f$ ), which is a dimensionless quantity used to express the transition probability of the complex band<sup>30</sup>, and the transition dipole moment ( $\mu_{EN}$ ) of the ion-associate complexes<sup>31</sup> were calculated from the following equations:

$$f = 4.32 \times 10^{-9} [\epsilon_{\max} \Delta\nu_{1/2}] \quad (1)$$

$$\mu = 0.0958 \left[ \frac{\epsilon_{\max} \Delta\nu_{1/2}}{\nu_{\max}} \right]^{1/2} \quad (2)$$

where  $\Delta\nu_{1/2}$  is the band width of the absorption peak at its half height,  $\epsilon_{\max}$  and  $\nu_{\max}$  are the extinction coefficient (molar absorptivity) and the wave number at the maximum absorption of the ion-associate, respectively. In these equations,  $\nu$  has been expressed in  $\text{cm}^{-1}$  unit. Results are shown in Table 4. The relative low values of  $f$  indicate a weak interaction between the cation–anion pairs.<sup>32</sup> The  $R_N$  is the resonance energy of the ion-associate in the ground state, which is obviously a contributing factor to the stability constant of the ion-associate (a ground state property), can be determined by following equation.<sup>33</sup>

$$\epsilon_{\max} = \frac{7.7 \times 10^4 |R_N|}{h\nu_c} - 3.5 \quad (3)$$

where  $\nu_c$  is the frequency of the absorption band of the ion-associate at maximum absorption. Resonance energies for the SC ion-associates with different chromotropic acid azo dyes are given in Table 4.

#### Conclusion

A new class of sildenafil citrate ion-associate compounds with chromotropic acid azo dyes has been synthesized and characterized. The results obtained in the present study showed that, the elemental analysis values of C, H, N and S are in good agreement with the calculated values according to the proposed molecular formulae of the ion-associates. The small shift in the absorption maxima ( $\lambda_{\max}$ ) in the VIS spectra and the change in the molar absorptivity values of the solid ion-associates relative to those of pure azo dyes reveal the formation of new ion-associates. This, also, was confirmed by the change in the position of the IR spectral bands of the prepared solid ion-associate compounds.

**Table 4:** The UV-spectral properties of the solid ion-associates of sildenafil citrate with reagents (I-V), absorption maxima ( $\lambda_{\max}$ ), transition energy ( $h\nu_{\max}$ ), molar absorptivity ( $\epsilon$ ), oscillator strength ( $f$ ), transition dipole moment ( $\mu_{\text{EN}}$ ), resonance energy (RN) and wave number of maximum absorption ( $\nu_{\max}$ ).

Parameter	Reagent				
	I	II	III	IV	V
$\lambda_{\max}$ (nm)	520	520	560	595	530
$h\nu_{\max}$ (eV)	3.82	3.82	3.55	3.34	3.75
$\epsilon$ (L mol <sup>-1</sup> cm <sup>-1</sup> )	10.93 x10 <sup>3</sup>	4.88x10 <sup>3</sup>	11.37x10 <sup>3</sup>	8.10x10 <sup>3</sup>	18.07x10 <sup>3</sup>
$f$	4.72 x10 <sup>-10</sup>	1.83 x10 <sup>-10</sup>	5.40x10 <sup>-10</sup>	4.54x10 <sup>-10</sup>	8.82x10 <sup>-10</sup>
$\mu_{\text{EN}}$ (Debye)	2.28x10 <sup>-4</sup>	1.42x10 <sup>-4</sup>	2.53x10 <sup>-4</sup>	2.39x10 <sup>-4</sup>	3.15x10 <sup>-4</sup>
RN (eV)	0.362	0.198	0.345	0.268	0.483
$\nu_{\max}$ (cm <sup>-1</sup> )	1.92x10 <sup>4</sup>	1.92x10 <sup>4</sup>	1.78x10 <sup>4</sup>	1.68x10 <sup>4</sup>	1.88x10 <sup>4</sup>

- <sup>1</sup>Viagra®: (Sildenafil citrate) the FDA Approved Impotence Pill, Pfizer labs., Division of Pfizer Inc., New York, **1999**.
- <sup>2</sup>Singh, S., Prasad, B., Savaliya, A. A., Shah, R. P., Gohil, V. M. and Kaur, A., *Trends in Anal. Chem.*, **2009**, 28, 13.
- <sup>3</sup>Venhuis, B. J., Zomer, G. and de Kaste, D., *J. Pharm. Biomed. Anal.*, **2008**, 46, 814.
- <sup>4</sup>Kim, D., Lee, N., Lee, J. Y., Ryu, D. H., Kim, J., Lee, S., Choi, J., Chang, K., Kim, Y., Im, G., Choi, W., Kim, T., Ryu, J., Kim N. and Lee, K., *Bioorg. Med. Chem.*, **2001**, 9, 1609.
- <sup>5</sup>Gratz, S. R., Flurer, C. L., and Wolnik, K. A., *J. Pharm. Biomed. Anal.*, **2004**, 36, 525.
- <sup>6</sup>Shin, M. H. Hong, M. K., Kim, W. S., Lee, Y. J. and Jeoung, Y. C., *Food Addit. Contam.*, **2003**, 20, 793.
- <sup>7</sup>Blok-Tip, L., Zomer, B., Bakker, F., Hartog, K. D., Hamzink, M., Ten Hove, J., Vredendregt, M. and de Kaste, D., *Food Addit. Contam.*, **2004**, 21, 737.
- <sup>8</sup>Zou, P., Oh, S. S., Hou, P., Lowand, M. Y., Koh, H. L., *J. Chromy. A*, **2006**, 1104, 113.
- <sup>9</sup>Shin, C., Hong, M., Kim, D. and Lim. Y., *Magn. Reson. Chem.*, **2004**, 42, 1060.
- <sup>10</sup>Lai, K. C., Liu, Y. C., Tseng M. C. and Lin, J. H., *Yaowu Shipin Fenxi*, **2006**, 14, 19.
- <sup>11</sup>Hou, P., Zou, P., Low, M. Y., Chan, E. and Koh, H. L., *Food Addit. Contam.*, **2006**, 23, 870.
- <sup>12</sup>Reepmeyer, J. C. Woodruff, J. T. and Avignon, D. A. *J. Pharm. Biomed. Anal.*, **2007**, 43, 1615.
- <sup>13</sup>Wawer, I., Pisklak, M. and Chilmonczyk, Z. *J. Pharm. Biomed. Anal.*, **2005**, 38, 865.
- <sup>14</sup>Dzygiel, P., O'Donnell, E., Fraier, D., Chassaing, C. and Cormack, P. A. G., *J. Chromy. B*, **2007**, 853, 346.
- <sup>15</sup>Prakash, O. and Mushran, S. P. *Chim. Anal.* **1967**, 49, 473.
- <sup>16</sup>Shibata, S., Uchiumi, A., Sasaki, S. and Goto, K., *Anal. Chim. Acta*, **1969**, 44, 345.
- <sup>17</sup>Yazdanbakhsh, M. R., Mohammadi, A., Mohajerani, E., Nemati, H., Hosain Nataj, N., Moheghi, A. and Naeemikhah, E., *J. Mol. Liq.*, **2010**, 151, 107.
- <sup>18</sup>Pavlović, G., Racané, L., Čičak, H. and Tralić-Kulenović, V., *Dyes and Pigments*, **2009**, 83, 354.
- <sup>19</sup>Nejati, K., Rezvani Z. and Seyedahmadian, M., *Dyes and Pigments*, **2009**, 83, 304.
- <sup>20</sup>Khanmohammadi H. and Darvishpour, M., *Dyes and Pigments*, **2009**, 81, 167.
- <sup>21</sup>Le Fèvre, R. J. W., O'Dwyer, M. F. and Werner, R. L. *Aust. J. Chem.*, **1953**, 6, 341.
- <sup>22</sup>Dolinsky, M. and Jones. J. H., *J. Assoc. Offic. Agr. Chemists*, **1954**, 37, 197.
- <sup>23</sup>Abdel-Ghani, N. T., Issa, Y. M., Khaled, M. A., and El-Kottamy, M. H., *Thermochim. Acta*, **1988**, 125, 163.
- <sup>24</sup>Lyčka, A. *Ann. Report NMR Spectr.*, **2000**, 42, 1.
- <sup>25</sup>Ishibashi, M. I. and Higashi, S., *Jpn. Anal.*, **1955**, 4, 14.
- <sup>26</sup>Mehata, C. D. and Shan, K. H. *Indian J. Appl. Chem.*, **1966**, 29, 122.
- <sup>27</sup>Khalifa, H., Etaiw, S. H., Issa, Y. M. and Haj-Hussein, A.T. *Egypt. J. Chem.*, **1975**, 18, 855.
- <sup>28</sup>Melnikov, P. Corbi, P. P., Cuin, A. Cavicchioli, M. and Guimaraes, W. R., *J. Pharm. Sci.*, **2003**, 92, 2140.
- <sup>29</sup>Bellamy, L. J. *The Infrared Spectra of Complex Molecules*, Champan and Hall, London, **1975**.
- <sup>30</sup>Lever, A. B. P., *Inorganic Electronic Spectroscopy*, 2nd ed., Elsevier, Amsterdam, **1985**, 161.
- <sup>31</sup>Tsubomura H. and Lang R., *J. Am. Chem. Soc.*, **1964**, 86, 3930.
- <sup>32</sup>Pandeeswaran, M. and Elango. K. P., *Spectrochim. Acta A*, **2006**, 65, 1148.
- <sup>33</sup>Briegleb, G. and Czekalla, J. Z., *Phys. Chem.*, **1960**, 24, 37.

Received: 29.09.2012.  
Accepted: 02.10.2012.



## AN OVERVIEW OF WAX UTILIZATION IN CHINA

Zhang Xiaoli<sup>[a]\*</sup>**Keywords:** China; wax; overview; utilization; feedstock

The utilization of wax as a raw material has been reviewed. Adding wax feedstock into rubber products, leather, food, synthesis of castor oil phosphate, tail gas recovery and electrodes has also been discussed. The complete utilization most of the wax sources in China has also been evaluated.

\* Corresponding Author

Fax: 86-24-56860869

E-Mail: fszxi69@163.com

[a] Liaoning Shihua University, Fushun, Liaoning, P.R. China.

## Introduction

Wax during the oil refinery process is one of the important chemical products. It is a white to yellowish-white, gelatinous, crystalline water-insoluble substance. Its main content includes n-paraffin. Its carbon number, molecular weight, distillation range and density are 16-32, 300-540, 350 °C -500°C and 0.880-0.915, respectively.<sup>1</sup> Wax plays an important role in *Chinese* industries such as lighting, packaging, farming, chemicals, rubber, medicine and homecare products, etc. *China* owns a considerable amount of wax. *Shengbei*, *Daqing* and *Nanyang*'s oil have high wax contents. The production of wax in *China* reached 147.9 million tons which was about one third of the total production of wax in world during 2005.<sup>2</sup>

In the present paper, the output and import of *Chinese* wax, adding wax feedstock into rubber products, leather, food, synthesis of castor oil phosphate, tail gas recovery and electrodes has been reviewed, including a detailed comparison between output and import of *Chinese* wax also.

## Discussion

### Comparing between output and import of *Chinese* wax

Table 1 shows output and import of *Chinese* wax. There were more waxes distributed in Northeast of *China* such as *Yanshan*, *Dalian*, *Fushun*, *Jinxi* and *Daqing*. Their output were about half of the production of *Chinese* wax. The production of plants, which were near sea (*Gaojiao*, *Jinan* and *Maoming*), was about one fourth of *Chinese* total wax output. Food grade wax and completely refined wax were about 5% and 50% of *Chinese* total wax output, respectively.<sup>3</sup> Utilization of *Chinese* wax in the rubber industry<sup>4</sup>

Rubber during the storage and usage is easily cracked due to aging such as light, oxygen, ozone, heat and machinery. Wax derived from the oil refinery process is a solid compound having white to yellowish-white colour. It never reacts with rubber during the rubber production, however it freely swims in rubber.

It slowly moves on the surface of rubber because of low wax content on the surface of rubber. There is a layer of preventive film in the surface of rubber as time increases, rubber avoids making a direct contact with oxygen, so it decreases aging by the addition of wax into rubber. Different variety of waxes have different functions, therefore, people prefer it to take maximum benefits based on its properties.

### Utilization of *Chinese* wax in the leather industry<sup>5</sup>

In general, people usually have two requirements for leather. First one is increasing glossiness and second one is natural beauty as true leather. Manufactures use two methods to satisfy people's requirement, (1) its property is changed such as oxidation and esterification reaction; (2) as a main feedstock is blended to produce emulsified wax with other products such as resin, surfactant, aids and solvent. Its derivative is used at the top of leather, which increases glossiness and radiance of leather.

### Utilization of *Chinese* wax in the food industry<sup>6</sup>

Food products are packaged by using paper coated with wax or wax as adhesion agent in the food industry. Wax products can be coated to the surface of fruit also. It is dissolved into gasoline and then sprays to the surface of fruit, which not only avoids fruit to dry or spoil, but also prevents insects attack. In the poultry industry, poultry products are put in melted wax and then are cooled until wax settles. Using a machine to remove wax from the surface of poultry, so poultry's feathers will leave into wax.

### Utilization of *Chinese* wax in the castor oil phosphate<sup>7</sup>

Using wax and its derivative as P<sub>2</sub>O<sub>5</sub> dispersant obviously decreased the reaction time of castor oil phosphate and prevented P<sub>2</sub>O<sub>5</sub> making big particles. Finally it was observed that the yield of products increased by 7% and the MAP content of phosphate. Castor oil phosphate is widely used in the various areas such as leather, fur, textile, printing and dyeing, daily chemicals, etc.

**Table 1.** Output and import and Chinese wax (million tons)

Unit	Total output	Fully refined wax	Semi-refined wax	Food grade wax	Crude scale wax	Soap wax	Others	Import yield	Incremental yield
Yanshan	6.2367	0.2635	5.9672	0.0060				0.8100	2
Dalian	16.9049	3.6955	2.6429	5.0866	4.1347	1.3452		5.6456	3
Fushun	22.1638	5.4645	10.9573	0.2010	0.3275	5.2135		5.1944	15
Jinxi	3.2186		1.8001			1.4185		0.9557	
Daqing	13.0773	0.0140	12.6222	0.1779	0.2220	0.0552		8.9290	2
Gaojiao	10.8195	1.4019	6.4534		1.5655		1.3987		3
Jinan	1.0202				1.0202				
Luoyang	0.1541		0.1541						
Jingmen	7.5395		2.9824		0.7686		0.0324	1.4354	2
Maoming	8.1736		2.1812	0.0422		0.6720		4.3247	2
Lanzhou	2.8857		0.6064		0.7943	1.4850			10.5
Jiangnan	1.0429		0.9409		0.1020				
Qingdao	0.0007	0.0007							
Jilin	0.0829	0.0829							
Yumen	0.0643		0.0643						
Nangchong	0.4627		0.3594		0.1843				
Total	93.8478	10.9230	47.7318	5.5137	9.1191	10.1894	1.4311	27.2948	39.5

### Utilization of Chinese wax in the tail gas recovery <sup>8</sup>

In the cotton industry, gases from cotton seed cake unit include some solvents. They have a bad effect on the energy standard and safe production of cotton seed cake unit. Using wax can remove solvent from gases. Tail gases may reach the qualifying standard to discharge into atmosphere.

### Utilization of Chinese wax in electrodes <sup>9</sup>

Mao Qinglu used solid wax as an adhesive agent to produce carbon paste electrodes. The carbon paste electrodes have high activity. Their property can be studied under unstable condition. Other electrodes cannot replace them.

### Conclusion

Based on the above review, wax is widely used in different areas such as rubber products, leather, food, synthesis of caster oil phosphate, tail gas recovery and electrodes. China owns a considerable amount of paraffin base petroleum and high quality wax.

It is an urgent need for Chinese people to utilize wax sources in a more rational way, involving new processes, which could result in improving the product's value. These newer processes may improve the energy efficiency and decrease the environmental pollution as well.

### References

- <sup>1</sup> Chang, Y. H. *Chem. Prod. Technol.*, **2002**, 9(6), 6.
- <sup>2</sup> Wang, J. *Int. Petro. Econ.*, **2005**, 12, 20.
- <sup>3</sup> Guo, Y. G. *Contemporary Chem. Ind.*, **2001**, 30(4), 210.
- <sup>4</sup> Ou, Y. *Petrochem. Ind. Technol.*, **2006**, 3, 9.
- <sup>5</sup> Feng, G. L. *West Leather*, **2012**, 8, 22.
- <sup>6</sup> Sheng, X., Hu, Y. Y., Zhang, L., Sun, H., Zheng, P., Tao, F. R., Yang, Y. Y. and Hang, J. *Chin. J. Anal. Chem.*, **2009**, 12, 1765.
- <sup>7</sup> Wang, X. C. and Yao, C. P. *Specialty Petrochem.*, **2003**, 2, 26.
- <sup>8</sup> Xiao, X. J., Zhang, F. Q. and Wang, Q. X. *China Cotton Process.*, **2008**, 6, 32.
- <sup>9</sup> Mao, Q. L., Wu, S. G. and Zhang, H. C. *Ana. Chem.*, **1995**, 23(6), 648.

Received: 29.09.2012.  
Accepted: 02.10.2012.



# DETERMINATION OF THE SOLUBILIZING CHARACTER OF 1-METHOXYETHYL-1-METHYLPYRROLIDIUM TRIS(PENTAFLUOROETHYL)TRIFLUOROPHOSPHATE BASED ON THE ABRAHAM SOLVATION PARAMETER MODEL

**Pamela Twu<sup>[a]</sup>, Jared L. Anderson<sup>[a]</sup>, Timothy W. Stephens<sup>[b]</sup>, William E. Acree, Jr.<sup>[b]\*</sup>, and  
Michael H. Abraham<sup>[c]</sup>**

**Keywords:** chromatographic retention factors, partition coefficients, linear free energy relationships, ionic liquids

---

Chromatographic retention data were measured for a chemically diverse set of organic solutes on an anhydrous 1-methoxyethyl-1-methylpyrrolidinium tris(pentafluoroethyl)trifluorophosphate, ([MeoeMPip]<sup>+</sup>[FAP]<sup>-</sup>), stationary phase at both 323 K and 353 K. The experimental retention factors were combined with previously published thermodynamic data and gas-to-water partition coefficient data to yield gas-to-anhydrous ionic liquid (IL) and water-to-anhydrous IL partition coefficients. The three sets of partition coefficient data were analyzed in accordance with the Abraham model. The Abraham model correlations that were determined in the present study describe the observed gas-to-([MeoeMPip]<sup>+</sup>[FAP]<sup>-</sup>) (log *K*) and water-to-([MeoeMPip]<sup>+</sup>[FAP]<sup>-</sup>) (log *P*) partition coefficient data to within average standard deviations of approximately 0.13 and 0.16 log units, respectively.

---

\* Corresponding Author  
Fax: 1-940-565-4318  
E-Mail: Bill.Acree@unt.edu

[a] University of Toledo, United States  
[b] University of North Texas, United States  
[c] University College London, United Kingdom

## 1. Introduction

Ionic liquids (ILs) have garnered considerable attention in recent years as potential “green solvent” replacements for the more traditional molecular organic solvents in applications involving chemical syntheses and chemical separations. Most (if not all) of the classic synthetic methods have been performed in ILs. Published studies have reported that much higher isolated product yields can be obtained in ILs with reduced reactions.<sup>1-4</sup> For select chemical reactions the IL may serve as both the reaction solvent media and catalyst, and the fact that many ionic liquids are immiscible with water and nonpolar organic solvents affords a convenient extraction method for separating the desired product(s) from any unreacted starting material(s). Ionic liquid have also been utilized as stationary phases in gas-liquid chromatography (glc)<sup>5-7</sup> and high-performance liquid chromatography (hplc),<sup>8,9</sup> and as sorbent materials for solid-phase microextractions.<sup>9,10</sup> The fore-mentioned applications are facilitated by the ionic liquid’s unique physical and solubilizing properties, which are determined largely by the specific cation-anion pair combination. The large number of known (and possible) combinations provides a large list of ILs having different viscosity, thermal stability, polarity, water immiscibility and solubilizing characteristics. At present more than 500 different ionic liquids are known.

The solvation parameter model, developed by Abraham and coworkers<sup>11,12</sup> has been successfully employed to evaluate the solubilizing properties of a large number of traditional organic solvents,<sup>13-18</sup> and several classes of ILs containing 1,3-dialkylimidazolium, 1,1-dialkylpyrrolidinium, N-alkylpyridinium and tetraalkylammonium cations with both ionic and organic anions.<sup>19-34</sup> The solvation parameter model is based on two linear free energy relationships (LFERs), the first mathematical relationship governs solute transfer between two condensed phases

$$\log P = c_p + e_p \cdot \mathbf{E} + s_p \cdot \mathbf{S} + a_p \cdot \mathbf{A} + b_p \cdot \mathbf{B} + v_p \cdot \mathbf{V} \quad (1)$$

while the second relationship describes solute transfer from the gas phase to a condensed phase

$$\log K = c_k + e_k \cdot \mathbf{E} + s_k \cdot \mathbf{S} + a_k \cdot \mathbf{A} + b_k \cdot \mathbf{B} + l_k \cdot \mathbf{L} \quad (2)$$

The two dependent solute properties, *P* and *K*, refer to the condensed phase-to-condensed phase partition coefficient (often water-to-organic solvent partition coefficient) and gas-to-condensed phase partition coefficient of the solute, respectively. Mathematical equations describing the respective standard Gibbs energies of transfer,  $\Delta G_{\text{water-to-organic solvent}}$  and  $\Delta G_{\text{gas-to-organic solvent}}$  are obtained by multiplying log *K* and log *P* by  $-2.303 RT$ :

$$\begin{aligned} \Delta G_{\text{water-to-organic solvent}} &= -2.303 RT \log P \\ &= -2.303 RT (c_p + e_p \cdot \mathbf{E} + s_p \cdot \mathbf{S} + a_p \cdot \mathbf{A} + b_p \cdot \mathbf{B} + v_p \cdot \mathbf{V}) \quad (3) \end{aligned}$$

$$\begin{aligned} \Delta G_{\text{gas-to-organic solvent}} &= -2.303 RT \log K \\ &= -2.303 RT (c_k + e_k \cdot \mathbf{E} + s_k \cdot \mathbf{S} + a_k \cdot \mathbf{A} + b_k \cdot \mathbf{B} + l_k \cdot \mathbf{L}) \quad (4) \end{aligned}$$

For ionic liquid solvents, Sprunger *et al.*<sup>30,35-37</sup> further modified the basic solvation model to include ion-specific equation coefficients:

$$\log P = c_{p,\text{cation}} + c_{p,\text{anion}} + (e_{p,\text{cation}} + e_{p,\text{anion}}) \mathbf{E} \\ + (s_{p,\text{cation}} + s_{p,\text{anion}}) \mathbf{S} + (a_{p,\text{cation}} + a_{p,\text{anion}}) \mathbf{A} \\ + (b_{p,\text{cation}} + b_{p,\text{anion}}) \mathbf{B} + (v_{p,\text{cation}} + v_{p,\text{anion}}) \mathbf{V} \quad (5)$$

$$\log K = c_{k,\text{cation}} + c_{k,\text{anion}} + (e_{k,\text{cation}} + e_{k,\text{anion}}) \mathbf{E} \\ + (s_{k,\text{cation}} + s_{k,\text{anion}}) \mathbf{S} + (a_{k,\text{cation}} + a_{k,\text{anion}}) \mathbf{A} \\ + (b_{k,\text{cation}} + b_{k,\text{anion}}) \mathbf{B} + (l_{k,\text{cation}} + l_{k,\text{anion}}) \mathbf{L} \quad (6)$$

Once calculated, the ion-specific equation coefficients can be summed to enable one to estimate solute partitioning behavior into a given IL as we will later illustrate. Thus far determined IL-specific equation coefficients have been determined for 30 different ILs (Eqns. 1 and 2), and 14 anion-specific coefficients and 21 cation-specific (Eqns. 5 and 6), based on experimentally measured infinite dilution activity coefficient data, gas chromatographic retention factors and solubilities of solutes dissolved in anhydrous IL solvents.<sup>19-37</sup> The fore-mentioned properties are thermodynamically related to the solute's Gibbs energies of transfer, gas-to-anhydrous IL and water-to-anhydrous IL partition coefficients. The water-to-anhydrous IL correlations describe "hypothetical" partitions, or more specifically a thermodynamic transfer process, in which the partition coefficient is calculated as the molar solubility ratio for the solute dissolved in both water and the anhydrous IL.

Each term on the right-hand side of Eqns. 1-6 represents a different type of solute-solvent interaction believed to be present in the solution. The interactions are determined by the polarity and hydrogen-bonding characteristics of the respective solute and solvent molecules. The uppercase variables (**E**, **S**, **A**, **B**, **V** and **L**) are solute-specific descriptors that have been determined for more than 5,000 different organic compounds and inorganic gases. The solute descriptors are defined as follows: **E** denotes the solute excess molar refraction in units of cm<sup>3</sup> mol<sup>-1</sup>/10 computed from the solute's refractive index; **S** corresponds to a combined dipolarity/polarizability descriptor; **A** and **B** describe the total hydrogen-bond acidity and basicity of the solute molecule, respectively; **V** is the McGowan characteristic molecular volume in units of cm<sup>3</sup> mol<sup>-1</sup>/100 and **L** is the logarithm of the gas-to-hexadecane partition coefficient measured at 298 K.

The set of six solvent/system coefficients in Eqns. 1-6 ( $c_p$ ,  $e_p$ ,  $s_p$ ,  $a_p$ ,  $b_p$ ,  $v_p$ ,  $c_k$ ,  $e_k$ ,  $s_k$ ,  $a_k$ ,  $b_k$  and  $l_k$ ) characterize the given transfer process, and when multiplied by the respective solute descriptor quantify the strength of each type of solute-condensed phase interaction. Consequently, the equation coefficients are not merely adjustable curve-fitting parameters, but rather encode chemical knowledge concerning the properties of the specific condensed phase being described. These properties are defined as follows:  $e$  is a measure of the condensed phase interactions with the non-bonding and  $\pi$ -electrons of the solute molecule;  $s$  describes the dipolarity/polarizability of the condensed phase;  $a$  represents the condensed phase's hydrogen bond basicity (which is the complimentary property to solute's hydrogen bond acidity) and  $b$  is the condensed phase's hydrogen bond acidity (which is the complimentary property

to solute's hydrogen bond basicity). The  $l$  and  $v$  coefficients in Eqns. 1-6 reflect the general dispersion forces that facilitate solubility of a dissolved solute and the condensed phase-condensed phase interactions that oppose the solubilization process. In the case of solute transfer between water and an ionic liquid solvent (Eqns. 1, 3 and 5), the equation coefficients refer to differences in the properties of the aqueous and IL condensed phases.

In the present study, we report gas-liquid chromatographic retention factor data for a wide range of organic solutes on 1-methoxyethyl-1-methylpiperidinium *tris*(pentafluoroethyl)trifluorophosphate, ([MeoeMPip]<sup>+</sup>[FAP]<sup>-</sup>), stationary phases at 323 K and 353 K. See Figure 1 for the molecular structure of the ionic liquid solvent. Results of the chromatographic measurements, combined with published gas-to-liquid partition coefficient data for volatile solutes dissolved in ([MeoeMPip]<sup>+</sup>[FAP]<sup>-</sup>)<sup>38</sup> were used to derive Abraham model  $\log K$  and  $\log P$  correlations at 298 K and 323 K. We note that Marciniak and Wlazlo<sup>38</sup> previously reported on Abraham model correlations for ([MeoeMPip]<sup>+</sup>[FAP]<sup>-</sup>) at 318, 328, 338, 348, 358 and 368 K based on 62 experimental data points. The datasets used in deriving the published correlations did not include the more acidic phenolic and carboxylic acid solutes (solutes with large **A** values) and the lesser volatile organic compounds considered in the present study. As a result the expanse of predictive chemical space encompassed by the published Abraham model correlations is significantly less than that achieved by the correlations derived here. The predictive area of chemical space is important in that one should not use the derived equations to estimate  $\log P$  and  $\log K$  values for compounds whose solute descriptors fall outside of the range of solute descriptors used in obtaining the predictive equations. Several of the IL-specific Abraham model correlations that have been reported in the published literature were based on datasets containing only fairly volatile and nonacidic organic solutes. Correlation equations derived from such data sets do need to be updated as experimental data for more diverse chemical solutes become available.

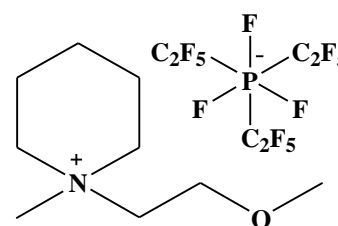


**Figure 1.** Molecular structure of 1-methoxy-ethyl-1-methylpiperidinium *tris*(pentafluoroethyl)trifluorophosphate.

## 2. Experimental Methods and Partition Coefficient Datasets

The sample of 1-methoxyethyl-1-methylpiperidinium *tris*(pentafluoroethyl)trifluorophosphate examined in this study was kindly donated as a gift from Merck KGaA (Darmstadt, Germany). The IL stationary phase was coated onto untreated fused silica capillary columns (5 m x 0.25 mm) obtained from Supelco (Bellefonte, PA). The IL coating solutions were prepared in dichloromethane using a 0.45% (w/v) concentration of [MeoeMPip]<sup>+</sup>[FAP]<sup>-</sup>.

Forty-four (44) probe molecules were selected for the characterization of the [MeoeMPip]<sup>+</sup>[FAP]<sup>-</sup> stationary phase. The names of the solutes, along with the chemical suppliers and chemical purities, are given in Table 1. All solute molecules were used as received. The presence of trace impurities in these probes should in no way affect the results because the main chromatographic peak can be easily distinguished from any impurity peak by its much greater intensity.

**Table 1.** List of organic solutes, chemical suppliers, and chemical purities

Solute	Supplier <sup>a</sup>	Purity
Acetic acid	Supelco	99.7%
Acetophenone	Sigma-Aldrich	99%
Aniline	Sigma-Aldrich	99.5%
Benzaldehyde	Sigma-Aldrich	99+%
Benzene	Sigma-Aldrich	99.8%
Benzonitrile	Sigma-Aldrich	99%
Benzyl alcohol	Sigma-Aldrich	99%
1-Bromohexane	Sigma-Aldrich	98%
1-Bromooctane	Sigma-Aldrich	99%
Butyraldehyde	Acros Organics	99%
1-Butanol	Fisher Scientific	99.9%
2-Chloroaniline	Sigma-Aldrich	98%
1-Chlorobutane	Sigma-Aldrich	99%
1-Chlorohexane	Sigma-Aldrich	99%
1-Chlorooctane	Sigma-Aldrich	99%
<i>p</i> -Cresol	Fluka	99%
Cyclohexanol	J.T. Baker	99%
Cyclohexanone	Sigma-Aldrich	99.8%
1,2-Dichlorobenzene	Sigma-Aldrich	99%
1,4-Dioxane	Sigma-Aldrich	99.8%
N,N-Dimethylformamide	Fisher Scientific	99.9%
Ethyl acetate	Fisher Scientific	99.9%
Ethylbenzene	Eastman Kodak Co	95+%
1-Iodobutane	Sigma-Aldrich	99%
Methyl caproate	Supelco	98%
Naphthalene	Supelco	98%
Nitrobenzene	Sigma-Aldrich	99+%
2-Nitrophenol	Acros Organics	99%
1-Nitropropane	Sigma-Aldrich	99%
1-Octanol	Sigma-Aldrich	99+%
Octylaldehyde	Sigma-Aldrich	99%
1-Pentanol	Sigma-Aldrich	99+%
2-Pentanone	Sigma-Aldrich	99+%
Phenetole	Sigma-Aldrich	99%
Phenol	Sigma-Aldrich	99+%
Propionitrile	Sigma-Aldrich	99%
Pyridine	Sigma-Aldrich	99.9%
Toluene	Fisher Scientific	99.80%
<i>m</i> -Xylene	Fluka	99.5%
<i>o</i> -Xylene	Fluka	99.5%
<i>p</i> -Xylene	Fluka	99.5%
Propanoic acid	Supelco	99%
1-Decanol	Sigma-Aldrich	99+%
2-Propanol	Fisher Scientific	99.6%

<sup>a</sup> Fluka (Steinheim, Germany); Eastman Kodak Company (Rochester, NY, USA); Supelco (Bellefonte, PA, USA); Acros Organics (Morris Plains, NJ, USA); J.T. Baker (Phillipsburg, NJ, USA); Sigma-Aldrich (St. Louis, MO, USA); and Fisher Scientific (Pittsburgh, PA, USA).

Chromatographic retention factors,  $k$ , were determined on a [MeoeMPip]<sup>+</sup>[FAP]<sup>-</sup> stationary phase at 323 K and 353 K as part of the present study. The percent relative standard deviation (% RSD) in experimental retention times for all solutes included in this study was less than 1%. The stationary phase's integrity during the duration of the experimental measurements was established by periodically monitoring the retention factor and efficiency of naphthalene separation. The experimental  $\log k$  values are tabulated in the second and third columns of Table 2. The extrapolated 298 K  $\log k$  values obtained through a  $\log k$  versus  $1/T$  linear plot of the measured data at 323 K and 353 K are given in the table's last column.

The thermodynamic gas-to-IL partition coefficient,  $K$ , can be computed from isothermal chromatographic measurements through  $K = V_N/V_L$ , where  $V_N$  is the volume of the carrier gas required to elute the solute, and  $V_L$  is the volume of liquid present as the stationary phase.<sup>39</sup> The retention factor,  $k$ , is defined as<sup>39</sup>  $k = (t_r - t_m)/t_m$  where  $t_r$  is the retention time of a solute and  $t_m$  is the "void" retention time for an unretained solute. Since  $t_r - t_m$ , the corrected retention time, is proportional to  $V_N$ , the corrected elution volume, it follows that gas-to-liquid partition coefficients and retention factors are interrelated,

$$K = P^* \cdot k \quad \text{or} \quad \log K = \log P^* + \log k \quad (7)$$

The proportionality constant,  $P^*$ , is the phase ratio and depends only upon the chromatographic conditions. The value of  $P^*$  should remain essentially constant for a given column during the time the experimental measurements are performed.

Thermodynamic gas-to-IL partition coefficients are required to calculate the proportionality constants needed in Eqn. 8 for converting the measured  $\log k$  data in Table 2 to  $\log K$  values. Marciniak and Wlazlo<sup>38</sup> reported infinite dilution activity coefficients and gas-to-liquid partition coefficients of 62 solutes dissolved in [MeoeMPip]<sup>+</sup>[FAP]<sup>-</sup> in the 318 to 368 K temperature range. Uncertainties in the measured  $K$  and  $\gamma_{\text{solute}}^\infty$  values were reported to be on the order of 2 to 3%. The published experimental data were extrapolated to 298 K and 323 K by assuming a linear  $\ln K$  versus  $1/T$  relationship. A linear extrapolation should be valid as the measurements were performed not too far removed from the desired temperatures (less than 20 K in most instances). The  $\log P$  values for partition from water to the anhydrous IL can be calculated via Eqn. 8

$$\log P = \log K - \log K_w \quad (8)$$

The conversion of  $\log K$  data to  $\log P$  requires a prior knowledge of the solute's gas phase partition coefficient into water,  $K_w$ , which is available for most of the solutes being studied. As noted above, water-to-anhydrous IL partition coefficients (more formally called Gibbs energy of solute transfer when multiplied by  $-2.303 RT$ ) calculated through Eqn. 8 refer to a hypothetical partitioning process involving solute transfer from water to the anhydrous IL.  $\log P$  values calculated in this fashion are still useful because the predicted  $\log P$  values can be used to estimate the solute's infinite dilution activity coefficient in the IL.

The proportionality constants needed in Eqn. 7;  $\log P^* = 2.555$  (298 K) and  $\log P^* = 2.498$  (323 K) for [MeoeMPip]<sup>+</sup>[FAP]<sup>-</sup> were the calculated average differences between the measured  $\log k$  and  $\log K$  values for

**Table 2.** Chromatographic retention factor data for organic solutes on 1-methoxyethyl-1-methylpiperidinium tris(pentafluoroethyl)-trifluorophosphate, ([MeoeMPip]<sup>+</sup>[FAP]<sup>-</sup>), stationary phase at 298, 323, and 353 K

Solute	log k (323 K)	log k (353 K)	log k (298 K)
Acetic acid	0.446	-0.096	0.981
Acetophenone	2.172	1.466	2.869
Aniline	2.187	1.462	2.902
Benzaldehyde	1.662	1.027	2.289
Benzene	0.037	-0.405	0.474
Benzonitrile	1.810	1.177	2.435
Benzyl alcohol	2.150	1.421	2.870
1-Bromooctane	0.983	0.370	1.589
1-Butanol	0.143	-0.341	0.622
Butyraldehyde	0.087	-0.352	0.520
2-Chloroaniline	2.284	1.558	3.001
1-Chlorobutane	-0.495		
1-Chlorohexane	0.129	-0.354	0.606
1-Chlorooctane	0.736	0.155	1.309
<i>p</i> -Cresol	2.173	1.420	2.915
Cyclohexanol	0.922	0.343	1.493
Cyclohexanone	1.384	0.804	1.957
1,2-Dichlorobenzene	1.111	0.540	1.675
N,N-Dimethylformamide	1.925	1.288	2.554
1,4-Dioxane	0.578	0.059	1.090
Ethyl acetate	0.142	-0.334	0.610
Ethylbenzene	0.649	0.105	1.186
1-Iodobutane	-0.028	-0.452	0.392
Methyl Caproate	1.019	0.404	1.626
Naphthalene	2.288	1.580	2.988
Nitrobenzene	2.040	1.379	2.693
1-Nitropropane	0.939	0.409	1.461
1-Octanol	1.372	0.690	2.045
Octylaldehyde	1.305	0.667	1.935
1-Pentanol	0.462	-0.065	0.981
2-Pentanone	0.587	0.080	1.087
Phenetole	1.394	0.756	2.023
Phenol	1.855	1.161	2.539
Propionitrile	0.537	0.082	0.986
Pyridine	0.813	0.300	1.320
Pyrrole	1.329	0.722	1.929
Toluene	0.388	-0.103	0.873
<i>m</i> -Xylene	0.731	0.179	1.276
<i>o</i> -Xylene	0.836	0.277	1.387
<i>p</i> -Xylene	0.705	0.154	1.248
2-Propanol	-0.385		
2-Nitrophenol	1.960	1.291	2.621
1-Bromohexane	0.364	-0.128	0.849
Propanoic acid	0.731	0.133	1.321
1-Decanol	1.970	1.188	2.742

the 12 common compounds (i.e., benzene, 1-butanol, butyraldehyde, ethyl acetate, ethylbenzene, 1-nitropropane, 2-pentanone, pyridine, toluene, *m*-xylene, *o*-xylene and *p*-xylene) in the IL's data set that had been studied by us and by Marciniak and Wlazlo.<sup>38</sup> The calculated  $\log K$  and  $\log P$  values are compiled in Table 3 for solutes dissolved in [MeoeMPip]<sup>+</sup>[FAP]<sup>-</sup>.  $\log P$  values are tabulated only for

298 K as we do not have experimental values for the solutes' gas-to-water partition coefficients,  $\log K_w$ , at 323 K. The  $\log K_w$  values that we have compiled to date pertain to gas to water partitioning at 298 K<sup>40</sup> and 310 K,<sup>41</sup> or for gas to physiological saline partitioning at 310 K.<sup>41</sup> For the convenience of the reader, we have compiled the numerical values of solute descriptors for the 90 organic compounds considered in the present study in Table 4. The solute descriptors are of experimental origin, and were retrieved from the Abraham database. The numerical values were deduced from experimental solubility data, gas-liquid and high-performance liquid chromatographic retention factor measurements and water-to-solvent partition determinations as discussed by Abraham and coworkers<sup>42-44</sup> in several published papers.

### 3. Results and Discussion

We have tabulated in Table 3 the experimental  $\log K$  values and  $\log P$  values for a chemically diverse set of 90 organic compounds in [MeoeMPip]<sup>+</sup>[FAP]<sup>-</sup>. The solutes span a large range of molecular size and shape, polarity and hydrogen-bonding characteristics. Preliminary analysis of the experimental data in Table 3 in accordance with Eqns. 1 and 2 of the Abraham general solvation parameter model revealed that the  $e_k$  equation coefficient ( $e_k = 0.008 \pm 0.092$  and  $0.040 \pm 0.069$ ) was negligible in both the  $\log K$  (298 K) and  $\log K$  (323 K) correlation. The  $e_k \cdot E$  term was consequently removed from the 298 K and 323 K  $\log K$  correlations, and the regression analyses were rerun to yield the following three LFERs:

$$\begin{aligned} \log K (298 \text{ K}) = & -0.177 (0.061) + 2.311(0.056) \text{ S} \\ & + 1.249(0.091) \text{ A} + 0.542(0.090) \text{ B} \\ & + 0.655(0.017) \text{ L} \end{aligned} \quad (8)$$

(N = 103, SD = 0.137, R<sup>2</sup> = 0.984, F = 1534)

$$\begin{aligned} \log K (323 \text{ K}) = & -0.298(0.050) + 2.126(0.047) \text{ S} \\ & + 1.056(0.076) \text{ A} + 0.447(0.075) \text{ B} \\ & + 0.567(0.014) \text{ L} \end{aligned} \quad (9)$$

(N = 105, SD = 0.116, R<sup>2</sup> = 0.986, F = 1747)

$$\begin{aligned} \log P (298 \text{ K}) = & 0.114(0.091) + 0.260(0.091) \text{ E} \\ & + 0.391(0.103) \text{ S} - 2.448(0.114) \text{ A} \\ & - 4.245(0.128) \text{ B} + 3.281(0.079) \text{ V} \end{aligned} \quad (10)$$

(N = 103, SD = 0.163, R<sup>2</sup> = 0.989, F = 1755)

where the standard errors in the calculated equation coefficients are given in parentheses. The statistical information associated with each correlation includes the number of experimental data points (N), the standard deviation (SD), the squared correlation coefficient (R<sup>2</sup>) and the Fisher F-statistic (F). The number of data points used in the regression analyses is larger than the number of solutes studied because the thirteen solutes needed in the  $\log P^*$  computation appear twice – first in top thermodynamic dataset and then later in the chromatographic retention factor dataset.

**Table 3.** Logarithm of the gas-to-anhydrous IL partition coefficient, log *K*, and logarithm of the water-to-anhydrous IL partition coefficient, log *P*, for organic solutes dissolved in [MeoeMPip]<sup>+</sup>[FAP]<sup>-</sup> at 298 K and 323 K

Solute	log <i>K</i> (298 K)	log <i>K</i> (323 K)	log <i>P</i> (298 K)
<i>Based on Thermodynamic Data</i>			
Pentane	1.118	0.832	2.818
Hexane	1.488	1.142	3.308
3-Methylpentane	1.449	1.120	3.289
2,2-Dimethylbutane	1.274	0.978	3.114
Heptane	1.844	1.450	3.804
Octane	2.198	1.753	4.308
2,2,4-Trimethylpentane	1.859	1.476	3.979
Nonane	2.559	2.055	4.709
Decane	2.914	2.355	5.234
Cyclopentane	1.508	1.194	2.388
Cyclohexane	1.837	1.486	2.737
Methylcyclohexane	2.051	1.661	3.301
Cycloheptane	2.349	1.925	2.929
Cyclooctane	2.784	2.309	3.554
1-Pentene	1.354	1.042	2.584
1-Hexene	1.727	1.357	2.887
Cyclohexene	2.151	1.752	2.421
1-Heptene	2.084	1.660	3.304
1-Octene	2.445	1.963	3.855
1-Decene	3.122	2.551	4.762
1-Pentyne	1.885	1.504	1.895
1-Hexyne	2.242	1.809	2.542
1-Heptyne	2.606	2.115	3.046
1-Octyne	2.943	2.412	3.463
Benzene	3.036	2.547	2.406
Toluene	3.432	2.888	2.782
Ethylbenzene	3.736	3.148	3.156
<i>o</i> -Xylene	3.947	3.337	3.287
<i>m</i> -Xylene	3.840	3.235	3.230
<i>p</i> -Xylene	3.804	3.201	3.214
Styrene	4.142	3.508	3.192
$\alpha$ -Methylstyrene	4.361	3.684	3.401
Methanol	2.197	1.808	-1.543
Ethanol	2.436	2.006	-1.234
1-Propanol	2.790	2.303	-0.770
2-Propanol	2.563	2.101	-0.917
1-Butanol	3.192	2.636	-0.268
2-Butanol	2.915	2.392	-0.475
2-Methyl-1-propanol	2.986	2.473	-0.314
<i>tert</i> -Butanol	2.673	2.177	-0.607
Thiophene	3.083	2.593	2.043
Tetrahydrofuran	2.917	2.447	0.367
1,4-Dioxane	3.643	3.078	-0.067
Methyl <i>tert</i> -butyl ether	2.244	1.817	0.624
Ethyl <i>tert</i> -butyl ether	2.151	1.722	0.881
Methyl <i>tert</i> -amyl ether	2.589	2.115	1.119
Diethyl ether	1.900	1.514	0.730
Dipropyl ether	2.408	1.947	1.518
Diisopropyl ether	2.091	1.663	1.041
Dibutyl ether	3.063	2.509	2.373
Acetone	3.037	2.572	0.247
2-Pentanone	3.644	3.089	1.064

**Table 3.** (cont.)

Solute	log <i>K</i> (298 K)	log <i>K</i> (323 K)	log <i>P</i> (298 K)
<i>Based on Thermodynamic Data</i>			
3-Pentanone	3.639	3.080	1.139
Methyl acetate	2.886	2.414	0.586
Ethyl acetate	3.154	2.639	0.994
Methyl propanoate	3.203	2.678	1.053
Methyl butanoate	3.491	2.927	1.411
Butyraldehyde	3.067	2.585	0.737
Acetonitrile	3.314	2.849	0.464
Pyridine	3.857	3.284	0.417
1-Nitropropane	4.021	3.446	1.571
<i>Based on Chromatographic Retention Factor Data</i>			
Acetic acid	3.536	2.944	-1.374
Acetophenone	5.424	4.670	2.154
Aniline	5.457	4.685	1.375
Benzaldehyde	4.844	4.160	1.894
Benzene	3.029	2.535	2.399
Benzonitrile	4.990	4.308	1.900
Benzyl alcohol	5.425	4.648	0.565
1-Bromooctane	4.144	3.481	4.524
Butyraldehyde	3.075	2.585	0.745
1-Butanol	3.177	2.641	-0.283
2-Chloroaniline	5.556	4.782	1.956
1-Chlorobutane		2.003	
1-Chlorohexane	3.161	2.627	3.161
1-Chlorooctane	3.864	3.234	4.054
<i>p</i> -Cresol	5.470	4.671	0.970
Cyclohexanol	4.048	3.420	0.038
Cyclohexanone	4.512	3.882	0.912
1,2-Dichlorobenzene	4.230	3.609	3.330
1,4-Dioxane	3.645	3.076	-0.065
<i>N,N</i> -Dimethylformamide	5.109	4.423	-0.621
Ethyl acetate	3.165	2.640	1.005
Ethyl benzene	3.741	3.147	3.161
1-Iodobutane	2.947	2.470	2.767
Methyl caproate	4.181	3.517	2.351
Naphthalene	5.543	4.786	3.813
Nitrobenzene	5.248	4.538	2.228
2-Nitrophenol	5.176	4.458	1.816
1-Nitropropane	4.016	3.437	1.566
1-Octanol	4.600	3.870	1.600
Octylaldehyde	4.490	3.803	2.810
1-Pentanol	3.536	2.960	0.186
2-Pentanone	3.642	3.085	1.062
Phenetole	4.578	3.892	2.948
Phenol	5.094	4.353	0.244
2-Propanol		2.113	
Propionitrile	3.541	3.035	0.721
Pyridine	3.875	3.311	0.435
Toluene	3.428	2.886	2.778
<i>m</i> -Xylene	3.831	3.229	3.221
<i>o</i> -Xylene	3.942	3.334	3.282
<i>p</i> -Xylene	3.803	3.203	3.213
1-Bromohexane	3.404	2.862	3.534
Propanoic acid	3.876	3.229	-0.864
1-Decanol	5.297	4.468	2.627

**Table 4.** Abraham model solute descriptors of the organic compounds considered in the present study

Solute	E	S	A	B	L	V
Pentane	0.000	0.000	0.000	0.000	2.162	0.8131
Hexane	0.000	0.000	0.000	0.000	2.668	0.9540
3-Methylpentane	0.000	0.000	0.000	0.000	2.581	0.9540
2,2-Dimethylbutane	0.000	0.000	0.000	0.000	2.352	0.9540
Heptane	0.000	0.000	0.000	0.000	3.173	1.0949
Octane	0.000	0.000	0.000	0.000	3.677	1.2358
2,2,4-Trimethylpentane	0.000	0.000	0.000	0.000	3.106	1.2358
Nonane	0.000	0.000	0.000	0.000	4.182	1.3767
Decane	0.000	0.000	0.000	0.000	4.686	1.5176
Cyclopentane	0.263	0.100	0.000	0.000	2.477	0.7045
Cyclohexane	0.305	0.100	0.000	0.000	2.964	0.8454
Methylcyclohexane	0.244	0.060	0.000	0.000	3.319	0.9863
Cycloheptane	0.350	0.100	0.000	0.000	3.704	0.9863
Cyclooctane	0.413	0.100	0.000	0.000	4.329	1.1272
1-Pentene	0.093	0.080	0.000	0.070	2.047	0.7701
1-Hexene	0.078	0.080	0.000	0.070	2.572	0.9110
Cyclohexene	0.395	0.280	0.000	0.090	2.952	0.8204
1-Heptene	0.092	0.080	0.000	0.070	3.063	1.0519
1-Octene	0.094	0.080	0.000	0.070	3.568	1.1928
1-Decene	0.093	0.080	0.000	0.070	4.554	1.4746
1-Pentyne	0.172	0.230	0.120	0.120	2.010	0.7271
1-Hexyne	0.166	0.220	0.100	0.120	2.510	0.8680
1-Heptyne	0.160	0.230	0.120	0.100	3.000	1.0089
1-Octyne	0.155	0.220	0.090	0.100	3.521	1.1498
Benzene	0.610	0.520	0.000	0.140	2.786	0.7164
Toluene	0.601	0.520	0.000	0.140	3.325	0.8573
Ethylbenzene	0.613	0.510	0.000	0.150	3.778	0.9982
<i>o</i> -Xylene	0.663	0.560	0.000	0.160	3.939	0.9982
<i>m</i> -Xylene	0.623	0.520	0.000	0.160	3.839	0.9982
<i>p</i> -Xylene	0.613	0.520	0.000	0.160	3.839	0.9982
Styrene	0.849	0.650	0.000	0.160	3.908	0.9550
$\alpha$ -Methylstyrene	0.851	0.640	0.000	0.190	4.290	1.0960
Methanol	0.278	0.440	0.430	0.470	0.970	0.3082
Ethanol	0.246	0.420	0.370	0.480	1.485	0.4491
1-Propanol	0.236	0.420	0.370	0.480	2.031	0.5900
2-Propanol	0.212	0.360	0.330	0.560	1.764	0.5900
1-Butanol	0.224	0.420	0.370	0.480	2.601	0.7310
2-Butanol	0.217	0.360	0.330	0.560	2.338	0.7310
2-Methyl-1-propanol	0.217	0.390	0.370	0.480	2.413	0.7310
<i>tert</i> -Butanol	0.180	0.300	0.310	0.600	1.963	0.7310
Thiophene	0.687	0.570	0.000	0.150	2.819	0.6411
Tetrahydrofuran	0.289	0.520	0.000	0.480	2.636	0.6223
1,4-Dioxane	0.329	0.750	0.000	0.640	2.892	0.6810
Methyl <i>tert</i> -butyl ether	0.024	0.220	0.000	0.550	2.372	0.8718
Ethyl <i>tert</i> -butyl ether	-0.020	0.160	0.000	0.600	2.720	1.0127
Methyl <i>tert</i> -amyl ether	0.050	0.210	0.000	0.600	2.916	1.0127
Diethyl ether	0.041	0.250	0.000	0.450	2.015	0.7309
Dipropyl ether	0.008	0.250	0.000	0.450	2.954	1.0127
Diisopropyl ether	-0.063	0.170	0.000	0.570	2.501	1.0127
Dibutyl ether	0.000	0.250	0.000	0.450	3.924	1.2945
Acetone	0.179	0.700	0.040	0.490	1.696	0.5470
2-Pentanone	0.143	0.680	0.000	0.510	2.755	0.8288
3-Pentanone	0.154	0.660	0.000	0.510	2.811	0.8288
Methyl acetate	0.142	0.640	0.000	0.450	1.911	0.6057
Ethyl acetate	0.106	0.620	0.000	0.450	2.314	0.7466
Methyl propanoate	0.128	0.600	0.000	0.450	2.431	0.7470
Methyl butanoate	0.106	0.600	0.000	0.450	2.943	0.8880
Butyraldehyde	0.187	0.650	0.000	0.450	2.270	0.6880
Acetonitrile	0.237	0.900	0.070	0.320	1.739	0.4040
Pyridine	0.631	0.840	0.000	0.520	3.022	0.6753

Table 4. (cont.)

Solute	E	S	A	B	L	V
1-Nitropropane	0.242	0.950	0.000	0.310	2.894	0.7055
Acetic acid	0.265	0.640	0.620	0.440	1.816	0.4648
Acetophenone	0.818	1.010	0.000	0.480	4.501	1.0139
Aniline	0.955	0.960	0.260	0.410	3.934	0.8162
Benzaldehyde	0.820	1.000	0.000	0.390	4.008	0.8730
Benzonitrile	0.742	1.110	0.000	0.330	4.039	0.8711
Benzyl alcohol	0.803	0.870	0.330	0.560	4.221	0.9160
1-Bromooctane	0.339	0.400	0.000	0.120	5.143	1.4108
2-Chloroaniline	1.033	0.920	0.250	0.310	4.674	0.9390
1-Chlorobutane	0.210	0.400	0.000	0.100	2.722	0.7946
1-Chlorohexane	0.201	0.390	0.000	0.090	3.708	1.0764
1-Chlorooctane	0.191	0.400	0.000	0.090	4.708	1.3582
<i>p</i> -Cresol	0.820	0.870	0.570	0.310	4.312	0.9160
Cyclohexanol	0.460	0.540	0.320	0.570	3.758	0.9040
Cyclohexanone	0.403	0.860	0.000	0.560	3.792	0.8611
1,2-Dichlorobenzene	0.872	0.780	0.000	0.040	4.318	0.9612
N,N-Dimethylformamide	0.367	1.310	0.000	0.740	3.173	0.6468
1-Iodobutane	0.628	0.400	0.000	0.150	3.628	0.9304
Methyl caproate	0.080	0.600	0.000	0.450	3.874	1.1693
Naphthalene	1.340	0.920	0.000	0.200	5.161	1.0854
Nitrobenzene	0.871	1.110	0.000	0.280	4.557	0.8906
2-Nitrophenol	1.015	1.050	0.050	0.370	4.760	0.9493
1-Octanol	0.199	0.420	0.370	0.480	4.619	1.2950
Octylaldehyde	0.160	0.650	0.000	0.450	4.380	1.2515
1-Pentanol	0.219	0.420	0.370	0.480	3.106	0.8718
2-Pentanone	0.143	0.680	0.000	0.510	2.755	0.8288
Phenetole	0.681	0.700	0.000	0.320	4.242	1.0569
Phenol	0.805	0.890	0.600	0.300	3.766	0.7751
Propionitrile	0.162	0.900	0.020	0.360	2.082	0.5450
1-Bromohexane	0.349	0.400	0.000	0.120	4.130	1.1290
Propionic acid	0.233	0.650	0.600	0.450	2.290	0.6057
1-Decanol	0.191	0.420	0.370	0.480	5.610	1.5763

All regression analyses were performed using SPSS Statistics (Version 20) software. The LFERs described by Eqns. 8 – 10 are statistically quite good with standard deviations of less than 0.165 log units. Figure 2 shows a plot of log *K* (298) values predicted from Eqn. 8 against experimental values covering a range of approximately 4.44 log units, from log *K* = 1.118 for pentane to log *K* = 5.556 for 2-chloronaphthalene. A comparison of the calculated versus experimental log *P* data is shown in Figure 2. As expected the standard deviation for the log *P* correlation is slightly larger than that of the log *K* correlations because the log *P* values contain the additional experimental uncertainty in the gas-to-water used in the log *K* to log *P* conversion.

The equation coefficients in Eqn. 9 can be compared to those reported by Marciniak and Wlazlo.<sup>38</sup> As noted above the authors determined log *K* correlations based on experimental gas-to-liquid partition coefficient data for 55 different compounds measured at temperatures of 318, 328, 338, 348, 358 and 368 K. While 323 K was not one of the temperatures studied by the authors, one should be able to reasonably assume that a log *K* correlation for 323 K should fall somewhere between the reported correlations

$$\log K (318 \text{ K}) = -0.386(0.067) - 0.004(0.082) \mathbf{E} \\ + 2.35(0.08) \mathbf{S} + 1.17(0.12) \mathbf{A} \\ + 0.391(0.084) \mathbf{B} + 0.607(0.020) \mathbf{L} \quad (11)$$

$$\log K (328 \text{ K}) = -0.409(0.062) + 0.005(0.076) \mathbf{E} \\ + 2.26(0.08) \mathbf{S} + 1.09(0.12) \mathbf{A} \\ + 0.354(0.079) \mathbf{B} + 0.569(0.019) \mathbf{L} \quad (12)$$

for 318 K and 328 K. Comparison of Eqns. 9, 11 and 12 shows that our calculated equation coefficients for the 323 log *K* correlation do fall in between those reported for the Marciniak and Wlazlo for 318 K and 328 K when the combined standard errors in the coefficients are taken into account. The slight difference between our coefficients and the arithmetic average of the coefficients of Eqns. 11 and 12 likely results from the more diverse set of solutes used in deriving Eqn. 9. Our dataset (see Table 3) has 105 data points and includes two carboxylic acid solutes (acetic acid and propanoic acid), two primary amine solutes (aniline and 2-chloroaniline), three phenolic compounds (phenol, 2-nitrophenol and *p*-cresol), several substituted aromatic benzene derivatives (nitrobenzene, benzonitrile, acetophenone, benzaldehyde, phenetole, 1,2-dichlorobenzene, benzyl alcohol), and

several halogenated alkanes (1-chlorobutane, 1-chlorohexane, 1-chlorooctane, 1-iodobutane, 1-bromohexane, 1-bromooctane) plus the solutes (and data) from the Marciniak and Wlazlo study.<sup>38</sup> We also note that Marciniak and Wlazlo did not report a log *K* correlation for 298 K, nor did the authors correlate the water-to-anhydrous ionic liquid transfer properties.

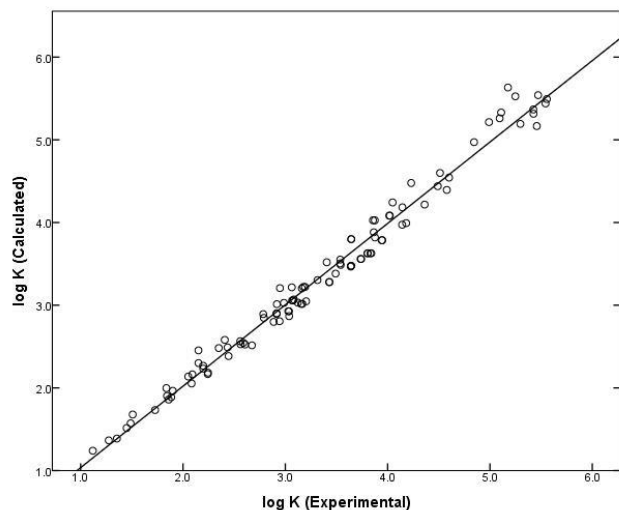


**Figure 2.** Comparison between experimental log *K* (298 K) data and predicted values based on Eqn. 8

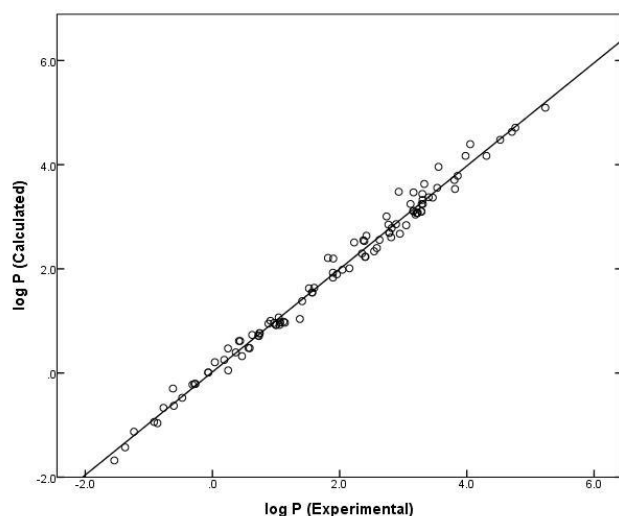


**Figure 3.** Comparison between experimental log *P* (298 K) data and predicted values based on Eqn. 10

One small change that has made in the present study concerns converting the measured log *K* value to log *P*. We are using a value of log *K<sub>w</sub>* = -0.77 for the logarithm of the gas-to-water partition coefficient of cyclooctane<sup>45</sup> in the log *K* to log *P* conversions, which is a departure from several earlier studies. Stephens et al.<sup>31</sup> observed that the value of log *K<sub>w</sub>* = -0.77 for cyclooctane led to slightly smaller standard deviations in the log *P* correlations of 1-butyl-1-methylpyrrolidinium tetracyanoborate and 1-butyl-1-methylpiperidinium bis(trifluoromethylsulfonyl)imide. The standard deviations in the derived correlations are slightly larger than the uncertainty in the measured data, which we estimate to be

on the order of approximately ± 0.07 to 0.10 log units. Our estimated uncertainty includes not only the uncertainties in the measured *K* data, but also the uncertainties involved in extrapolating the measured values to 298 K and in the calculated proportionality constant, *P*<sup>\*</sup>, needed to convert the chromatographic retention factors to gas-to-liquid partition coefficients.

Equations 8 – 10 can be utilized to estimate the infinite dilution activity coefficients and chromatographic retention factors of solutes dissolved in anhydrous [MeoeMPip]<sup>+</sup>[FAP]<sup>-</sup>. The predicted log *K* and log *P* values could be easily converted to  $\gamma_{\text{solute}}^{\infty}$  values through Eqns. 13 and 14

$$\log K = \log \left( \frac{RT}{\gamma_{\text{solute}}^{\infty} P_{\text{solute}}^{\circ} V_{\text{solvent}}} \right) \quad (13)$$

$$\log P + \log K_w = \log \left( \frac{RT}{\gamma_{\text{solute}}^{\infty} P_{\text{solute}}^{\circ} V_{\text{solvent}}} \right) \quad (14)$$

where  $P_{\text{solute}}^{\circ}$  is the vapor pressure of the solute at the system temperature (*T*),  $V_{\text{solvent}}$  is the molar volume of the IL solvent, and *R* is the universal gas constant. Infinite dilution activity coefficients play an important role in chemical separations in that the ratio of  $\gamma_{\text{solute}}^{\infty}$  values for two solutes is called the selectivity factor which measures the enhanced separation that one could get from solute interactions with the ionic liquid phase solvent. In the case of chromatographic retention factors, one will need to measure log *k* values for a few standard “calibration” solutes using the actual coated chromatographic column in order to obtain the phase ratio (*P*<sup>\*</sup> in Eqn. 7) needed to convert the predicted log *K* values to log *k* values.

In order to assess properly the predictive capabilities and limitations of Eqns. 8–10, we divided each of the three large data sets into training sets and test sets by allowing the SPSS software to randomly select half of the experimental data points. The selected data points became the training sets and the compounds that were left served as the test sets. Analysis of the experimental data in the two log *K* and single log *P* training sets gave

$$\begin{aligned} \log K (298) = & -0.120(0.088) + 2.260(0.076) \mathbf{S} \\ & + 1.242(0.107) \mathbf{A} + 0.556(0.123) \mathbf{B} \\ & + 0.644 (0.023) \mathbf{L} \end{aligned} \quad (15)$$

(*N* = 52, *SD* = 0.137, *R*<sup>2</sup> = 0.984, *F* = 704)

$$\begin{aligned} \log K (323) = & -0.326(0.073) + 2.115(0.078) \mathbf{S} \\ & + 1.179(0.169) \mathbf{A} + 0.425(0.128) \mathbf{B} \\ & + 0.574(0.021) \mathbf{L} \end{aligned} \quad (16)$$

(*N* = 53, *SD* = 0.119, *R*<sup>2</sup> = 0.985, *F* = 765)

$$\begin{aligned} \log P (298) = & 0.075(0.128) + 0.129(0.121) \mathbf{E} \\ & + 0.515(0.144) \mathbf{S} - 2.490(0.141) \mathbf{A} \\ & - 4.211(0.171) \mathbf{B} + 3.315(0.110) \mathbf{V} \end{aligned} \quad (17)$$

(*N* = 52, *SD* = 0.160, *R*<sup>2</sup> = 0.989, *F* = 852)

Careful examination of Eqns. 8 – 10 and Eqns. 15 – 17 reveals that to within the standard errors in the equation coefficients, the training set equation coefficients are identical to the equation coefficients for the full data sets. The training set expressions were then used to estimate the gas-to-IL partition coefficients for the 51 compounds in the log *K* test sets, and the water-to-IL partition coefficients of the 51 compounds in the log *P* test set. For the estimated and experimental values we found SD values of 0.142, 0.116 and 0.174; average absolute error (AAE) values of 0.122, 0.097 and 0.143; and average error (AE) values of 0.004, 0.012 and -0.028 for Eqns. 15–17, respectively. The small AE values indicate that there was very little bias in generating these estimated log *K* and log *P* values. The training and test set analyses were performed two more times with very similar statistical results.

The derived Abraham model correlations are expected to provide reasonably accurate partition coefficient predictions for additional organic compounds in anhydrous [MeoeMPip]<sup>+</sup>[FAP]<sup>-</sup> provided that solute's descriptor values fall within the range of **E** = 0.000 to 1.340; **S** = 0.000 to 1.310; **A** = 0.000 to 0.620; **B** = 0.000 to 0.740; **V** = 0.308 to 1.576; and **L** = 0.970 to 5.610. As an informational note, small gaseous solutes like carbon dioxide, methane, ethene, *etc.* would not be included in the above descriptor range because their **V** and **L** solute descriptors are too small. We were not able to find gas solubility data for these small solutes dissolved in anhydrous [MeoeMPip]<sup>+</sup>[FAP]<sup>-</sup>.

For ionic liquid solvents, Sprunger *et al.*<sup>35,36</sup> assumed that each equation coefficient could be separated into a cationic and an anionic contribution according to Eqns. 5 and 6 above. The authors proposed a relatively simple computation methodology for obtaining ion-specific equation coefficients for additional cations/anions based on previously calculated ion-specific equation coefficients. [FAP]<sup>-</sup>-specific equation coefficients of  $c_{k,anion} = 0.179$ ;  $e_{k,anion} = -0.015$ ;  $s_{k,anion} = 0.063$ ;  $a_{k,anion} = -1.314$ ;  $b_{k,anion} = 0.238$  and  $l_{k,anion} = -0.053$ <sup>32</sup> have been previously reported. The above [FAP]<sup>-</sup>-specific equation coefficients pertain to the log *K* Abraham model correlation for 298 K. The equation coefficients for the [MeoeMPip]<sup>+</sup> are computed by subtracting the existing [FAP]<sup>-</sup>-specific equation coefficients from the values given in Eqn. 8. Performing the indicated computation, the following numerical values of  $c_{k,cation} = -0.356$ ;  $e_{k,cation} = 0.015$ ;  $s_{k,cation} = 2.248$ ;  $a_{k,cation} = 2.563$ ;  $b_{k,cation} = 0.304$  and  $l_{k,cation} = 0.708$  are obtained for the [MeoeMPip]<sup>+</sup> cation. Numerical values for the [MeoeMPip]<sup>+</sup> cation for the log *P* (298 K) correlation would be calculated in similar using published values<sup>32</sup> of  $c_{p,anion} = 0.132$ ;  $e_{p,anion} = -0.171$ ;  $s_{p,anion} = 0.121$ ;  $a_{p,anion} = -1.314$ ;  $b_{p,anion} = 0.244$  and  $v_{p,anion} = -0.107$  for the [FAP]<sup>-</sup> anion in conjunction with Eqn. 10.

The calculated [FAP]<sup>-</sup>-specific equation coefficients can be combined with existing known values for other anions to generate Abraham model correlations for predicting gas-to-liquid partition coefficients of solutes dissolved in other anhydrous ionic liquid. For example, the Abraham model correlation for predicting gas-to-liquid partition coefficients of solutes in 1-methoxyethyl-

**Table 5.** Comparison of Experimental log *K* (298) Data and Predicted Values Based on Eqn. 18

Solute	log <i>K</i> <sub>exp</sub>	log <i>K</i> <sub>pred</sub>
Pentane	0.965	1.175
Hexane	1.318	1.533
3-Methylpentane	1.295	1.471
2,2-Dimethylbutane	1.113	1.309
Heptane	1.663	1.890
Octane	1.998	2.247
2,2,4-Trimethylpentane	1.650	1.843
Nonane	2.338	2.605
Decane	2.669	2.962
Cyclopentane	1.414	1.626
Cyclohexane	1.752	1.972
Methylcyclohexane	1.927	2.132
Cycloheptane	2.248	2.496
Cyclooctane	2.689	2.940
1-Pentene	1.190	1.296
1-Hexene	1.536	1.667
Cyclohexene	2.058	2.397
1-Heptene	1.889	2.015
1-Octene	2.227	2.373
1-Decene	2.888	3.071
1-Hexyne	2.187	2.211
1-Heptyne	2.527	2.625
1-Octyne	2.863	2.895
Benzene	2.850	2.837
Toluene	3.225	3.219
Ethylbenzene	3.515	3.520
<i>o</i> -Xylene	3.739	3.750
<i>m</i> -Xylene	3.604	3.589
<i>p</i> -Xylene	3.587	3.589
Styrene	3.970	3.933
$\alpha$ -Methylstyrene	4.179	4.191
Methanol	2.469	2.569
Ethanol	2.677	2.737
1-Propanol	3.026	3.124
2-Propanol	2.761	2.721
1-Butanol	3.403	3.527
2-Butanol	3.083	3.128
2-Methyl-1-propanol	3.222	3.327
Thiophene	2.997	2.977
Tetrahydrofuran	2.709	2.830
1,4-Dioxane	3.440	3.577
Methyl <i>tert</i> -butyl ether	1.995	1.985
Ethyl <i>tert</i> -butyl ether	1.897	2.139
Methyl <i>tert</i> -amyl ether	2.328	2.364
Diethyl ether	1.639	1.770
Dipropyl ether	2.150	2.434
Diisopropyl ether	1.809	1.969
Dibutyl ether	2.781	3.121
Acetone	2.779	2.673
2-Pentanone	3.349	3.280
3-Pentanone	3.334	3.275
Methyl acetate	2.627	2.575
Ethyl Acetate	2.864	2.814
Methyl propanoate	2.917	2.853
Methyl butanoate	3.191	3.215
Butanal	2.855	2.852
Acetonitrile	3.163	3.179
Pyridine	3.731	3.839
1-Nitropropane	3.913	3.926

1-methylpiperidinium bis(trifluoro-methylsulfonyl)imide, [MeoeMPip]<sup>+</sup>[(Tf)<sub>2</sub>N]<sup>-</sup>, is simply

$$\log K (298) = -0.356 + 0.015 E + 2.248 S + 2.563 A + 0.304 B + 0.708 L \quad (18)$$

as the [(Tf)<sub>2</sub>N]<sup>-</sup>-specific equation coefficients are  $c_{k,\text{anion}} = 0.000$ ;  $e_{k,\text{anion}} = 0.000$ ;  $s_{k,\text{anion}} = 0.000$ ;  $a_{k,\text{anion}} = 0.000$ ;  $b_{k,\text{anion}} = 0.000$  and  $l_{k,\text{anion}} = 0.000$ .<sup>35,36</sup> In establishing the computation methodology, equation coefficients for the bis(trifluoromethylsulfonyl)imide anion were set equal to zero to provide a reference point from which all other equation coefficients would be calculated. The cation- and anion-specific equation coefficients appear in the Abraham model as a summed pair, and one needs a reference point for isolating an unique set of individual cation and anion values. In many respects this is analogous to setting a reference point for calculating thermodynamic properties of single ions.

The predictive ability of Eqn. 18 can be assessed using the recently published experimental data of Marciniak and Wlazlo<sup>46</sup> for 60 organic solutes dissolved in [MeoeMPip]<sup>+</sup>[(Tf)<sub>2</sub>N]<sup>-</sup> at temperatures from 318.15 to 368.15 K. The measured log *K* (298 K) needed for comparison against the predicted values based on Eqn. 18 were obtained by extrapolating the 318.15 K and 328.15 K log *K* data back to 298.15 K assuming a linear log *K* versus 1/*T* behavior. Examination of the numerical values in Table 5 reveals that the Eqn. 18 provides reasonably accurate predictions of the partitioning behavior of the 60 organic solutes studied by Marciniak and Wlazlo. The average absolute deviation between the predicted and extrapolated experimental data was 0.16 log units, which is just slightly larger than the standard deviations in our derived log *K* correlations for [MeoeMPip]<sup>+</sup>[FAP]<sup>-</sup>. Past experience with the Abraham model has shown that IL-specific correlations (Eqns. 8 – 10) give slightly better predictions than correlations using the ion-specific equation coefficients (Eqn. 18). Predictions using the ion-specific equation coefficients are generally accurate enough for many practical applications, however, particularly in those instances where one does not have an IL-specific correlation expression to use.

#### 4. References

- Hallet, J. P., Welton, T. *Chem. Rev.*, 2011, 111, 3508.
- Sowmiah, S., Cheng, C. I. Chu, Y.-H. *Curr. Org. Synth.*, 2012, 9, 74.
- Sandhu, S., Sandhu, J. S. *Green Chem. Lett. Review*, 2011, 4, 289.
- Sandhu, S., Sandhu, J. S. *Green Chem. Let. Review*, 2011, 4, 311.
- Yao, C., Anderson, J. L. *J. Chromatogr. A*, 2009, 1216, 1658.
- Poole, C. F., Poole, S. K. *J. Sep. Sci.*, 2011, 34, 888.
- Ragonese, C., Sciarone, D., Tranchida, Dugo, P., Mondello, L. *J. Chromatogr. A*, 2012, 1255, 130.
- Pino, V., Afonso, A. M. *Anal. Chim. Acta*, 2012, 714, 20.
- Vidal, L., Rickkola, M.-L., Canals, A. *Anal. Chim. Acta*, 2012, 715, 19.
- Ho, T. D., Canestralo, A. J., Anderson, J. L. *Anal. Chim. Acta*, 2011, 695, 18.
- Abraham, M. H. *Chem. Soc. Reviews*, 1993, 22, 73.
- Abraham, M. H., Ibrahim, A., Zissimos, A. M. *J. Chromatogr. A*, 2004, 1037, 29.
- Stephens, T. W., Loera, M., Quay, A. N., Chou, V., Shen, C., Wilson, A., Acree, W. E. Jr., Abraham, M. H. *Open Thermodyn. J.*, 2011, 5, 104.
- Abraham, M. H., Acree, W. E. Jr. *Thermochim. Acta*, 2011, 526 (2011).
- Saifullah, M., Ye, S., Grubbs, L. M., De La Rosa, N. E., Acree, W. E. Jr., Abraham, M. H. *J. Solution Chem.*, 2011, 40, 2082.
- Abraham, M. H., Smith, R. E., Luchtefeld, R., Boorem, A. J., Luo, R., Acree, W. E. Jr. *J. Pharm. Sci.*, 2010, 99, 1500.
- Stephens, T. W., De La Rosa, N. E., Saifullah, M., Ye, S., Chou, V., Quay, A. N., Acree, W. E. Jr., Abraham, M. H. *Fluid Phase Equilib.*, 2011, 309, 30.
- Stephens, T. W., De La Rosa, N. E., Saifullah, M., Ye, S., Chou, V., Quay, A. N., Acree, W. E. Jr., Abraham, M. H. *Fluid Phase Equilib.*, 2011, 308, 64.
- Acree, W. E. Jr., Abraham, M. H. *J. Chem. Technol. Biotechnol.*, 2006, 81, 1441 [Erratum: *J. Chem. Technol. Biotechnol.*, 2006, 81, 1722].
- Mintz, C., Acree, W. E. Jr. *Phys. Chem. Liq.*, 2007, 45, 241.
- Mutelet, F., Revelli, A.-L., Jaubert, J.-N., Sprunger, L. M., Acree, W. E. Jr., Baker, G. A. *J. Chem. Eng. Data*, 2010, 55, 234.
- Revelli, A.-L., Mutelet, F., Jaubert, J.-N., Garcia-Martinez, M., Sprunger, L. M., Acree, W. E. Jr., Baker, G. A. *J. Chem. Eng. Data*, 2010, 55, 2434.
- Grubbs, L. M., Ye, S., Saifullah, M., McMillan-Wiggins, M. C., Acree, W. E. Jr., Abraham, M. H., Twu, P., Anderson, J. L. *Fluid Phase Equilib.*, 2011, 301, 257.
- Proctor, A., Sprunger, L. M., Acree, W. E. Jr., Abraham, M. H. *Phys. Chem. Liq.*, 2008, 46, 631.
- Abraham, M. H., Acree, W. E. Jr. *Green Chem.*, 2006, 8, 906.
- Moise, J.-C., Mutelet, F., Jaubert, J.-N., Grubbs, L. M., Acree, W. E. Jr., Baker, G. A. *J. Chem. Eng. Data*, 2011, 56, 3106.
- Sprunger, L. M., Acree, W. E. Jr., Abraham, M. H. *Phys. Chem. Liq.*, 2010, 48, 394.
- Grubbs, L. M., Ye, S., Saifullah, M., Acree, W. E. Jr., Twu, P., Anderson, J. L., Baker, G. A., Abraham, M. H. *J. Solution Chem.*, 2011, 40, 2000.
- Sprunger, L. M., Gibbs, J., Baltazar, Q. Q., Acree, W. E. Jr., Abraham, M. H., Anderson, J. L. *Phys. Chem. Liq.*, 2009, 47, 74.
- Grubbs, L. M., Saifullah, M., De La Rosa, N. E. Acree, W. E. Jr., Abraham, M. H., Zhao, Q., Anderson, J. L. *Glob. J. Phys. Chem.*, 2010, 1, 1.
- Stephens, T. W., Acree, W. E. Jr., Twu, P., Anderson, J. L., Baker, G. A., Abraham, M. H. *J. Solution Chem.*, 2012, 41, 1165.
- Acree, W. E. Jr., Grubbs, L. M., Abraham, M. H., Selection of Ionic Liquid Solvents for Chemical Separations Based on the Abraham Model, in *Ionic Liquids: Applications and Perspectives* (Book 2), Kokorin, A. (Editor), INTECH Publishers, 2011, Chapter 13, 273.
- Revelli, A.-L., Sprunger, L. M., Gibbs, J., Acree, W. E. Jr., Baker, G. A., Mutelet, F. *J. Chem. Eng. Data*, 2009, 54, 977.
- Sprunger, L. M., Acree, W. E. Jr., Abraham, M. H. *Phys. Chem. Liq.*, 2010, 48, 385.

- <sup>35</sup> Sprunger, L., Clark, M., Acree, W. E. Jr., Abraham, M. H. *J. Chem. Inf. Model.*, 2007, 47, 1123.
- <sup>36</sup> Sprunger, L. M., Proctor, A., Acree, W. E. Jr., Abraham, M. H. *Fluid Phase Equilib.*, 2008, 265, 104.
- <sup>37</sup> Sprunger, L. M., Gibbs, J., Proctor, A., Acree, W. E. Jr., Abraham, M. H., Meng, Y., Yao, C., Anderson, J. L. *Ind. Eng. Chem. Res.*, 2009, 48, 4145.
- <sup>38</sup> Marciniak, A., Wlazlo, M. *J. Chem. Thermodyn.*, 2013, in press, [<http://dx.doi.org/10.1016/j.jct.2012.08.016>].
- <sup>39</sup> Baltazar, Q. Q., Leininger, S. K., Anderson, J. L. *J. Chromatogr. A*, 2008, 1182, 119.
- <sup>40</sup> Abraham, M. H., Andonian-Haftvan, J., Whiting, G. S., Leo, A., Taft, R. W. *J. Chem. Soc., Perkin Trans 2*, 1994, 1971.
- <sup>41</sup> Abraham, M. H., Ibrahim, A., Acree, W. E. Jr. *Fluid Phase Equilib.*, 2007, 251, 93.
- <sup>42</sup> Abraham, M. H., Ibrahim, A., Zissimos, A. M. *J. Chromatogr. A*, 2004, 1037, 29.
- <sup>43</sup> Zissimos, A. M., Abraham, M. H., Barker, M. C., Box, K. J., Tam, K. Y., *J. Chem. Soc. Perkin Trans. 2*, 2002, 470.
- <sup>44</sup> Zissimos, A. M., Abraham, M. H., Du, C. M., Valko, K., Bevan, C., Reynolds, D., Wood, J., Tam, K. Y., *J. Chem. Soc., Perkin Trans. 2*, 2002, 2001.
- <sup>45</sup> Dohanvosova, P., Sarraute, S., Dohnal, V., Majer, V., Gomes, M. C. *Ind. Eng. Chem. Res.*, 2004, 43, 2805.
- <sup>46</sup> Marciniak, A., Wlazlo, M. *J. Chem. Thermodyn.*, 2012, 49, 137.

Received: 30.09.2012.

Accepted: 04.10.2012.



# AFM-Investigations , Structural Visualization Studies, and Temperature Optimization of Single Metal Cyclotetraphosphates Synthesized at Elevated Temperature

Khaled M. Elsabawy<sup>[a,b]\*</sup> , A. El-Maghraby<sup>[b,c]</sup>

**Keywords:** Synthesis ; Ceramics ; Visualization; Metal cyclotetraphosphates; Structure;

The precursor metal dihydrogen phosphate dihydrate was synthesized by a rapid and simple precipitation method using phosphoric acid, cobalt nitrate at ambient temperature (cobalt(II) was selected as model for metal in these investigations). The precursor was heated and sintered at different temperatures (600, 800, 1000 and 1100 °C) respectively, to optimize the conditions to obtain Co<sub>2</sub>P<sub>4</sub>O<sub>12</sub> crystal form with high purity. The products were monitored by both of XRD, IR spectra by additional to accurate imaging via scanning electron microscope (SEM) and AFM-microscope to analyze surface topology and microstructural features of the metal cyclotetraphosphate. Structural investigations via XRD proved that the product obtained at 1100°C is the best and have fine structure with monoclinic structure phase and C12/c1 space group with lattice parameter  $a = 11.809(2)$ ,  $b = 8.293(1)$ ,  $c = 9.923(2)$  Å, respectively. A visualized investigations were performed to confirm structure validity and stability at sintering temperature (1100 °C) . Visualization studies indicated that variations in bond distances between Co1, Co2, P1 and P2 and different six oxygen atoms (O1 ,O2 , O3 ,O4 ,O5 and O6) inside crystal lattice are responsible for increasing lattice flexibility factor (by controlling in shrinkage and expansion coefficient) and consequently increase its bonds stability to break .

\* Corresponding Authors

E-Mail: ksabawy@yahoo.com

[a] Materials Science Unit , Chemistry Department ,Faculty of Science,Tanta University-31725-Tanta-Egypt

[b] Department of Chemistry, Faculty of Science, Taif University, 888- Taif, Kingdom of Saudi Arabia

[c] Ceramic Department, Chemistry Unit, National Research Center, Dokki, Tahrir st., Egypt

## Introduction

In the last decade, synthesis and structures of inorganic phosphates at micro-/nanoscale levels is a significant challenge, which attracts increased attention because of their strong influence on the chemical and physical properties of materials.<sup>1-3</sup>

Morphology influences not only the intrinsic chemical, optical, and catalytic properties of micro/nano scale metal phosphates, but also their relevant applications in electronic, biocompatible and biodegradable in tissue.<sup>2,4</sup>

As one of the members of phosphate material family, transition metal cyclotetraphosphate micro-/nanoparticles can be used as potential pigments, selective catalysts, phosphors, materials for corrosion-resistant coatings and biocompatible and biodegradable in tissues.<sup>5-8</sup> Several bivalent including 3d metals, namely, Mn, Co, Fe, Zn, Cu, and Ni, are known to form the single metal cyclotetraphosphate M<sub>2</sub>P<sub>4</sub>O<sub>12</sub>, where M(II) stands for a bivalent metal. The binary metal cyclotetraphosphates M<sub>2-x</sub>A<sub>x</sub>P<sub>4</sub>O<sub>12</sub> (M and A=Mg, Ca, Mn, Co, Ni, Zn, or Cu; x=0-2), isostructural with the single metal cyclotetraphosphates M<sub>2</sub>P<sub>4</sub>O<sub>12</sub>, were prepared by Trojan et al.<sup>5-8</sup> and Boonchom et al.<sup>9-11</sup> All these compounds have similar X-ray diffraction patterns and close unit cell parameters, which crystallize in monoclinic space group

C2/c (Z=4).<sup>12</sup> Various methods have been employed to synthesize binary metal cyclotetraphosphates, including two-step thermal method,<sup>5-8</sup> hydrothermal synthesis<sup>5</sup> and the decomposition of binary metal(II) dihydrogenphosphates (M<sub>1-y</sub>A<sub>y</sub>(H<sub>2</sub>PO<sub>4</sub>)<sub>2</sub>.nH<sub>2</sub>O; where M and A=Ca, Mg, Mn, Fe, Co, Ni, Cu or Zn; y=0-1; n=1-4).<sup>9-11</sup> This work is of immense interest because it appears economically advantageous to replace partially the divalent metal cations by some cheaper bivalent element which could also improve special properties as above mentioned.<sup>1-4</sup> However, it is relevant to synthesize binary cyclotetraphosphate and its solid solution because changing the metal ratio influences its useful properties. Consequently, it is a major challenge to synthesize binary metal cyclotetraphosphate micro/nano particles with its intrinsic shape-dependent properties and resulting application. Recently, cobalt iron pyrophosphate CoFe<sub>2</sub>O<sub>7</sub> and cobalt iron cyclotetraphosphate CoFeP<sub>4</sub>O<sub>12</sub> were prepared by mixing of CoCO<sub>3</sub>, Fe and H<sub>3</sub>PO<sub>4</sub> in water-methanol and in water- acetone, respectively.<sup>13,14</sup>

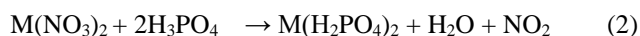
The difference of media (solvents) in the precipitation process leads to obtain different phosphates, as revealed by XRD and FTIR data. Due to its solubility in water and its ability to associate with metal ions in media, solvent has been used as a binder cum gel for shaping materials (bulk, porous, micro- or nano particles) and a matrix for entrapment of ions to generate a gelled precursor which resulted in obtaining different material or same material with different size and morphology after heat treatment. The results obtained are also in agreement with other phosphate group reported in literature.<sup>15,16</sup>

The major objective of the present investigations is understanding the role of structural parameters within crystal lattice of M<sub>2</sub>P<sub>4</sub>O<sub>12</sub> that stabilize structure of crystal even at elevated temperatures. Furthermore understanding the structural parameters effects on the morphological and surface nature of metalized cyclotetraphosphates.

## Experimental

### Synthesis of metal cyclotetraphosphates

The cobalt cyclotetraphosphate was synthesized via three step reactions. First reaction is dissolving cobalt carbonate in few drops of concentrated nitric acid forming acidic cobalt nitrate then solution neutralized by condensed ammonia solution. The second step is the reaction with 70% phosphoric acid forming cobalt dihydrogen phosphate at temperature 230 °C, the third step is heating followed by sintering process at 1100 °C to form violet powder from pure cobalt cyclotetraphosphate. These steps are in partial agreement with the method of Parada et al.<sup>5</sup>



where M=Co. The violet powder from pure cobalt cyclotetraphosphate was grounded in agate mortar for 15 min, then the resulted powder forwarded to perform the different structural measurements.

### Structural measurements

The X-ray diffraction (XRD) measurements were carried out at room temperature on the fine ground samples using Cu-K $\alpha$  radiation source, Ni-filter and a computerized STOE diffractometer/Germany with two  $\theta$  step scan technique. Rietveld refinement and indexing of structure were made via Fullprof package and GEsas program.

A visualized studies of crystal structure were made by using Diamond Molecular Structure version 3.2 package, Germany and MERCURY-2.3 depending up on single crystal structural data of pure cobalt cyclotetraphosphates including atomic coordinates of monoclinic phase supplied from ICSD-Karlsruhe-Germany. Scanning electron microscopy (SEM) measurements were carried out along ab-plane using a small pieces of the prepared samples by using a computerized SEM camera with elemental analyzer unit Shimadzu (Japan). Atomic force microscopy (AFM): High-resolution Atomic Force Microscopy (AFM) is used for testing morphological features and topological map (Veeco-di Innova Model-2009-AFM-USA). The applied mode was tapping non-contacting mode. For accurate mapping of the surface topology AFM-raw data were forwarded to the Origin-Lab version 6-USA program to visualize more accurate three dimension surface of the sample under investigation. This process is new trend to get high resolution 3D-mapped surface for very small area.

A visualization study made is concerned by matching and comparison of experimental and theoretical data of atomic positions, bond distances, oxidation states and bond torsion on the crystal structure formed. Some of these data can be obtained free of charge from The Cambridge Crystallographic Data Centre via [www.ccdc.cam.ac.uk/data\\_request/cif](http://www.ccdc.cam.ac.uk/data_request/cif), or by emailing [data\\_request@ccdc.cam.ac.uk](mailto:data_request@ccdc.cam.ac.uk), or by contacting ICSD-Fiz-Karlsruhe-Germany.

### FT-Infrared Spectroscopy

The infrared spectra of the solid products obtained were recorded from KBr discs using a Shimadzu FT-IR Spectrophotometer in the range from 400 to 4000 cm<sup>-1</sup>.

## RESULTS AND DISCUSSION

### Structural Identification

Fig.1 displays different x-ray diffraction patterns of cobalt cyclotetraphosphate at different sintering temperatures (600, 800, 1000 and 1100 °C) respectively. The accurate analyses of these patterns were performed by using both of Rietveld and indexing via Fullprof package and GEsas program. The analysis is focused on the main intense reflection peaks (fingerprint of structure) and indicated that cobalt cyclotetraphosphate is mainly belong to single monoclinic phase with C12/c1 space group as symbolized by pink circles in Fig.1 and only very few percentage of cobalt oxide as secondary phase in minor. It was observed that the impurity phases are decreasing as sintering temperatures are increasing as shown in Fig.1 where impurity phases are assigned by blue squares. The comparisons of most intense reflections peaks in all patterns (fingerprint reflections represent monoclinic-phase) indicated that cobalt cyclotetraphosphate, which is sintered at 1100 °C is the best fit one with high purity than others which sintered at temperatures 600, 800 and 1000 °C, respectively.

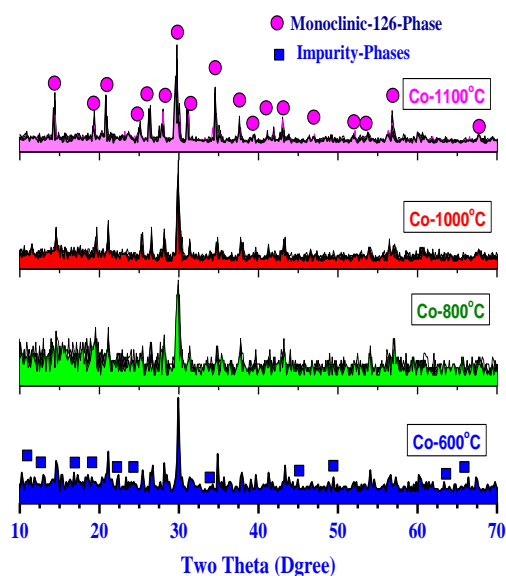


**Figure 1.** X-ray diffraction patterns of cobalt cyclotetraphosphate formed at different sintering temperatures (600, 800, 1000 and 1100°C) respectively.

In the hypothesis of isostructural, due to existence of cobalt(II) and cobalt(III) the spectrum peaks for the system of cobalt cyclotetraphosphate (solid solution) which is single metal cyclotetraphosphate (M<sub>2</sub>P<sub>4</sub>O<sub>12</sub>, M=Co) are quite similar because of the equivalent electronic charges and the close radii of cations. Consequently, all the diffraction peaks in the Fig.1 are found to be in a good agreement with monoclinic M<sub>2</sub>P<sub>4</sub>O<sub>12</sub> and space group C12/c1 without violation. Only a few characteristic peaks of other impurities

(e.g. Co-Oxide) was clearly observed at lower sintering temperatures (600, 800°C).

From XRD analysis (Fig. 1), grain size evaluated and calculated according to the Scherrer's formula:  $D = K\lambda / (\beta \cos\theta)$ , where  $D$  is particle diameter,  $K=0.89$  (the Scherrer's constant),  $\lambda=1.5406$  (wavelength of the X-ray used),  $\beta$  is the width of line at the half-maximum intensity and  $\theta$  is the corresponding angle. The average crystallite size of product is estimated from the strongest three diffraction peaks below 40° for  $2\theta$  and found to be  $98 \pm 11$  nm. This crystal size of the prepared cobalt cyclotetraphosphate is smaller than those of data estimated from SEM and AFM-investigations in the present work which confirms that the powder mixture of cobalt cyclotetraphosphate is not unified grain sizes and grain sizes are varied in the bulk than surface's layers. The lattice parameters were calculated from the XRD spectra and found to be  $a=11.809(2)$ ,  $b=8.293(1)$ ,  $c=9.923(2)$  Å, which are very close to those of the standard data file (ICSD #300027) and the literatures also.<sup>9-11,14</sup>

### FT-IR-Spectroscopic Investigations

Fig. 2 displays infrared spectra recorded for  $\text{Co}_2\text{P}_4\text{O}_{12}$  (126-Phase =  $\text{AB}_2\text{X}_6$  structure type) after heating process and sintering at 1100 °C. The most intense reflection peak of IR-spectra are assigned by red cycles as clear in Fig. 2. It is well known that the  $\text{Co}_2\text{P}_4\text{O}_{12}$  structure is mainly characterized by a three-dimensional framework with  $\text{MO}_6$  ( $M=\text{Co}$ ) polyhedral linked with  $\text{P}_4\text{O}_{12}$  rings by  $M\text{-O-P}$ . The basic structure unit is the centrosymmetric cyclotetraphosphate ring  $\text{P}_4\text{O}_{12}$  and therefore vibrational modes can consider it as made up of the  $[\text{P}_4\text{O}_{12}]^{4-}$  anion. The different vibrational modes of  $[\text{P}_4\text{O}_{12}]^{4-}$  ion observed in the frequency range of 370–1400  $\text{cm}^{-1}$  are assigned according to the literature.<sup>17-19</sup>

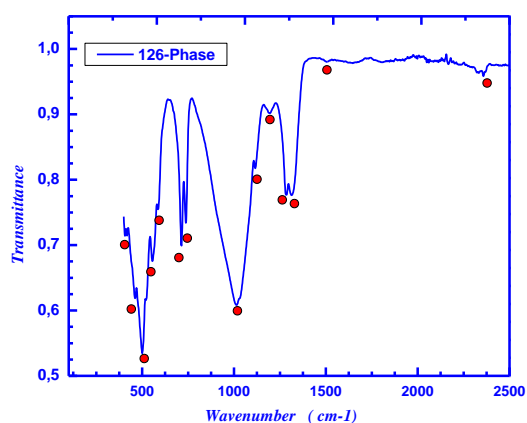


**Figure 2.** Infrared spectra recorded for  $\text{Co}_2\text{P}_4\text{O}_{12}$  (126-Phase =  $\text{AB}_2\text{X}_6$  structure type) after firing process and sintering at 1100 °C.

The peaks splitting in these regions is due to the different strength of the bond between cations ( $M = \text{Co}^{2+}$  or  $\text{Co}^{3+}$ ) and anion  $[\text{P}_4\text{O}_{12}]^{4-}$ , which confirms the inserting different cations in the skeletal as well as the formation of multi-valence cobalt(II,III) cyclotetraphosphate also as confirmed in the visualization studies part. The anion contains the

$[\text{PO}_2]^{2-}$  radical and the  $\text{P-O-P}$  bridge which differs in their bond strength and as a result multi-splitting processes are occurred as shown in Fig. 2. As the  $\text{P-O}$  bond strength in the  $[\text{PO}_2]^{2-}$  radical is stronger than in the  $\text{P-O-P}$  bridge, the stretching frequencies of the  $[\text{PO}_2]^{2-}$  radical are expected to be higher than those in the  $\text{P-O-P}$  bridge. The  $\text{P-O}$  bonds in the  $[\text{PO}_2]^{2-}$  radical show its asymmetric and symmetric stretching frequencies around 1327–1237 and 1150–1000  $\text{cm}^{-1}$ , respectively.

The asymmetric and symmetric stretching frequencies of the  $\text{P-O-P}$  bridge are observed in the regions of 1000–900 and 800–700  $\text{cm}^{-1}$ , respectively. The symmetric  $\text{P-O-P}$  bridge stretching modes occur at 736 and 714  $\text{cm}^{-1}$ . These observed bands are known to be the most striking feature of cyclotetraphosphate spectra, along with the presence of the  $\nu_{\text{as}}(\text{OPO})$  band. From X-ray diffraction data,<sup>12</sup> it was shown that the crystal structure is monoclinic (space group  $C2/c$ ) with a cyclic structure of the  $[\text{P}_4\text{O}_{12}]^{4-}$  anion. This has been confirmed by the IR measurements. The bending modes are expected in the area 600–400  $\text{cm}^{-1}$  ( $[\text{PO}_2]^{2-}$  radical) and 400–370  $\text{cm}^{-1}$  ( $\text{P-O-P}$  bridge). The metal–O stretching usually appears in the bending mode region as the bending modes of the  $\text{P-O-P}$  bridge and absorption bands associated with these vibrations are usually very weak. The weak IR band at 400  $\text{cm}^{-1}$  is probably due to metal–oxygen (Co–O) stretching mode.

### Scanning Electron Microscopy (SEM) and EDX-Elemental Analysis (EDX)

Fig. 3a shows scanning electron micrograph recorded for cobalt cyclotetraphosphate synthesized at 1100 °C, it is so difficult to observe inhomogeneity within the micrograph due to that the powders used are very fine and the grain size estimated is too small.

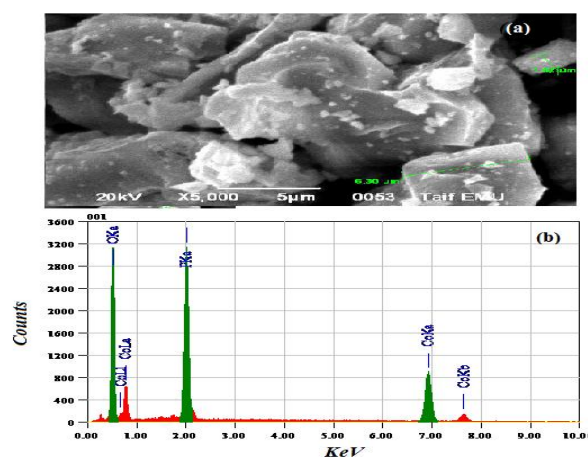


**Figure 3.** Scanning electron micrograph recorded for cobalt cyclotetraphosphate synthesized at 1100°C with average grain size ranged in between 3.2–3.78 μm.

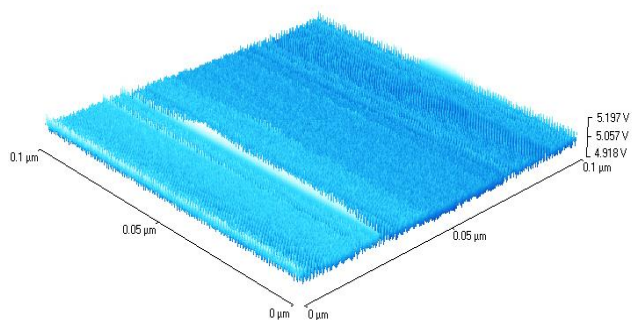
The average grain size was estimated from SE-micrograph and found to be ranged in between 3.2–3.78 μm which is relatively high in contrast with data estimated from XRD through Scherrer's equation ( $D=0.98$  μm). This indicates that the actual grain size in the material bulk could be smaller than that detected on the surface morphology.

Furthermore, in our EDX (energy disperse X-ray) analysis as shown in Fig. 3b and Table 1a, the molar ratios of cobalt cyclotetraphosphate was detected qualitatively with very good fitting to the actual molar ratio(1:2:6) as shown in Table 1a (Supplementary material).

The EDX examinations were performed on random spots within the same sample to confirm accuracy of calculations molar ratios of cobalt cyclotetraphosphate as possible .

#### Atomic Force Investigations ( AFM ) :

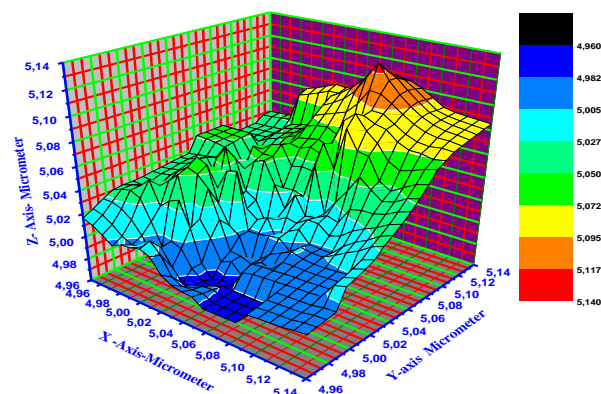
Fig.4 shows 3D-AFM-micrograph tapping mode image trapped for scanned area  $0.1 \mu\text{m}^2$  of cobalt cyclotetraphosphate ( $\text{Co}_2\text{P}_4\text{O}_{12}$ ).The image was constructed by application tapping mode with slow scan rate and high resolution imaging with 1024 line per  $0.1 \text{ nm}$ .The tapping amplitude current was monitored as a function of line drawing heights. For more accurate surface analysis AFM-raw data was forwarded to Origin Lab program version 7 and the data are converted into matrix then 3D-contour surface mapping is constructed as shown in Fig.5a.



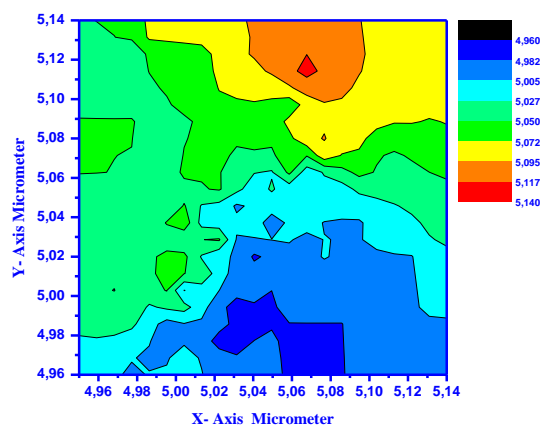
**Figure 4.** 3D-AFM-micrograph tapping mode image recorded for scanned area  $0.1 \mu\text{m}^2$  of cobalt cyclotetraphosphate ( $\text{Co}_2\text{P}_4\text{O}_{12}$ ).

Fig.5a displays 3D-visualized-contour plot of AFM-micrograph surface image trapped for scanned area  $0.2 \mu\text{m}^2$  of cobalt cyclotetraphosphate ( $\text{Co}_2\text{P}_4\text{O}_{12}$ ). To increase the accuracy of analysis of this image the data were forwarded to plot Fig.5b which is 2D-visualized-contour plot of the same image of cobalt cyclotetraphosphate ( $\text{Co}_2\text{P}_4\text{O}_{12}$ ). The analysis of the surface nature and morphology enrich us to understand application of such these materials metal cyclotetraphosphate ( $\text{M}_2\text{P}_4\text{O}_{12}$ ) as colorant materials in coating and ceramic industry .

The AFM-tapping mode trapped image can be divided into three zones 1<sup>st</sup> zone include (yellow, orange and red color) this zone represents ~21% of the whole scanned area which is equal  $\sim 0.042 \mu\text{m}^2$ , the surface heights in this zone ranged in between  $6.072\text{-}6.14 \mu\text{m}$  as clear in the key-image .The red zone represents  $2\%=0.004 \mu\text{m}^2$  which processes the highest height on the scanned area with  $\text{height}_{\text{max}}=6.14 \mu\text{m}$ . The second zone represents  $\sim$  [dark green zone (23%) + pale green zone (18%)] which represents  $\sim 41\%$  ( $0.082 \mu\text{m}^2$ ) from the whole scanned area with heights gradient ranged in between  $6.027\text{-}6.06 \mu\text{m}$  .



**Figure 5a.** 3D-visualized-contour plot of AFM-micrograph surface image recorded for scanned area  $0.2 \mu\text{m}^2$  of cobalt cyclotetraphosphate ( $\text{Co}_2\text{P}_4\text{O}_{12}$ ).



**Figure 5b.** 2D-visualized-contour plot of AFM-micrograph tapping mode image recorded for scanned area  $0.2 \mu\text{m}^2$  of cobalt cyclotetraphosphate ( $\text{Co}_2\text{P}_4\text{O}_{12}$ ).

The 3<sup>rd</sup> zone occupies  $\sim 38\% = 0.076 \mu\text{m}^2$  from the whole scanned area with heights gradient lies in between  $4.88\text{-}6.06 \mu\text{m}$ . The average grain size was estimated from AFM-analysis and found in between  $56\text{-}80 \text{ nm}$  which is nearly matched with that calculated from XRD by applying Scherrer's formula ( $\sim 98 \text{ nm}$ ). The differences in the values of average grain sizes calculated via SEM, AFM and Scherrer's formula are good evidence for existence gradient in the grain sizes in the bulk which are completely different than those on the surface layers.

#### Structural Visualization Studies

Fig. 6 displays the unit cell of cobalt cyclotetraphosphate which built up via DIAMOND IMPACT CRYSTAL PROGRAM version 3.2 depending on the single crystal data and atomic coordinates locations of pure cobalt cyclotetraphosphate. The unit cell was visualized and built up with minimum 138 atoms (Co=16, P=38 and O=94 atoms) and four edges. A visualization study made is concerned by matching and comparison of experimental and theoretical data of atomic positions, bond distances, oxidation states and bond torsion on the crystal structure formed .

**Table.1.** Selected bond lengths and angles inside crystal lattice of Co<sub>2</sub>P<sub>4</sub>O<sub>12</sub>

Atom1	Atom2	d <sub>1-2</sub> Å	Atom3	d <sub>1-3</sub> Å	Angle 312
Co1	O1	2.0927	O1	2.0927	180.000
	O1	2.0927	O2	2.3366	82.238
	O1	2.0927	O2	2.3366	97.762
	O2	2.3366	O2	2.3366	180.000
	O2	2.3366	O5	2.4865	116.323
	O5	2.4865	O3	2.8210	57.061
	O5	2.4865	P1	3.0353	157.072
	O3	2.8210	O3	2.8210	180.000
	O3	2.8210	P2	2.9164	144.014
	P2	2.9164	P2	2.9164	180.000
	P2	2.9164	P1	3.0353	71.568
	P2	2.9164	O4	3.5270	29.627
	P2	2.9164	O6	3.5756	80.753
	P1	3.0353	P1	3.0353	180.000
	P1	3.0353	O6	3.5756	21.363
	O4	3.5270	O6	3.5756	96.488
	O4	3.5270	O6	3.5756	83.512
	O6	3.5756	O6	3.5756	180.000
	O6	3.5756	P2	3.6583	79.758
	O6	3.5756	P2	3.6583	100.242
Co2	O6	2.1694	O6	2.1694	93.593
	O6	2.1694	O5	2.3208	84.836
	O6	2.1694	O5	2.3208	174.602
	O6	2.1694	O2	2.5737	112.127
	O6	2.1694	O2	2.5737	71.914
	O5	2.3208	O4	3.5398	76.791
	O5	2.3208	P2	3.7464	74.787
	O5	2.3208	P2	3.7464	116.925
	O5	2.3208	O3	3.9043	138.211
	O5	2.3208	O3	3.9043	120.351
	O2	2.5737	O2	2.5737	174.457
	O2	2.5737	P1	3.1577	77.031
	O2	2.5737	O6	3.3434	98.404
	O2	2.5737	O6	3.3434	80.635
	P1	3.1577	O4	3.5398	93.099
	P1	3.1577	O3	3.9043	107.617
	P1	3.1577	O3	3.9043	136.556
	O6	3.3434	O6	3.3434	160.281
	O6	3.3434	P1	3.4087	138.822
	P1	3.4087	P1	3.4087	79.006
	P1	3.4087	O1	3.5271	84.012
	P1	3.4087	O1	3.5271	67.309
	P1	3.4087	O4	3.5398	103.558
	O1	3.5271	P2	3.7464	25.747
	O1	3.5271	P2	3.7464	144.026
	O1	3.5271	O3	3.9043	56.224
	O1	3.5271	O3	3.9043	87.439
	O4	3.5398	O4	3.5398	88.346
	O4	3.5398	P2	3.7464	74.116
	O4	3.5398	P2	3.7464	118.697
	P2	3.7464	O3	3.9043	72.236
	P2	3.7464	O3	3.9043	91.882
	P2	3.7464	O3	3.9043	91.882
	P2	3.7464	O3	3.9043	72.236
	O3	3.9043	O3	3.9043	37.949

**Table.2.** Selected bond lengths and angles inside crystal lattice of Co<sub>2</sub>P<sub>4</sub>O<sub>12</sub>

Atom1	Atom2	d <sub>1-2</sub> Å	Atom3	d <sub>1-3</sub> Å	Angle 312^
P1	O5	1.2222	O6	1.3354	112.012
	O5	1.2222	O3	1.8394	111.327
	O5	1.2222	O4	1.9623	98.852
	O5	1.2222	Co1	3.0353	52.425
	O6	1.3354	O1	3.8450	71.883
	O6	1.3354	O6	3.9043	47.653
	O1	3.4635	O1	3.9266	106.380
	O1	3.4635	O2	3.9527	25.309
	O1	3.4635	P1	3.9812	156.181
	O3	1.8394	Co1	3.0353	65.455
	O3	1.8394	Co2	3.1577	148.445
	O4	1.9623	O1	3.9266	47.041
	O4	1.9623	O2	3.9527	87.564
	O4	1.9623	P1	3.9812	64.088
	Co1	3.0353	Co2	3.1577	83.872
	Co1	3.0353	O3	3.3910	107.797
	Co1	3.0353	Co2	3.4087	90.253
	Co2	3.1577	P2	3.4815	133.588
	Co2	3.1577	O1	3.5216	76.412
	O3	3.3910	O1	3.8450	90.375
	Co2	3.4087	O1	3.9266	108.957
	Co2	3.4087	O2	3.9527	40.078
	O2	3.5532	O2	3.9527	62.931
	O2	3.5532	P1	3.9812	152.445
	O3	3.4278	P2	3.4815	82.722
	P2	3.4815	O1	3.5216	59.248
	P2	3.5485	O2	3.5982	110.496
	O4	3.5878	O2	3.5982	95.547
	O4	3.5878	O1	3.8450	84.205
	O4	3.5878	O6	3.9043	96.550
	O4	3.5878	O1	3.9266	72.730
P2	O2	1.3584	O1	1.6346	90.263
	O2	1.3584	O4	1.7500	122.795
	O1	1.6346	O5	3.8101	159.446
	O1	1.6346	O4	3.8181	47.186
	O1	1.6346	O5	3.8547	102.964
	O4	1.7500	O3	1.7746	85.307
	O4	1.7500	Co1	2.9164	94.901
	O3	1.7746	O5	3.8101	34.432
	O3	1.7746	O5	3.8547	105.956
	Co1	2.9164	O5	3.4562	164.249
	Co1	2.9164	O1	3.4618	37.075
	O5	3.4562	O4	3.8181	61.446
	O5	3.4562	O5	3.8547	151.691
	O1	3.4618	P1	3.4815	60.953
	O1	3.4618	P1	3.5485	68.115
	P1	3.5485	O5	3.8101	69.465
	P1	3.5485	O4	3.8181	128.505
	P1	3.5485	O5	3.8547	127.918
	O6	3.5725	O3	3.5777	169.950
	O6	3.5725	Co1	3.6583	84.063
	O3	3.5777	O4	3.8181	51.319
	O3	3.5777	O5	3.8547	130.744
	Co1	3.6583	O2	3.7104	36.966
	Co1	3.6583	O1	3.7128	122.659

Table 2 (cont.)

Atom1	Atom2	d <sub>1-2</sub> Å	Atom3	d <sub>1-3</sub> Å	Angle 312
P2	O5	3.6692	O5	3.8547	147.193
	O2	3.7104	O1	3.7128	156.019
	Co2	3.7464	O5	3.8547	35.519
	O5	3.8101	O4	3.8181	112.308

Table 3. Selected bond lengths and angles inside crystal lattice of Co<sub>2</sub>P<sub>4</sub>O<sub>12</sub>.

Atom1	Atom2	d <sub>1-2</sub> Å	Atom3	d <sub>1-3</sub> Å	Angle 312
O1	P2	1.6346	Co1	2.0927	157.754
	P2	1.6346	O2	2.1302	39.621
	P2	1.6346	P1	3.9266	82.859
	Co1	2.0927	O2	2.1302	151.780
	Co1	2.0927	O5	2.6771	61.400
	O2	2.1302	O6	3.6570	81.232
	O2	2.1302	P2	3.7128	114.101
	O2	2.9186	O4	2.9451	75.146
	O2	2.9186	O4	2.9609	129.658
	O4	2.9451	O5	3.7359	138.844
	O4	2.9451	O6	3.7769	69.906
	O3	3.0569	O2	3.3406	135.391
	O3	3.0569	P2	3.4618	113.44
	O2	3.3406	P1	3.9266	79.250
	P2	3.4618	O3	3.5075	29.494
	O3	3.5174	O3	3.8471	157.065
	O3	3.5174	P1	3.9266	159.635
	P1	3.5216	Co2	3.5271	163.460
	P1	3.5216	O6	3.6570	129.656
	Co2	3.5271	P1	3.9266	118.457
	O6	3.6570	P2	3.7128	70.152
	P2	3.7128	P1	3.9266	148.032
	O5	3.7359	O6	3.7769	79.868
	O5	3.7359	P1	3.8450	18.483
	O5	3.7359	O3	3.8471	140.930
	O5	3.7359	P1	3.9266	120.490
	O6	3.7769	O3	3.8471	138.211
	O6	3.7769	P1	3.9266	141.255
	P1	3.8450	O3	3.8471	159.386
	O3	3.8471	P1	3.9266	27.350
O2	P2	1.3584	O1	2.1302	50.116
	P2	1.3584	Co1	2.3366	100.899
	O1	2.1302	O6	3.8732	144.603
	O1	2.1302	O6	3.9416	66.484
	O1	2.1302	P1	3.9527	94.733
	Co1	2.3366	O5	2.5475	61.027
	O5	2.5475	O6	3.8732	30.571
	O5	2.5475	O6	3.9416	84.546
	Co2	2.5737	O6	3.9416	30.654
	Co2	2.5737	P1	3.9527	58.507
	O3	2.6359	O4	2.7355	52.758
	O3	2.6359	O6	2.8042	141.814
	O4	2.7355	O6	3.9416	116.394
	O4	2.7355	P1	3.9527	78.086
	O6	2.8042	O1	2.9186	126.931
	O6	2.8042	O1	3.3406	83.218

Table 3 (cont.)

Atom1	Atom2	d <sub>1-2</sub> Å	Atom3	d <sub>1-3</sub> Å	Angle 312
O2	O6	2.8042	O4	3.5756	115.388
	O6	2.8042	P1	3.5982	63.049
	O6	2.8042	P2	3.7104	126.522
	O6	2.8042	O6	3.9416	52.695
	O6	2.8042	P1	3.9527	11.746
	O1	2.9186	O1	3.3406	83.639
	O1	2.9186	O4	3.5756	52.764
	O1	2.9186	P1	3.5982	64.434
	O4	3.5756	O6	3.9416	73.486
	P1	3.5982	P2	3.7104	73.993
	P1	3.5982	O6	3.8732	20.160

Many researchers in the past did their best to understand the crystallographic structure of phosphates (open phosphates or cyclic poly phosphates).<sup>20-28</sup>

The initial analysis of structural parameters inside visualized crystal lattice of cobalt cyclotetraphosphate indicated that there are two different types of cobalt, namely (Co1 and Co2). Two types of phosphorous atoms (P1 and P2) and finally six different types of oxygen atoms namely (O1, O2, O3, O4, O5 and O6).

The comparison between visualized XRD-profile (Supplementary material) and the experimental XRD-pattern sintered at 1100 °C Fig. 1, indicated that there is type of fitting coupled with high figure of merit between both patterns specially on the point of view positions of most intense reflection peaks on both patterns. The shifts on some intense reflection peak position within limits of two theta values ~2 degree could due to impurity phases interactions with the main monoclinic structure of cobalt cyclotetraphosphate on the experimental pattern. Fig.7 displays the regular distribution of PO<sub>3</sub>-polyhera throughout the unit cell of cobalt cyclotetraphosphate. The analysis of these polyhedron indicated that the phosphorous atom as central ion was surrounding by oxygen atoms, three oxygen atoms represents the triangle base lie at nearly the same distance from phosphorous (central metal ion) while the forth one at distance longer than the others three oxygen of triangle base.

The accurate analysis of bond lengths, torsion on angles inside the crystal lattice of cobalt cyclotetraphosphate (Tables 1-3) may enrich us understand that what are the structural factors responsible for lattice stability.

The analysis of data in Tables 1, 2 and 3, one can conclude the following observations; cobalt type one symbolized as (Co1) was linked with all types of oxygen atoms recording the following bond lengths (2.0927, 2.3366, 2.8210, 3.5270, 2.4865 and 3.5756 Å) corresponding to Co1-O1, Co1-O2, Co1-O3, Co1-O4, Co1-O5 and Co1-O6 bond lengths respectively. From these observations one can conclude that O1, O2 and O3 could be located as triangle base of PO<sub>3</sub>- while O4, O5 and O6 can be oriented as axial oxygen to complete the vacant site of tetrahedron forming PO<sub>4</sub><sup>-</sup> anion. The cobalt type one (Co1) is also linked with two different types of phosphorous namely (P1 and P2) with bond

Table 3. (cont.)

Atom1	Atom2	d <sub>1-2</sub> Å	Atom3	d <sub>1-3</sub> Å	Angle 312 <sup>^</sup>	
O3	P2	1.7746	P1	1.8394	148.861	
	P2	1.7746	O4	2.3882	46.911	
	P1	1.8394	O4	3.2099	33.597	
	P1	1.8394	O6	3.3713	92.284	
	P1	1.8394	P1	3.3910	108.337	
	O4	2.3882	P2	3.5777	102.290	
	O4	2.3882	O3	3.7969	57.227	
	O4	2.3882	O1	3.8471	88.198	
	O3	2.5389	O5	2.5520	126.753	
	O3	2.5389	O6	2.5691	82.598	
	O3	2.5389	O2	2.6359	123.991	
	O5	2.5520	Co1	2.8210	54.856	
	O5	2.5520	O1	3.0569	146.390	
	O6	2.5691	O4	3.2099	55.840	
	O2	2.6359	O6	3.3713	98.001	
	O2	2.6359	P1	3.3910	99.094	
	O2	2.6359	P1	3.4278	99.516	
	O2	2.6359	O5	3.4479	108.342	
	Co1	2.8210	O4	3.2099	103.234	
	Co1	2.8210	O6	3.3713	102.506	
	O1	3.0569	P1	3.4278	89.823	
	O4	3.2099	P1	3.3910	112.702	
	O4	3.2099	P1	3.4278	65.342	
	O4	3.2099	O5	3.4479	68.024	
	O4	3.2099	O1	3.5075	83.165	
	O4	3.2099	O1	3.5174	119.071	
	O6	3.3713	O1	3.8471	97.213	
	P1	3.3910	P1	3.4278	131.958	
	P1	3.3910	O5	3.4479	111.574	
	O5	3.4479	O1	3.8471	42.620	
	O5	3.4479	Co2	3.9043	143.431	
	O1	3.5075	O1	3.5174	73.138	
	O1	3.5075	P2	3.5777	142.989	
	O3	3.7969	O1	3.8471	54.622	
	O3	3.7969	Co2	3.9043	123.375	
	O1	3.8471	Co2	3.9043	100.918	
	O4	P2	1.7500	P1	1.9623	145.774
		P2	1.7500	O3	2.3882	47.781
		P1	1.9623	O5	3.7632	92.572
		P1	1.9623	P2	3.8181	82.582
P1		1.9623	O6	3.9110	148.016	
O3		2.3882	O5	2.4663	90.497	
O3		2.3882	O2	2.7355	61.479	
O3		2.3882	O6	3.9110	106.905	
O5		2.4663	O6	2.7645	47.431	
O5		2.4663	O6	3.9110	156.105	
O2		2.7355	O6	2.7645	167.476	
O2		2.7355	O1	2.9451	43.854	
O2		2.7355	O6	3.9110	45.808	
O6		2.7645	O1	2.9451	139.841	
O6		2.7645	O1	2.9609	103.240	
O1		2.9451	O1	2.9609	115.526	
O1		2.9451	O3	3.2099	146.973	
O1		2.9609	O5	3.7294	45.394	
O3		3.2099	O5	3.7632	112.476	
O3		3.2099	P2	3.8181	60.469	

Table 3. (cont.)

Atom1	Atom2	d <sub>1-2</sub> Å	Atom3	d <sub>1-3</sub> Å	Angle 312 <sup>^</sup>
O4	O3	3.2099	O6	3.9110	144.539
	O4	3.3886	Co1	3.5270	99.147
	O4	3.3886	O2	3.5756	72.211
	Co1	3.5270	P2	3.8181	59.587
	Co1	3.5270	O6	3.9110	67.403
	Co2	3.5398	O2	3.5756	42.407
	Co2	3.5398	P1	3.5878	116.699
	Co2	3.5398	O5	3.7294	133.664
	O2	3.5756	P2	3.8181	146.783
	P1	3.5878	O5	3.7294	19.104
	O5	3.7632	P2	3.8181	171.945
	O5	P1	1.2222	O6	2.1215
P1		1.2222	Co2	2.3208	123.015
O6		2.1215	O4	3.7632	163.350
O6		2.1215	P2	3.8101	86.174
O6		2.1215	P2	3.8547	108.843
Co2		2.3208	O4	2.4663	95.320
Co2		2.3208	Co1	2.4865	118.852
O4		2.4663	O4	3.7632	102.737
O4		2.4663	P2	3.8101	95.876
Co1		2.4865	P2	3.8101	49.940
Co1		2.4865	P2	3.8547	49.159
O2		2.5475	O3	2.5520	121.976
O2		2.5475	O1	2.6771	67.870
O3		2.5520	O1	3.7359	64.870
O3		2.5520	O4	3.7632	130.063
O3		2.5520	P2	3.8101	23.154
O1		2.6771	P2	3.8101	61.610
O1		2.6771	P2	3.8547	66.467
O6		3.0309	O3	3.4479	148.096
O6		3.0309	P2	3.4562	127.948
O3		3.4479	O4	3.7632	72.449
O3		3.4479	P2	3.8101	77.786
O3		3.4479	P2	3.8547	138.847
P2		3.4562	O5	3.4814	63.859
P2	3.4562	O4	3.7294	64.063	
O5	3.4814	P2	3.8101	142.125	
O5	3.4814	P2	3.8547	90.676	
P2	3.6692	O4	3.7294	79.797	
P2	3.6692	O1	3.7359	157.355	
P2	3.6692	O4	3.7632	78.546	
P2	3.6692	P2	3.8101	101.543	
O4	3.7294	O1	3.7359	83.831	
O4	3.7294	O4	3.7632	90.906	
O4	3.7294	P2	3.8101	26.815	
O1	3.7359	P2	3.8547	54.240	
O4	3.7632	P2	3.8101	110.453	
O4	3.7632	P2	3.8547	70.438	
P2	3.8101	P2	3.8547	99.099	
O6	P1	1.3354	O5	2.1215	32.284
	P1	1.3354	Co2	2.1694	152.293
	O5	2.1215	O4	3.9110	111.873
	O5	2.1215	O2	3.9416	107.377
	Co2	2.1694	O3	2.5691	110.682
	Co2	2.1694	O4	2.7645	159.226
	O3	2.5691	P1	3.9043	58.958

**Table 3.** (cont.)

Atom 1	Atom2	d <sub>1-2</sub> Å	Atom3	d <sub>1-3</sub> Å	Angle 312
O6	O3	2.5691	O4	3.9110	116.590
	O3	2.5691	O2	3.9416	83.895
	O4	2.7645	O2	2.8042	102.323
	O6	2.7825	P1	3.9043	141.347
	O6	2.7825	O4	3.9110	103.379
	O6	2.7825	O2	3.9416	82.241
	O2	2.8042	O5	3.0309	51.593
	O2	2.8042	O6	3.1627	82.453
	O5	3.0309	O4	3.9110	87.229
	O6	3.1627	Co2	3.3434	158.567
	O6	3.1627	O3	3.3713	46.169
	Co2	3.3434	O4	3.9110	92.220
	Co2	3.3434	O2	3.9416	113.851
	O3	3.3713	P1	3.4154	150.720
	O3	3.3713	P2	3.5725	80.983
	P1	3.4154	O2	3.9416	73.130
	O1	3.7769	O2	3.9416	98.395
	O2	3.8732	P1	3.9043	126.294
	O2	3.8732	O2	3.9416	78.676
	P1	3.9043	O4	3.9110	99.754
	P1	3.9043	O2	3.9416	60.500
	O4	3.9110	O2	3.9416	140.485

distances 3.0353 and 2.9164 Å respectively, which confirms that cobalt has more than one oxidation state over the original common oxidation (CoII and CoIII) inside crystal lattice of cobalt cyclotetraphosphates. This could lead us to informative scientific knowledge that oxidation state of cobalt takes values between  $\text{Co}^{2+}$ ,  $\text{Co}^{m+}$ ,  $\text{Co}^{3+}$  (where m fractions between 2, 3 and  $2 \leq m \leq 3$ ). This result may interpret that why the bond lengths of cobalt with six oxygen atoms are different. Plus effect of coupling of charges due to environmental neighboring groups.

Cobalt type two (Co2) has similar behavior to cobalt type one but the oxygen atoms that represent triangle base are recommended to be O2, O5 and O6 with bond lengths 2.5737, 2.3208 and 2.1694 Å, respectively, while axial oxygen atoms could be occupied by O1, O3 and O4 with bond distances 3.5271, 3.9043 and 3.5398 Å respectively

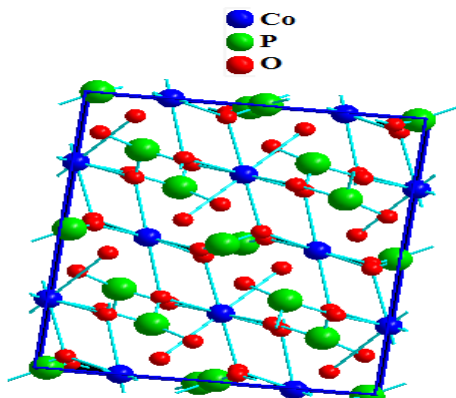
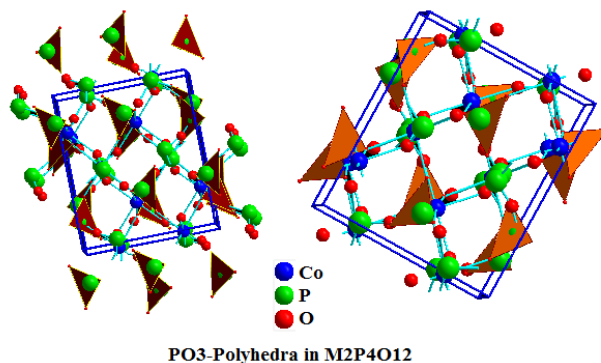


Fig.6 : Unit cell of monoclinic cobalt cyclotetraphosphate .

The cobalt type two (Co2) is also linked with the two different types of phosphorous atoms namely (P1 and P2) with bond distances 3.1577 and 3.7464 Å which confirm that cobalt has more than one oxidation state within the crystal lattice. Similar behavior of existence of multi oxidation states was reported in references [20,21] in which the conditions of synthesis at elevated temperatures in air or oxygen were responsible.

Figure 7 Distribution of PO<sub>3</sub>-polyhedra in the unit cell of cobalt cyclotetraphosphate .

With respect to phosphorous atoms (P1 and P2) it was observed that phosphorous type one (P1) was linked inside crystal lattice with all oxygen atoms recording bond lengths 1.2222, 1.3334 and 1.9623 Å correspond to P1-O5, P1-O6 and P1-O4 respectively. These bond distances are suitable to be the base triangle of PO<sub>3</sub><sup>-</sup> while the rest three oxygen atoms O1, O2 and O3 recorded bond distances 3.4635, 3.5532 and 3.3910 which are suited to be axial atoms.

## Conclusion

The variations of bond distances between Co1, Co2, P1 and P2 and six different oxygen atoms (O1, O2, O3, O4, O5 and O6) inside crystal lattice are responsible for increasing lattice flexibility factor (by controlling in shrinkage and expansion coefficient) and consequently increase its bonds stability to break. These facts can be attributed to three main factors inside lattice.

1.Oxidation state of cobalt takes values between  $\text{Co}^{2+}$ ,  $\text{Co}^{m+}$ ,  $\text{Co}^{3+}$  (where m fractions between 2, 3 and  $2 \leq m \leq 3$ ).

2.Effect of coupling of charges due to environmental neighboring groups effects.

3.The six oxygen atoms are liable to replace each other throughout the lattice to compensate any lattice defects could break bonds (evidence is exchanging positions of triangle base with axial positions).

## References

- Jouini, A., Gacon, J. C., Ferid, M., Trabelsi-Ayadi, M. *Opt. Mater.* **2003**, *24*, 175.
- Kitsugi, T., Yamamuro, T., Nakamura, T., Oka, M., *Biomaterials* **1995**, *16*, 1101.

- <sup>3</sup>Jian-Jiang, B., Dong-Wan, K., Kug Sun, H., *J. Eur. Ceram. Soc.* **2003**, *23*, 2589.
- <sup>4</sup>Martinelli, J. R., Sene, F. F., Gomes, L., *J. Non-Cryst. Solids*, **2000**, *263*, 299.
- <sup>5</sup>Parada, C., Perles, J., Saez-Puche, R., Ruiz-Valero, C., Snejko, N. *Chem. Mater.* **2003**, *15*, 3347.
- <sup>6</sup>Antrapitseva, N. M., Shchegrov, L. N., Ponomareva, I. G., *Russ. J. Inorg. Chem.*, **2006**, *51*, 1493.
- <sup>7</sup>Trojan, M., Brandova, D., *J. Therm. Anal. Calorim.*, **1985**, *30*, 159.
- <sup>8</sup>Trojan, M. *Dyes Pigm.*, **1990**, *12*, 35.
- <sup>9</sup>Trojan, M. *Dyes Pigm.*, **1990**, *13*, 1.
- <sup>10</sup>Trojan, M., Sýulcova, P., Mosner, P., *Dyes Pigm.*, **2000**, *44*, 161.
- <sup>11</sup>Trojan, M. *Thermochim. Acta*, **1990**, *160*, 361.
- <sup>12</sup>Trojan, M., Brandova, D., *Thermochim. Acta*, **1990**, *160*, 349.
- <sup>13</sup>Trojan, M., Sýulcova, P., *Dyes Pigm.*, **2000**, *47*, 291.
- <sup>14</sup>Trojan, M., Brandova, D.; Paulik, F.; Arnold, M., *J. Therm. Anal. Calorim.*, **1990**, *36*, 929.
- <sup>15</sup>Trojan, M., Brandova, D., *Thermochim. Acta*, **1990**, *159*, 1.
- <sup>16</sup>Brandova, D., Trojan, M., Arnold, M., Paulik, F., *J. Therm. Anal. Calorim.*, **1990**, *36*, 677.
- <sup>17</sup>Ramakrishnan, V., Aruldas, G., *Infrared Phys.*, **1985**, *25*, 665.
- <sup>18</sup>Baran, E.J. Mercader, R. C. Massaferrero, A. Kremer, E., *Spectrochim. Acta.*, **2004**, *60*, 1001.
- <sup>19</sup>Soumhi, E. H. Saadoune, I., Driss, A., *J. Solid State Chem.*, **2001**, *156*, 364.
- <sup>20</sup>Averbuch-Pouchot, M. T., Durif, A., *Acta Cryst.*, **1987**, *C43*, 631.
- <sup>21</sup>Chudinova, N. N., Lavrov, A. V., Tananaev, L. V., *Izv. Akad. Nauk SSSR, Neorg. Mater.*, **1972**, *8*, 1971.
- <sup>22</sup>Durif, A., Averbuch-Pouchot, M. T., Guitel, J. C., *Acta Cryst.* **1976**, *B32*, 2957.
- <sup>23</sup>Enraf-Nonius: Structure Determination Package. RSX 11M version. Enraf-Nonius, Delft, **1977**.
- <sup>24</sup>Hilmer, N., Chudinova, N. N., Jost, K. H., *Izv. Akad. Nauk SSSR, Neorg. Mat.* **1978**, *14*, 1507.
- <sup>25</sup>*International Tables for X-ray Crystallography* (Present distributor D. Reidel, Dordrecht), Vol. IV, Birmingham: Kynoch Press, **1974**.
- <sup>26</sup>Palkina, K., Jost, K. H., *Crystallogr.*, **1975**, *831*, 2285.
- <sup>27</sup>Schulz, L., *Z. Anorg. Allg. Chem.* 1956, *287*, 106.
- <sup>28</sup>Tezikova, L. A., Chudinova, N. N., Fedorov, P. M., Lavrov, A. V., *Izv. Akad. Nauk SSSR, Neorg. Mat.* **1974**, *10*, 2057.
- <sup>29</sup>Elsabawy, K. M., Elbagoury, N. H., *Adv. Appl. Science. Res.*, **2011**, *2(2)*, 38.
- <sup>30</sup>Elsabawy, K. M., *Cryogenics*, **2011**, *51*, 452.

Received: 30.09.2012.

Accepted: 03.10.2012.